Doctoral Programme in Industrial Engineering
Dottorato di Ricerca in Ingegneria Industriale

XXXIV

Design automation of lattice-based customized orthopedic for load-bearing implants

ING/IND-15

Doctoral Candidate
Lorenzo Guariento

Supervisors
Prof. Monica Carfagni

Prof. Yary Volpe

External Referees
Prof. Francesca De Crescenzio
Prof. Gianpaolo Savio

Dean of the Doctoral Programme
Prof. Giampaolo Manfrida

UNIVERSITÀ DEGLI STUDI FIRENZE

DOTTORATO DI RICERCA IN
INGEGNERIA INDUSTRIALE

CICLO XXXIV

COORDINATORE Prof. Giampaolo Manfrida

Design automation of lattice-based customized orthopedic for load-bearing implants

Settore Scientifico Disciplinare ING/IND-15

Dottorando
Dott. Lorenzo Guariento

_____
(firma)

Tutore
Prof. Monica Carfagni
Prof. Yary Volpe

_____
(firma)

Coordinatore
Prof. Giampaolo Manfrida

_____
(firma)

Anni 2018/2021

Years 2018/2021

Dedicated to…

Summary

Recent developments in Additive Manufacturing technology are transforming the medical industry, switching from the mass production of devices to the production of customized components. Orthopedics, in particular, has greatly benefited from the advent of Additive Manufacturing and its potential to produce complex parts, as it has allowed the manufacturing of customized orthopedic implants to treat complex cases that would not be treatable otherwise. Additive manufacturing is contributing to improve the quality of cares because allows for the reconstruction of severely damaged bones and the restoration of joint kinematics.

The greatest obstacle to the diffusion of custom orthopedic prostheses, to date, has been the effort required to design such specific devices, whose geometry and characteristics differ each time depending on the patient's anatomy and clinical conditions. The design process requires a combination of clinical and engineering knowledge, as well as multiple software systems to analyze medical images and model the device. This ultimately leads to a time-consuming process that implies significant costs.

The goal of this Ph.D. is to optimize and automate the design phase and 3D modeling of custom orthopedic implants, with the aim of making such devices more and more accessible, safer and with better performances compared to the state of the art. In order to reach such goal, this work has addressed the following aspects:

- Overcome the current limitations for load-bearing orthopedic implants by improving the design
- Identify the most time-consuming operations and develop an automatic workflow

This work focuses on the pelvis because is technically very challenging due to its complex geometry and the presence of several vital structures, as organs and large blood vessels.

By analyzing the state of the art regarding metal pelvic prostheses, the main cause of implant failure was found to be Stress-Shielding: it occurs due to the higher stiffness of the metal compared to the bony tissue which causes bone resorption, resulting in implant failure. According to the most recent studies, the most effective strategy to mitigate this effect is to decrease the elastic modulus of the metal components by creating an internal lattice structure. Among all the possible geometries for lattice structures, the most promising one for orthopedic applications was identified in the Gyroid. The surface of the Gyroid is defined by a simple trigonometric equation and can be easily manipulated to alter its geometric properties to meet the biomechanical requirements for orthopedic implants. The gyroid has a complex

architecture which is able to promote osseointegration, which creates a strong and long-lasting bond between implant and bone. One of the most important features of the Gyroid is that its elastic modulus is a function of lattice density, which allows to correlate geometric features with mechanical properties by simple mathematical equations.

For this work, the Gyroid was modeled with the CAD software nTopology, which provides useful programming capabilities for automating repetitive CAD operations. The mechanical properties of the gyroid were assessed by FE simulations, which allowed to define the ideal geometric properties for load bearing applications and a design space for the geometric features of the Gyroid structure, able to simultaneously fulfill biological, mechanical and manufacturing constraints.

With an eye toward automating the design of orthopedic prostheses, this work addressed the most time-consuming manual operations. With regard to the pelvis, the design often does not exactly reproduce the original anatomy with the goal to reduce weight and cost, instead the primary concern is the restoration of the acetabular joint kinematics. The calculation of the acetabulum parameters is typically performed by hand by experienced operators, however in case of highly defective anatomies this process can be time consuming with suboptimal results. In this regard, an automatic method has been developed, called eSSM, based on Statistical Shape Analysis, for the reconstruction of anatomical models that includes the coordinates of the joint center and the orientation of the acetabulum, fundamental parameters for the restoration of joint kinematics.

Regarding the automation of orthopedic implant design, an algorithm has been developed within nTopology that is able to generate the 3D model of pelvic prosthesis in 2 ± 0.15 minutes starting from simple CAD inputs. The goal is to develop a simple and effective tool within the reach of non-expert CAD users, reduce design time and the related costs. The developed algorithm was tested on 20 case studies provided by the Careggi Hospital in Florence and proved to be extremely robust, providing the expected results in all cases tested. It is important to note that the implemented method can be adapted to model implants in other body districts with minimal effort.

The last activity has been the assessment of the hypotheses made and the design strategy through FE analysis of the pelvis with acetabular implant; the simulations confirmed that the introduction of the Gyroid lattice structure is effective in reducing the damaging effects of Stress-Shielding.

Table of contents

List of Figures

List of tables

Acronyms List

AM Additive Manufacturing
PSI Patient Specific Instrument
FE Finite Element
THA Total Hip Arthroplasty
CAx Computer Aided technologies
TPMS Triply Periodic Minimal Surface
SA/V Surface Area to Volume ratio
COR Center Of Rotation
SSA Statistical Shape Analysis
ROI Region Of Interest
PDM Point Distribution Model
SSM Statistical Shape Model
eSSM enhanced SSM
PCA Principal Component Analysis
TS Training Set
MoVs Modes of Variations
SDF Signed Distance Fields
PAC Pelvis with Acetabular Cup
IBS Implant Base Shape
SED Strain Energy Density

Introduction

In recent years, Additive Manufacturing (AM) has deeply transformed healthcare industry, enabling healthcare providers with an increasing number of innovative technologies to improve patient care with less invasive surgeries and better outcomes.

One of the fields that have been influenced the most by the spread of AM is orthopedic surgery, where such technologies are currently employed for a wide variety of applications, as:

- Anatomic models for surgical planning: support surgeons to define the most appropriate surgical approach with a visual and haptic understanding of the patient-specific pathology and anatomy [1], [2]. Such models, and especially physical ones, can also be exploited to help the patient to better understand their medical conditions.
- Patient-specific instruments: allow to perform complex surgeries with high accuracy; Patient Specific Instruments (PSI) are custom devices designed from diagnostic image segmentation of the very patient. In orthopedics PSIs, allow to perform difficult osteotomies, which is a game-changing technology in oncological orthopedics because allows to easily obtain clear resection margins [3].
- Custom implants: whenever standard implants are not applicable, e.g. in complex revision surgeries or oncological cases, AM allows to manufacture custom metal implant for bone replacement that perfectly fit the patient's anatomy. Custom implants have proved to improve the surgical outcome and restore limb functionality [4], [5]. The extreme design flexibility ensured by AM also allows to create lattice structures to reduce implant's weight and thus increase the patient's comfort, besides improving osseointegration [1], [6].

AM is improving healthcare quality by providing customized solutions; in orthopedics, surgeons can now perform less invasive surgeries, lowering the overall operation time and improving the surgical outcome [6], thus improving the patients' safety and satisfaction [7].

The introduction of AM and related technologies in medicine is a breakthrough in treatment modalities for very complex cases that have been untreatable before, shifting from the paradigm "one size fits all" to customized treatments. AM, though, still has some drawbacks. Regarding custom orthopedic implants, the main limitation to their spread lies mainly within the design phase, because is cumbersome and time-consuming. The design process of custom implants can be resumed by the following Figure 1, where the operations carried out by clinicians are represented in red, while those demanded to engineers and technicians are highlighted in blue.
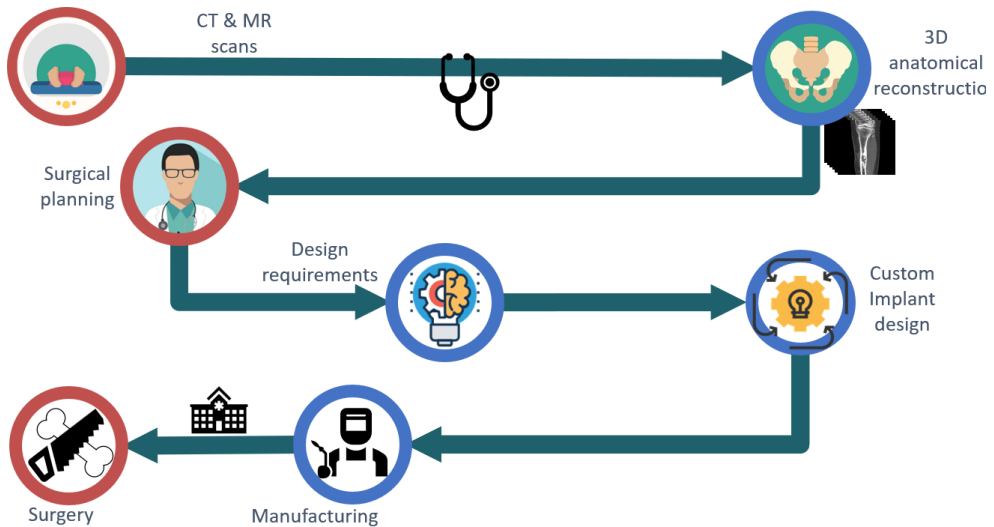
Figure 1 Design workflow of custom devices. The operations carried out by clinicians are represented in red, while those demanded to engineers and technicians are highlighted in blue.

The process starts with the diagnostic image segmentation to produce 3D patient-specific anatomical models; such operation is typically carried out by expert users with dedicated software. The next phase consists in the surgical planning along the definition of the design constraints. This is by far the most time-consuming operation because several strict biomechanical and technological issues must be taken into account, thus several iterations are typically necessary before the ultimate design is achieved. The definition of the design constraints involves a close cooperation of surgeons and engineers to produce a design with is both effective from the clinical and mechanical point of view. Finite Element (FE) Analysis of the custom implant can deliver significant information about the interaction with the surrounding tissues and the compliance with the strict biomechanical requirements, though the implementation of a patient-specific FE model is highly time-consuming, which conflicts with the need to deliver the devices as rapidly as possible, in particular for oncological cases where the time factor is crucial.

Once the design phase is complete, the device is eventually manufactured and implanted.

The goal of the present Ph.D. is to analyze, optimize and eventually automate the design process of custom orthopedic pelvic implants for load bearing applications, in order to speed-up the process and deliver high-performance customized devices in a short time, as well as cut the related cost by reducing the time-to-implant. The design automation also delivers significant advantages in terms of product safety and reliability; in addition, by reducing the time associated with implant's modeling, more resources can be spent on FE analysis for a deeper biomechanical evaluation of the system and further optimize the design. Ultimately, the objective is to make custom orthopedic implants more and more accessible for patients with severe conditions that would benefit of personalized solutions. This Ph.D. thesis focuses on pelvic implants to tackle the challenges introduced by the complex anatomical structure as well as the presence of numerous vital structures [8]. Nevertheless, the principles exposed in this work can be easily transferred to other anatomical districts.

First, the main biomechanical requirements for orthopedic implants will be analyzed along with the main causes of failure in order to provide an outlook over the most critical aspects to take account of during the design of custom orthopedic devices. The following session addresses the introduction of a promising lattice structure for load bearing applications, namely the Gyroid: its formulation and a method for its implementation within the workflow of the design of a custom prosthesis will be presented. Follows the discussion of the developed method for design of custom orthopedic pelvic devices. Finally, a FE model of the pelvis will be presented to validate the concepts exposed in this work. In the final chapter the results will be discussed along with the possible future developments.

1. Pelvic orthopedic implants

Primary bone tumors are rare conditions; they account for 3% to 5% of childhood cancers and for less than 1% of all cancers in adults [9]. Despite the low incidence, bone tumors are the third cause of tumor-related deaths in developed countries [10]. In particular, pelvis osteosarcomas represent 7% to 9% of all osteosarcomas and the related survival rate ranges between 20% and 47% [10], mainly due to late diagnose in advanced stage with large tumor size. Pelvic surgery is particularly challenging and technically demanding because of its complex anatomical structure, surrounded by several vital structures as large blood vessels and organs. In case of large bone deficiencies due to bone tumors, traumas, or other pathologies, a bone substitute becomes necessary to restore pelvic bone continuity and limb functionality. The surgical treatment consists of removing the affected area and replace it with a metal implant; such procedure, when involves the acetabular region, is named Total Hip Arthroplasty (THA).

THA is an established procedure extensively performed worldwide with high success rate [11], though complex cases as oncological or revision surgeries require custom solutions. Standard off the shelf devices are effectively employed to treat the most common conditions, though they can't cover the extreme variability in terms of shape, geometry and mechanical requirements encountered in oncological patients, as each case has different requirements.

Both oncological and revision surgery consist in the removal of the damaged bone stock and the implantation of a metal prosthesis. The goal is to restore limb functionality with a stable and long-lasting implant. To date, custom metal pelvic implants are widely employed to deal with large bone defects because they can be tailored to the very patient's anatomy and can be adapted to fill the missing bone and provide a stable fixation whenever standard implants are not suitable [12]. The design process requires an accurate pre-operative planning to assess the bone deficiency and define the main constraints which will drive the whole process. An accurate virtual reconstruction of the defected anatomy is crucial to determine the best surgical approach and to design an implant which perfectly fits the patient's anatomy with good biological and mechanical performances.

In the next section the main causes of implant failure will be analyzed in order to identify the most effective design approach.

1.1. Main causes of implant failure

Several studies investigated the main causes of pelvic implant failure [11], [13], [14], which can be classified as:

- Aseptic loosening: the relative motion between parts generates debris which cause inflammatory reaction which are one of the major causes of bone resorption [14], [15]
- Stress-shielding: the introduction of a metal implant alters magnitude and direction of load transmission through the bone leading to bone resorption according to Wolff's law [13], [16]
- Periprosthetic fracture: fractures that occur in association with an orthopedic implant and are associated with significant morbidity and, in some cases, mortality [17]

According to literature studies, stress shielding has been identified as the main cause of implant's failure hence the next section will focus on this phenomenon, its causes and how to design a prosthesis in order to mitigate its effects.

1.2. Stress shielding

Stress shielding is one of the main problems that lead to implants' failure because it reduces the support of the implant increasing the risk of implant loosening and peri-prosthetic fracture [14], [18], [19]. It occurs when a metal component is implanted; since it is much stiffer than the host bone, the implant bears most of the physiological load.

Stress shielding causes a mass and density reduction of the bone surrounding the implant due to bone remodeling mechanism, as stated by the "Wolf's law" [20]. As the bone is a living tissue, constantly evolving, it must be mechanically stimulated in a fashion as close as possible to its natural condition to maintain the tissue healthy. What occurs is summarized in Figure 2: whenever the mechanical stimuluses decrease or increase, the bone density decreases or increases accordingly [21], [22], [23].
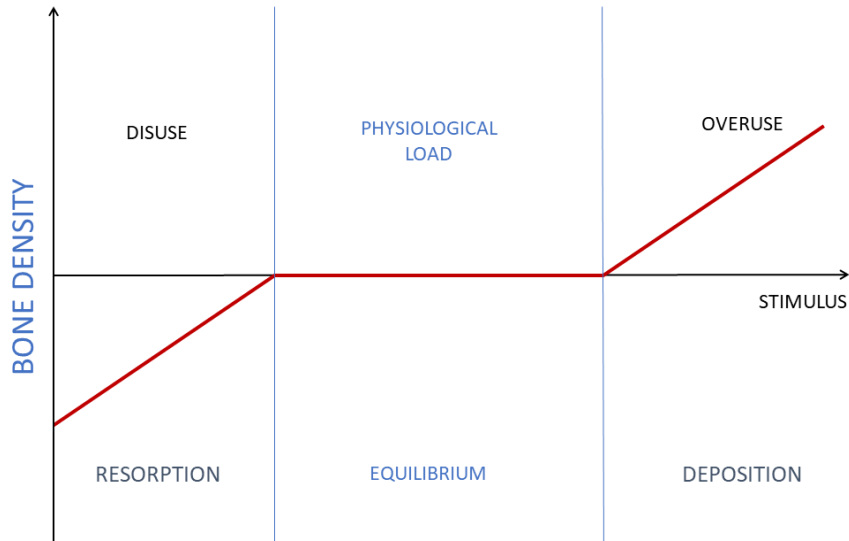
Figure 2 bone remodeling mechanism

Stress shielding effects can be quantified as the variation of strain energy in the host bone after surgery, with respect to a reference value of strain energy in the intact bone, as resumed by Equation 1 [13], [19]:

$$Stress - shielding\ Signal\ = \frac{strain\ energy\ (treated) - strain\ energy\ (reference)}{strain\ energy\ (reference)} \quad (1)$$

Stress shielding also reduces the quality of the remaining bone stock, increasing the risk of fracture and aseptic loosening after revision surgery, whenever necessary. This is particularly concerning for the future for young patients now undergoing THA, as the number of revision THAs is projected to rise as well as life expectancy [13].

1.2.1. Lattice structures to face stress shielding effects

An efficient method to decrease the elastic modulus of a metal body, and thus the mechanical mismatch between implant and bone, is to create a lattice infill [24]–[29]. Recent developments in Computer Aided Technologies (CAx) and Additive Manufacturing (AM) allow to model and manufacture porous lightweight cellular metallic structures [15], [30]–[34] which exhibit a lower elastic modulus compared to the bulk material. A lattice structure leads to several advantages:

- Mass reduction, and thus weight and cost
- Possibility to tune the geometric, and consequently mechanical, properties
- Promote bone ingrowth, providing a stable biological fixation

It is fundamental that the designed lattice provides a biomimetic mechanical environment that promotes cell migration and seeding [35]. Cell viability, seeding and

proliferation are sensitive to the 3D structure of the scaffold, thus it is crucial to mimic the natural architecture of the tissues, the bone in this case, to promote the integration of the host tissue within the implant [36]. Besides the geometry, a mechanical stimulation of the cells as close as the natural condition as possible is beneficial [37]–[40].

Besides stress-shielding mitigation, osseointegration is a key factor for a long-lasting orthopedic implant. Osseointegration is defined as a direct structural and functional connection between ordered, living bone and the surface of a load-carrying implant [41]; thus, bone grows into the porous structure creating a very strong bond between bone and implant.

Bone ingrowth into an implanted structure is affected by a multitude of factors, including material microarchitecture, e.g. cell topology, porosity, pore shape and size, and properties of the constituent material [42].

The scaffolds suitable for tissue engineering should satisfy the following structural requirements for an optimal integration with the host bone:

- the scaffold architecture should structurally and functionally mimic the structural hierarchy of the host tissue [43]
- the scaffold must be porous with interconnected pores to provide a viable space for cells, facilitate the diffusion of nutrients and waste products from the implant, and enhance vascularization [44]–[46]
- the pores should be interconnected to allow Material transport and cell migration [47]
- the pores should have curved cross-sections and avoid straight edges To mimic the curved partitions that separate cells aggregates [48]
- the scaffold should retain its structure after implantation without undesired deformations [49], [50]
- the permeability of the scaffold must facilitate the inflow of nutrients and the disposal of metabolic waste [51] through the scaffold's pores

An orthopedic implant should be designed to guarantee a stable fixation with the host bone and limit stress shielding effects, while ensuring its structural integrity for its life-cycle.

Biocompatible metal materials as stainless steel, Co-Cr alloys and titanium alloys are widely employed for orthopedic applications [52], though the mismatch between Young's modulus e.g. of titanium (E = 100 – 110 GPa) and host bone (E = 5 – 30 GPa) has a negative effect over stress shielding. The most promising approach to tackle this issue is to match the elastic modulus of the implant with that of the bone by implementing a lattice infill, while maintaining an adequate mechanical resistance to static and repetitive loads.

A variety of methods have been developed to produce porous metallic scaffolds with a homogeneous pore size distribution that provides a high degree of interconnected porosity for bone ingrowth [53].

The most popular lattices for bone replacement are:

• Strut-based cellular solids (ordered or stochastic, mimicking trabecular bone, Figure 3)

• Triply Periodic Minimal Surface (TPMS) based cellular solids (Figure 4)
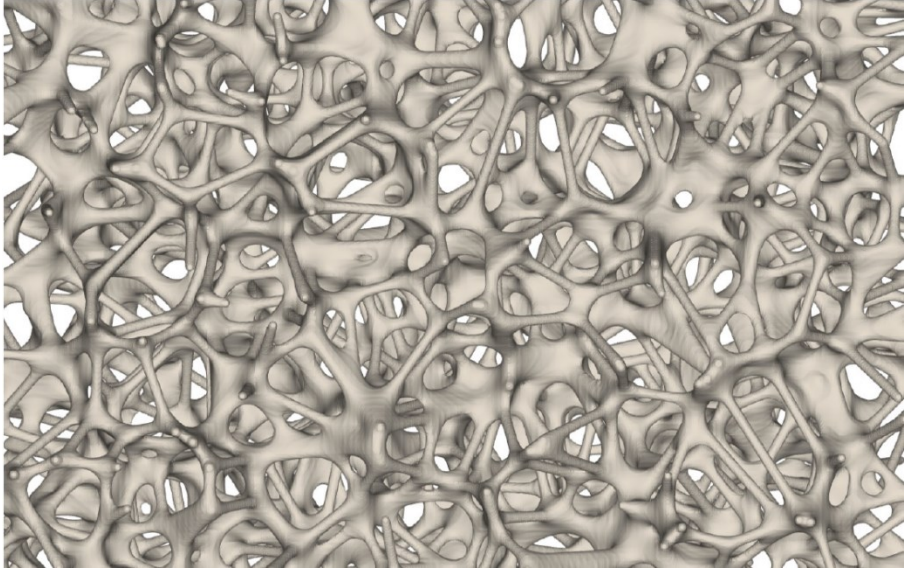
Figure 3 Stochastic strut-based lattice, mimicking the trabecular bone
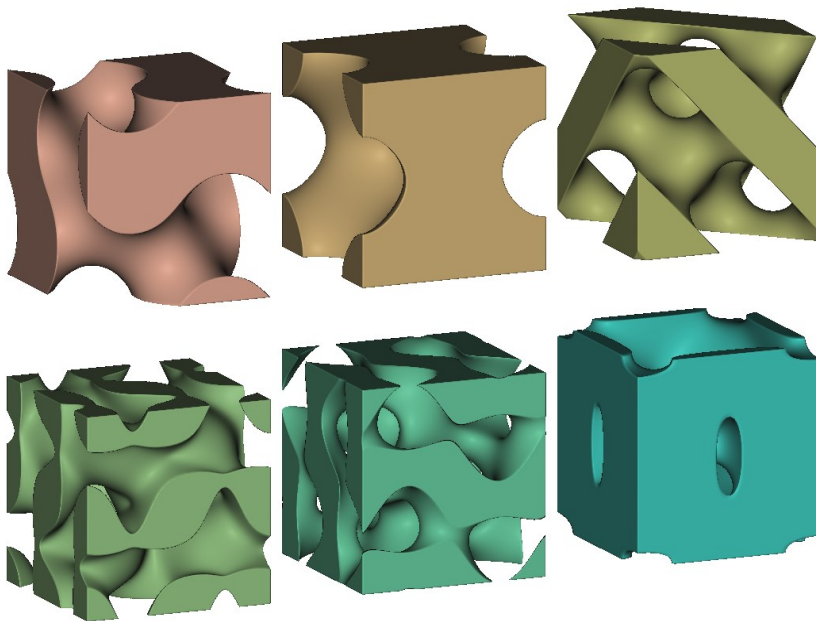
Figure 4 Six TPMS samples. In the first row, from left to right: Gyroid, Swarz, Diamond. In the second row, from left to right: Lidinoid, SplitP, Neovius.

In the past decades, a broad variety of lattice structures for orthopedic applications have been tested, such as diamond, truncated cube, truncated cuboctahedron and tetrahedron [54]. Among them, recently the TPMSs have proven to be the most suitable for the discussed

application [31], [55], [56]. TPMSs are a class of implicit surfaces which have often been observed in nature, as in biological membranes [57], [58]. Minimal surfaces have a constant mean curvature of zero (the sum of the principal curvatures at each point is zero) and interconnected pores. TPMSs are complex 3D topologies that locally minimize surface area for a given boundary and can be repeated periodically in three perpendicular directions [59]. TPMSs structures have smooth boundless surfaces that divide the space into two labyrinths in the absence of self-intersections [60]. Compared to strut-based lattices like cubic, octahedral, kelvin etc., these surfaces can guarantee a better biological fixation because they promote a stronger cell adhesion and vascularization [61], [62]. TPMS-based cellular structures are characterized by a smoother transition at the connection point of the structure's components compared to strut-based cellular structures [58], which also reduces stress concentrations. The materials' surface characteristics affect the osteoblast adhesion on biomaterials, a fundamental premise for bone integration; therefore, the porosity, pore shape and pore size of the biomaterial play a critical role in the bone ingrowth in vivo [24]. Several studies have proved that porous scaffolds with mathematically designed TPMSs provide a suitable environment for cell adhesion and proliferation [35], [61]. Osseointegration, and thus a stable fixation between bone and implant, is the result of a combination of physiological processes which are highly dependent to some characteristics of the lattice structure: (i) pore size, (ii) pore architecture, and (iii) surface area to volume ratio (SA/V ratio). The main advantage of minimal surface biomimetic scaffolds is the open cell structure, deemed to facilitate cell migration and vitalization, while retaining a high structural stiffness.

Among the TPMSs surfaces, the Gyroid (Figure 5) provides a higher SA/V ratio compared to strut-based lattices [35], which have been proved to promote cell adhesion and proliferation. Gyroid surface has neither planes of symmetry nor straight lines, with a similar topology to the trabecular bone, and allows to create high-performance lattice structures [63], [64]. TPMSs can be mathematically modelled with simple implicit functions, and their geometry can be altered in R^3 space with no discontinuities or sharp edges [56], [35], [59], which has a positive effect in reducing stress concentrations. Moreover, thanks to this property, the design process of implants is simplified and easy to control; specifically, the designer benefits from a higher freedom that can be exploited to improve the performances of the prosthesis. Furthermore, TPMS structures have features that maximize their manufacturability via powder-based AM processes [56], [57]. Struct-based geometries typically show an excess of sintered material in the nodes of the structure and higher deviation from the desired geometry, with respect to TPMS surfaces [62]. Gyroid proved to be one of the most promising lattice structures for orthopedic applications thanks to its geometric and mechanical properties, as well as its manufacturability via AM.

1.3. Gyroid lattice

The mathematical formulation of the Gyroid surface (Equation 2), depicted in Figure 5, was first defined by Alan Shoen in 1970 [65]:

$$\sin\left(\frac{2\pi}{a}x\right)\cos\left(\frac{2\pi}{a}y\right) + \sin\left(\frac{2\pi}{a}y\right)\cos\left(\frac{2\pi}{a}z\right) + \sin\left(\frac{2\pi}{a}z\right)\cos\left(\frac{2\pi}{a}x\right) = t \ (2)$$

where:

- *a* = cell size [mm]
- *t* = offset from the gyroid mean surface [mm]
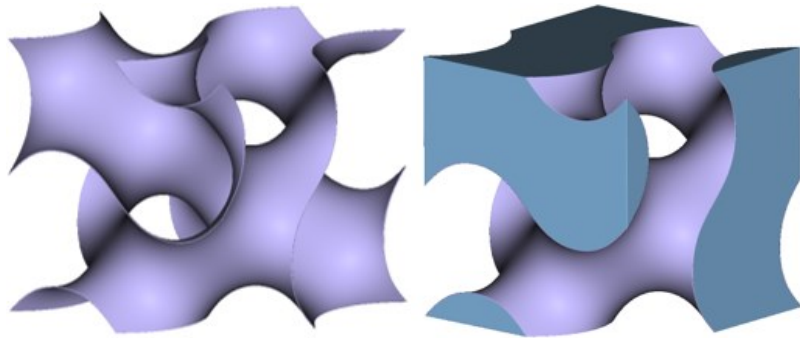
Figure 5 Gyroid surface. On the left the Gyroid surface with t=0; on the right, a solid Gyroid.

The parameters *a* and *t* in Equation 2 control the geometric features of the Gyroid: it is possible to independently control pore size [66], defined as the diameter of the inscribed circle between the struts of unit cell in planer view, and relative density, as described by Equation 3 and Equation 4.

$$p_s = 0.12a + 1.5t \qquad (3)$$

$$\rho_{rel} = \frac{V_c}{V_s} = \frac{2t}{a} + 0.5 \qquad (4)$$

where:
Vc= volume of cellular solid
Vs = volume of solid part

The Gyroid geometric and mechanical properties can be tailored to meet the specific constraints of an orthopedic implant by modifying the parameters that control pore size and relative density, as highlighted in Figure 6, where t increases from left to right and p_s grows accordingly. The following paragraphs will show how the Gyroid surface can be optimized to meet, at the same time, biological, mechanical, and technological requirements.
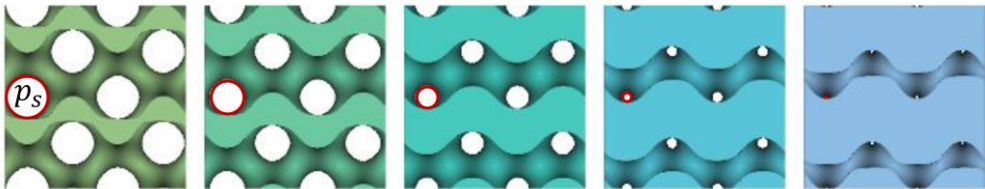
Figure 6 Gyroid lattice with increasing relative density from left to right. Pore size, highlighted in red, decreases as the relative density grows.

1.3.1. Gyroid for osseointegration

The ideal pore size range depends to the pore geometry and interconnectivity. Multiple studies have investigated the performances in terms of bone integration for several cell structures, and the ideal pore size range for osseointegration has been found to be, for the specific Gyroid structure, between $0.1 < p_s < 0.6$ mm [61], [62], [67], [68]. The relationship between pore size and porosity is depicted in Figure 8. The ideal relative density values lay between 20 and 50% [69].

1.3.2. Mechanical properties

Cellular solids are of great interest for load bearing and lightweight applications. The mechanical properties of cellular solids are related to the properties of the cell wall material and to the cell geometry and can be described by simple formulae. The Gibson-Ashby model [70] provides a simple and useful relationship between cell density and elastic modulus. Equations (5) and (6) show respectively the relationship between the relative density of the cellular material and its elastic modulus and compressive strength (constants with subscript s refer to the solid material):

$$\frac{E}{E_s} = C_1 (\rho_{rel})^n \quad (5)$$

$$\frac{\sigma_{pl\_latt}}{\sigma_{y\_s}} = C_2 (\rho_{rel})^m \quad (6)$$

where:

- E = Young modulus of cellular solid
- E_s = Young modulus of solid material
- ρ_{rel} = relative density of cellular solid
- C_1 = constant
- σ_{pl_latt} = Compressive strength of cellular material
- σ_{y_s} = Yield stress of the solid material
- C_2 = constant

Dense Titanium and some of its alloys are the most employed materials for load-bearing bone implants, as they have a good biocompatibility, as well as a higher corrosion resistance and lower elastic modulus compared to other metal biomaterials as stainless steel and cobalt alloy [63]. It is worth to note that there is a huge mismatch between the mechanical properties of metal and bone, in fact dense Ti-6Al-4V has a Young's modulus of 110 GPa, while the bone exhibits a Young's modulus of 0.5-30 GPa [63], [71], depending on anatomical region, age and sex. The elastic modulus of the metal implant can be tuned to that of the bone through the creation of lattice structures thanks to advanced manufacturing capabilities of AM. Gyroid shows higher SA/V ratio and highly efficient mechanical properties compared to traditional lattices, as cubic lattice, diamond, dodecahedron, honeycomb [59], [64], [72].

The Gibson-Ashby model (see (5) and (6)), provides a useful and straightforward tool to predict the Young's modulus of a cellular metal structure, as a function of its relative density [70]. Powder-bed fusion has been successfully employed to manufacture gyroid lattice structures with the elastic modulus within the range of the healthy bone [31], [55], [56], [73], [74]. Figure 7 shows the design space that produces a valid elastic modulus, comparable with the bone: a corresponding solid fraction value can be identified and considered as desirable target for the design of the lattice.

1.3.3. **Manufacturability**

Several literature studies have covered the analysis of the factors that could affect the manufacturability for lattice structures [75]: process parameters obviously play a major role on the achieved result and the allowed minimum feature size of the structure, though the Gyroid lattice exhibits a good manufacturability via powder-bed AM technologies, confirmed by a comparison of digital data with 3D CT scans of structures actually produced [63], [76], [77]. One of the main advantages of the Gyroid is that it is a self-supporting structure [78], [79]; the absence of straight lines and the zero mean curvature allows to manufacture via AM a gyroid lattice structure with high accuracy [63], [78]. Furthermore, such geometric characteristics also provide a smooth path from internal regions to the external surface and allow to easily remove the remaining powder. The gyroid parameters must be chosen in order to not exceed the maximum resolution of the AM process. The Gyroid strut size, represented in Figure 7 as the diameter of the minimum cross section of the Gyroid's struts, can be calculated with Equation 7:

$$Strut_{size} = \frac{a}{\sqrt{2}} - 2(0.12a + 1.5t) \tag{7}$$
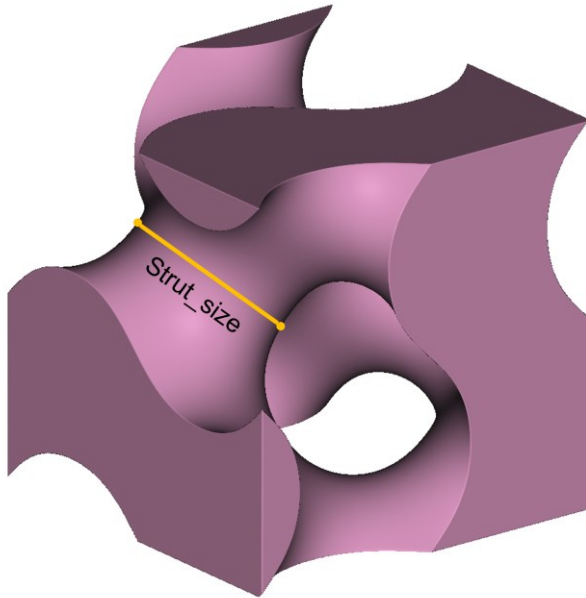
Figure 7 Gyroid Strut size, defined as the diameter of the minimum cross-section of the strut.

1.3.4. Design space for orthopedic applications

Summing up all the previously discussed aspects, it is possible to devise a design space for a Gyroid-based structure. Considering the intersection between the constraints imposed on the gyroid cell parameters (essentially *a* and *t* in Equation 2), by technological, biological, and mechanical constraints, it's possible to determine an optimal region of fabrication for lattice structure for orthopedic application.

With this respect, Figure 7 shows the design space evaluated for a Gyroid cellular material. The curves presented in Figure 8 are qualitative, since manufacturability and mechanical properties depend on the specific AM technology, material and post-processing operations [62], [75]. To be noted that in Figure 7 [62], the Manufacturability curve doesn't take into account the removal of the non-sintered powder and only provides information regarding the minimum feature size of the gyroid lattice that can be manufactured.
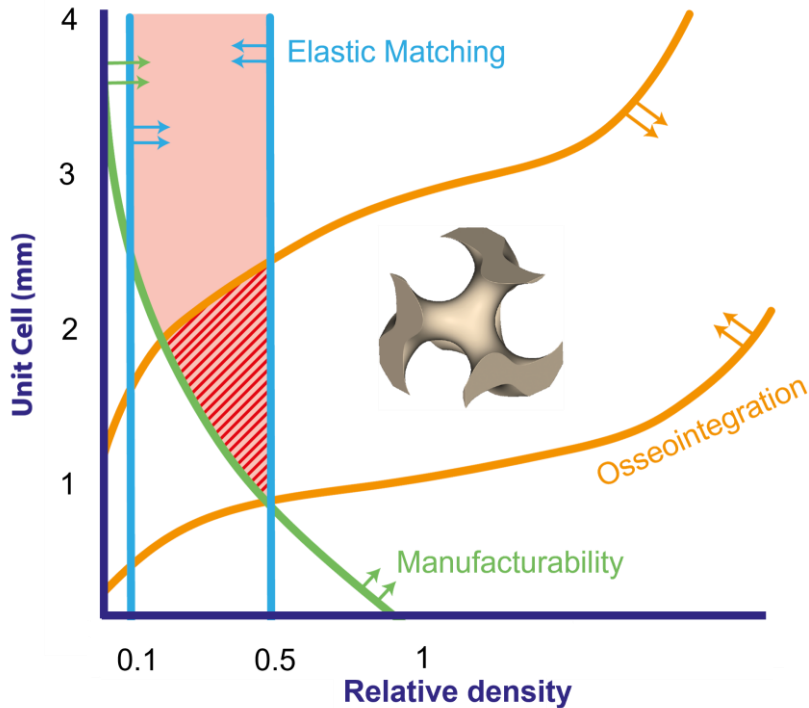
Figure 8 Gyroid design space. The red dashed line represents the design space which respects jointly the three constraints. Whenever the osseointegration constraint is removed, the design space gets wider with a higher design freedom.

This concept can be expanded considering that the constraints defining the shape of the design space refer to a single cellular structure characterized by continuous geometric properties. However, thanks to its mathematical formulation (2) it is possible to imagine a gyroid-based lattice structure characterized by locally defined geometric properties, which

vary continuously across the volume (Graded Gyroid). By implementing this type of structure, the design constraints defined in Figure 8 are subsequently relaxed from a global definition to a local one, allowing the designer a higher freedom in the definition of a specific structure. The osseointegration constraint implies a small cell size, thus the possibility to increase the cell size far from the bone-implant interface delivers great advantages in terms of manufacturability, especially for the removal of the non-sintered metal powder. Such aspects will be discussed in depth in the following sections.

1.4. Graded Gyroid design

The mathematical formulation of the gyroid surface allows to locally control the geometry and alter its geometric characteristics within a volume of the desired shape with continuity, thus generating a body with different mechanical properties with a gradual variation in composition, which reduces stress concentration effects near the interface between different phases.

Lattice hybridization [80] allows to combine two or more implicit surfaces with a controlled smooth transition; such approach allows to locally tune the geometric, and thus mechanical, properties according to specific needs. The general hybrid surface Equation is:

$$\varphi_{hyb}(x, y, z) = \alpha(x, y, z)\varphi_1(x, y, z) + \big(1 - \alpha(x, y, z)\big)\varphi_2(x, y, z) \quad (7)$$

where:

- $\varphi_{hyb}(x,y,z)$ is the resulting hybrid surface
- $\varphi_1(x,y,z)$ and $\varphi_2(x,y,z)$ are the implicit surfaces to be combined
- $\alpha(x,y,z) = 1/(1 + \exp(-kG(x,y,z)))$

α is a weighting factor that satisfies $\alpha(x,y,z) \in [0,1]$ and describes a monotonic change from 0 to 1. $G(x,y,z)$ is the transition boundary, and the constant k affects the width of the transition band. Figure 9 shows an example of transition where $G(x,y,z)$ is defined as a planar surface. Two regions, defined with the same cell size but different relative densities are separated by $G(x,y,z)$. The image shows the effects induced by different transition rates k in the formula.
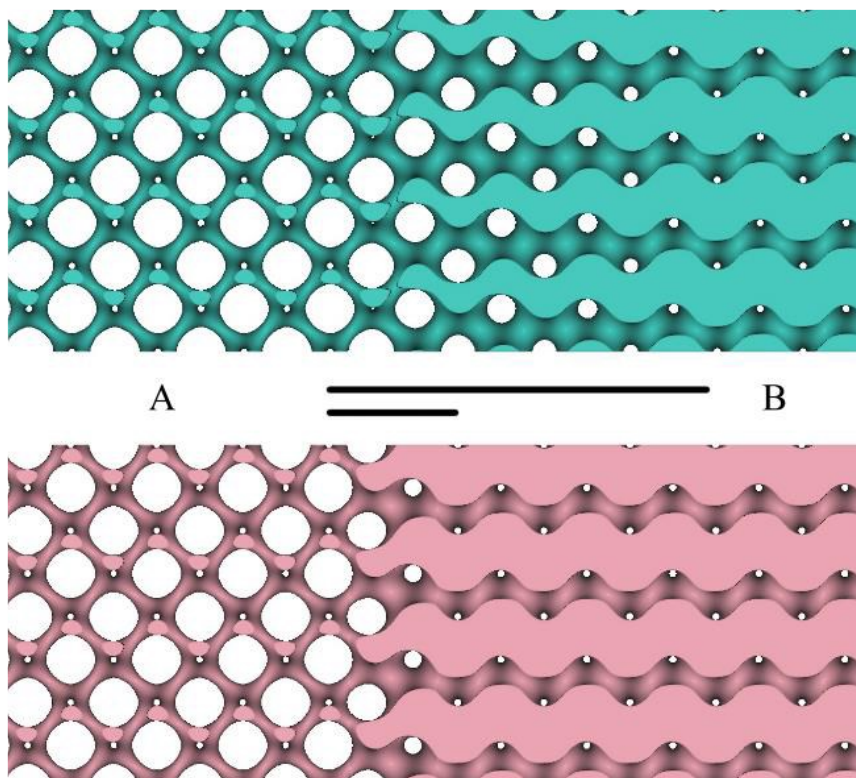
**Figure 9 Monotonic transition from region A to region B in ρrel across a Gyroid hybrid
structure. The black lines indicate the transition region, whose extension is affected by k.**

This method only requires the knowledge of the G(x,y,z) Equation, and allows to create a continuously graded lattice infill of any arbitrary geometry; such result is particularly interesting in the orthopedic field because allows to design, within a single body, regions with different geometric and/or mechanical properties with a smooth and controlled transition.

Taking into consideration the design space defined in Figure 8, the discussed constraints should be assured simultaneously only for the sub-volume in the close proximity of the healthy bone. Far from the bone-implant interfaces, the osseointegration constraint loses its significance. Consequently, in this area the design space is wider thanks to the relaxation of constraints.

A significant example is showed in Figure 10, where a simplified global geometry (i.e., a rectangular prism) that could represent a prosthetic implant is composed of three main regions. Region A is a lightweight optimized support structure, designed following an elastic matching approach to mimic the mechanical properties of healthy bone, hence reducing stress shielding occurrences. Region B is a solid superficial layer that can be introduced on all the external surfaces which are not in direct contact with spared bone. This type of surface is required to reduce the risk of damages to the surrounding tissues. Finally, Region C is a thin superficial layer designed to maximize bone integration and could be applied on each bone-implant interface. Furthermore, as discussed in the previous section, the user can control the global shape of each region as well as the transition rates between the zones.
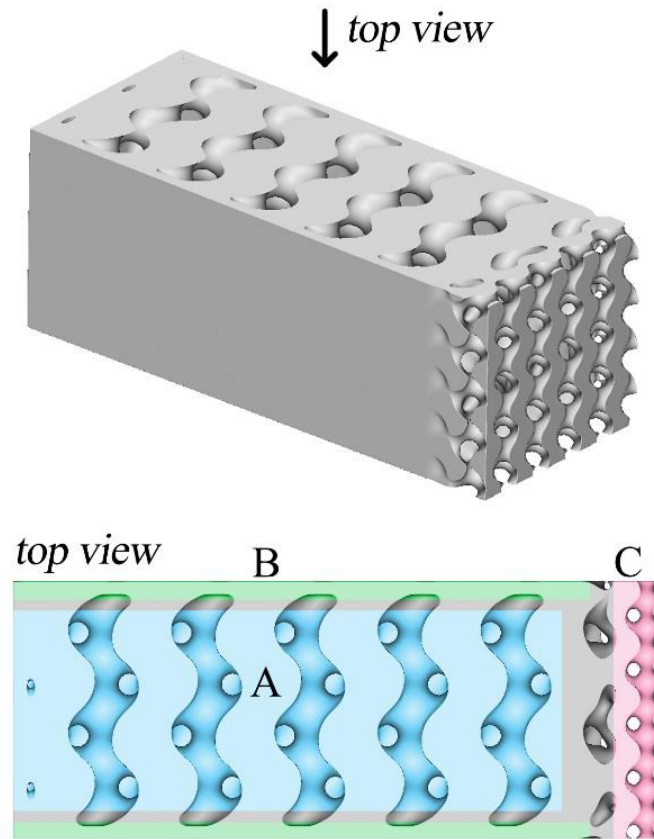
Figure 10 Gyroid hybrid lattice structure: A – designed following an elastic matching approach; B – Solid interface; C – region designed to maximize osseointegration.

The Gyroid's hybridization allows to create, within a single body, regions with different geometric and mechanical properties able to meet the specific biomechanical requirements for elastic matching and osseointegration and yet maximizing manufacturability via Additive Manufacturing.

The following chapter will cover the practical aspects of the implementation of the Gyroid lattice within a framework to design custom implants: first, a method to design and manipulate such structure within a CAD software will be introduced, then will follow the discussion of the biomechanical requirements necessary to fulfill the mechanical, biological and technological constraints. Eventually, the ideal parameters for orthopedic applications of the Gyroid structure will be presented.

2 Gyroid design

The Gyroid lattice was designed with nTop Platform [81] based on implicit modelling [82]–[86]. nTop software allows for an effective integration of CAD tools, required to design a personalized device based on the anatomy of the patient, and CAE functionalities (e.g., FEM, topology optimization), useful to implement a performance-driven design oriented to mass reduction. Moreover, thanks to an advanced implicit Geometric Modeling Kernel, nTop empowers the designer with a series of tools for the definition of complex structures that overcome the common limitations of the traditional CAD packages based on B-Reps in representing and manipulating large lattice components.

Most CAD systems rely on B-Reps (Boundary Representation) to express the shapes of solid objects. As the name implies, a boundary representation is a collection of faces that form the boundary (the outer skin) of the object by combining vertices, edges and faces. The main drawback of such method is the computational cost of very complex geometries, since the geometric entities required to describe the external shape can become very numerous and difficult to manage. The second main disadvantage of the traditional design approach is that some operations as fillet, offset and Booleans are highly prone to failure because, especially in case of design automation, the topology of the solid may change and new sets of curves must be extrapolated at each iteration. In implicit modelling, bodies are represented by implicit functions through SDFs (Signed Distance Field). A 3-D surface is characterized by a set of points $f \in R^3$ satisfying $f(x,y,z) = 0$; accordingly, the solid body is represented by the inequality $f(x,y,z) < 0$, thus no geometric entities must be calculated, and a 3D body can be represented by a single equation, which is extremely efficient, especially for complex geometries.

An example of the user interface of nTopology for gyroid lattice design is presented in Figure 11.
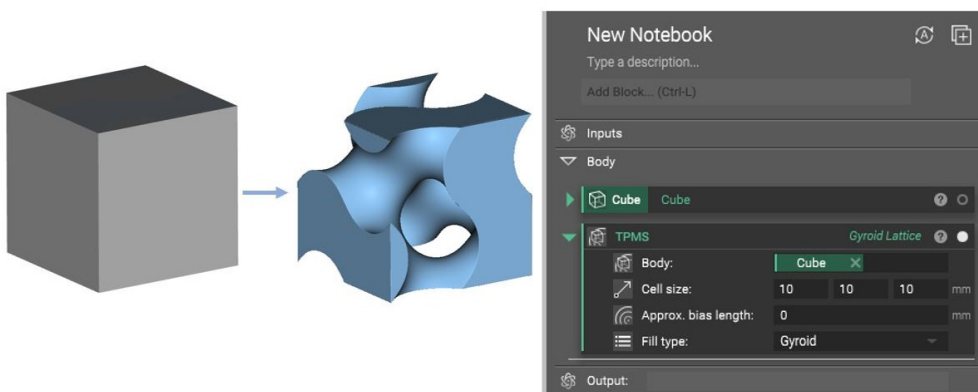
Figure 11 nTopology GUI

To assess the dimensional accuracy of nTopology, the gyroid Equation and hybridization have been implemented in MATLAB® 2019b for a geometric comparison. The results are depicted in Figure 12.
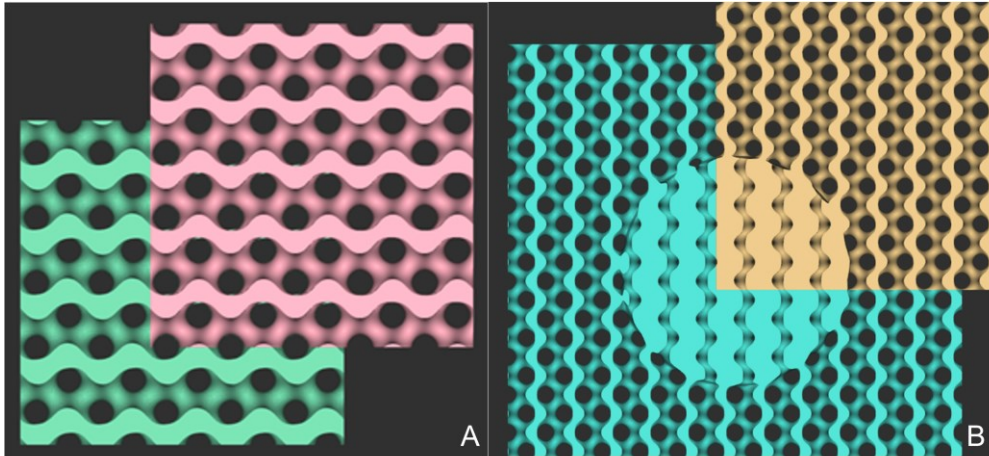
Figure 12 Comparison between MATLAB and nTopology. 10 a) in green the Gyroid surface designed in MATLAB, in red in nTopology. 10 b) in green the hybrid Gyroid surface with cylindrical transition designed in MATLAB, in yellow in nTopology.

As shown by the picture above, the output geometries of the two methods are perfectly overlapping and allow for the same level of accuracy and dimensional control, also for hybrid surfaces. In Figure 12 a) are depicted two gyroid surfaces with the same parameters, generated with MATLAB, in green, and with nTopology, in red. In Figure 12 b) a comparison of two hybrid surfaces with a cylindrical transition region; the MATLAB and nTopology surfaces are represented, respectively, in green and yellow.

Thanks to a lower computational time and a higher flexibility nTopology was adopted for the continuation of the research.

2.1. Gyroid mechanical properties assessment

To assess the mechanical properties of the gyroid lattice structure, and to verify the Gibson-Ashby model for cellular materials, a compressive test was simulated according to ISO 13314 [87].

A series of cubic samples with gyroid lattice infill have been designed and virtually tested through FE analyses in order to retrieve the case-specific constants C_l and n of Equation 6.

The cubic samples, presented in Figure 13, were designed with 50mm edge length and 10mm gyroid cell size; the only variable was the relative density (Equation 4) of the gyroid structure, which was namely 0.3, 0.4, 0.5, 0.6, 0.7.
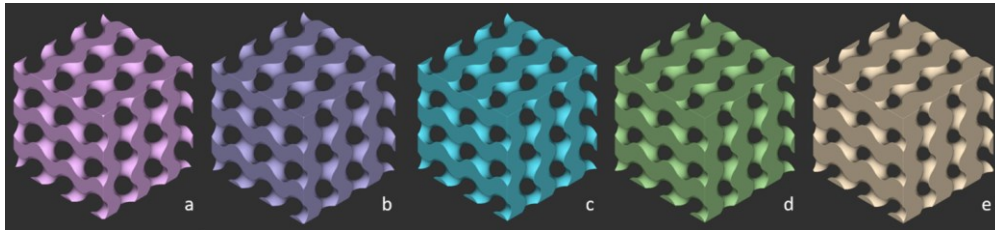
Figure 13 Five samples with 10mm cell size with increasing relative density. a) ρ_{rel} =0.3 b) ρ_{rel} = 0.4 c) ρ_{rel} = 0.5 d) ρ_{rel} = 0.6 e) ρ_{rel} = 0.7

The compression test was simulated with Ansys Workbench ® 2019r3 [88]. The simulation setup is depicted in Figure 14.
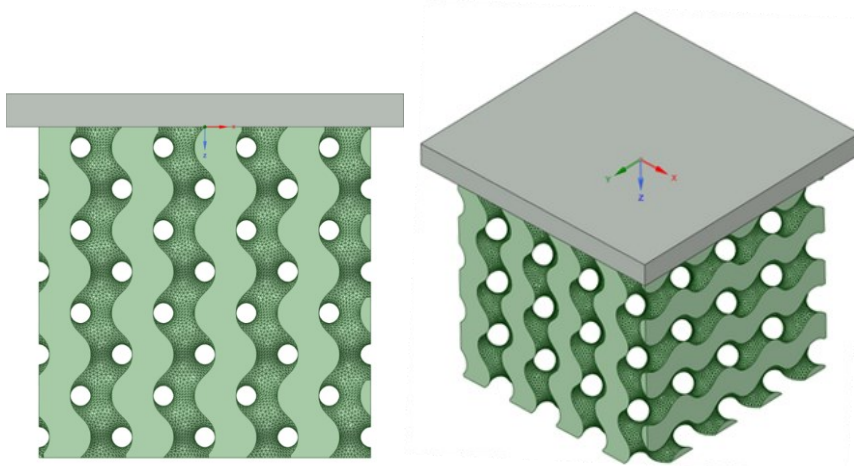
Figure 14 Compression test simulation setup in Ansys Mechanical

The samples have been meshed with tetrahedral volume elements with 0.6mm element size, according to the result of a convergence test performed to determine the optimal element size, and the material assigned was Ti-6Al-4V with Young's modulus of 110 GPa The compressive load was applied in the Z direction to a rigid plate in frictionless contact with the upper surface, while the lower surface was fixed along Z. To avoid unwanted deformations and rotations, two points in the lower face were bound to move respectively along the X and Y axes. According to the ISO 13314 norm for cellular materials, a compressive force was applied to calculate displacement and elastic modulus of the samples. Five levels of compressive force have been applied to assess the consistency of the Gibson-Ashby model.

Displacements and stresses increase coherently with the compression force, according to the related literature [62], [74], [89]–[91].

The results of the compression tests are resumed in Table 1.

V/V$_s$	E [GPa]
0.3	6.76
0.4	13.01
0.5	21.6
0.6	32.69
0.7	46.42

Table 1 Compression test results for cubic samples with gyroid lattice infill with increasing relative density

The elastic modulus of the structure was plotted with respect to the relative density for each cubic sample; the curve was interpolated with MATLAB in order to calculate the constants C1 and n (Equation 6) of the Gibson-Ashby model [70]. The resulting interpolation curve is represented in Figure 15.
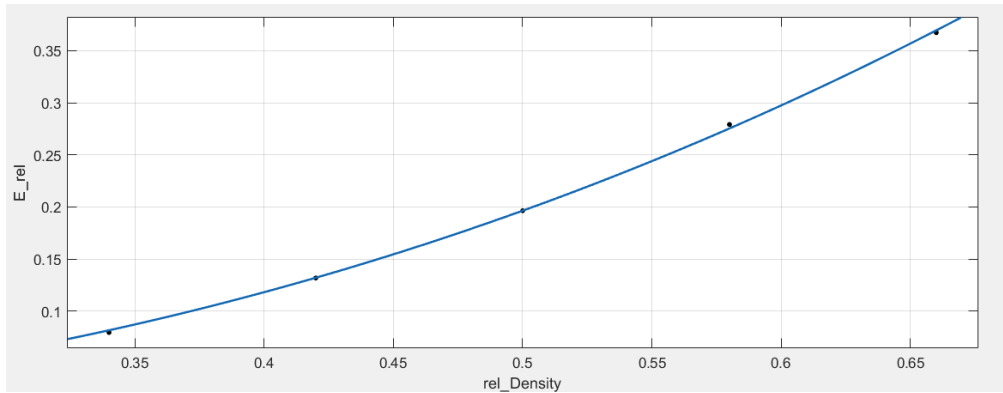
Figure 15 MATLAB interpolation of the calculated elastic modules of the gyroid samples

The resultant Gibson-Ashby model with the calculated coefficients is:

$$\frac{E}{E_s} = 0.9493 \, (\rho_{rel})^{2.273} \quad (8)$$

The model approximates the empirical values with a R$_{sqr}$ = 0,9997 and 95% confidence; the result and the coefficients are consistent with the Gibson-Ashby model [70]. This relationship allows to accurately predict the Young modulus of a cellular solid with gyroid lattice infill as a function of the relative density of the structure. Since the calculated coefficients are derived from a FE simulation they can't be applied in a real-life scenario and should be derived from actual compression test of additively manufactured samples instead. Several studies calculated the Gibson-Ashby model coefficients and proved that the results are highly dependent to manufacturing technology and parameters [52], [79], [92]–[95], thus it is crucial, to obtain a reliable model, to repeat the compression test of the gyroid samples with each Additive Manufacturing equipment.

Further analyses have been performed over the gyroid structure, in order to assess its behavior while subject to multi-axial compression. A cell homogenization approach [96], [97] was followed to calculate the mechanical properties of a single-cell gyroid lattice. The cell homogenization was calculated within the software nTopology, which provides a dedicated

tool for cell homogenization. The software calculates the homogenized elastic properties of a FE model; in particular, a unit strain is solved for in X, Y, Z, XY, XZ, and YZ directions, and the results are used to calculate the equivalent elastic properties of a unit cell in the form of a general 6 x 6 elasticity tensor. The result for a gyroid unit cell with ρ_{rel}=0.4 made of Ti-6Al-4V is presented in Figure 16, where the directional elastic modulus of the gyroid unit cell is represented. Figure 16 b) is nearly a sphere, which means that the elastic modulus of the Gyroid unit cell (Figure 16 a)) has approximately the same elastic modulus when compressed along every direction. As highlighted by the picture, the gyroid cell exhibits a nearly isotropic behavior, as there is a slight difference between maximum (2.1 GPa, represented in red along the diagonal) and minimum (1.9 GPa, represented in blue) values.
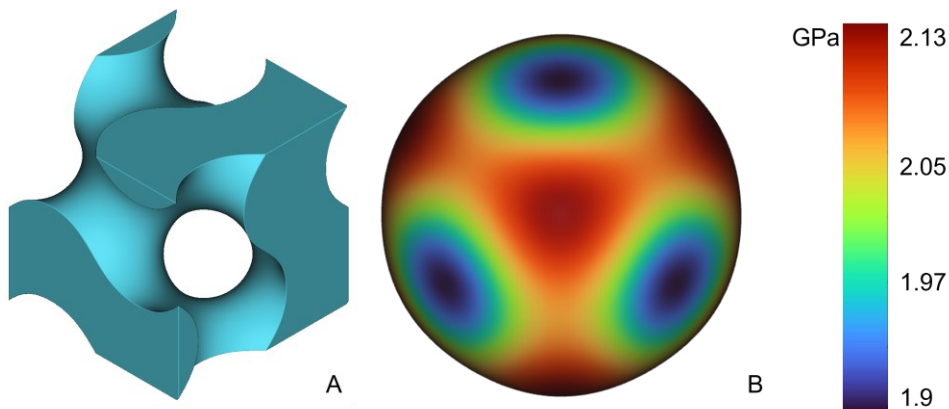
Figure 16 Gyroid cell homogenization. a) Gyroid unit cell; b) directional elastic modulus

For the sake of clarity, a non-isotropic cell is presented in Figure 17, which shows a great mismatch between maximum and minimum values. If compressed along the diagonals the cubic cell exhibits an elastic modulus much lower than along the x, y and z direction.
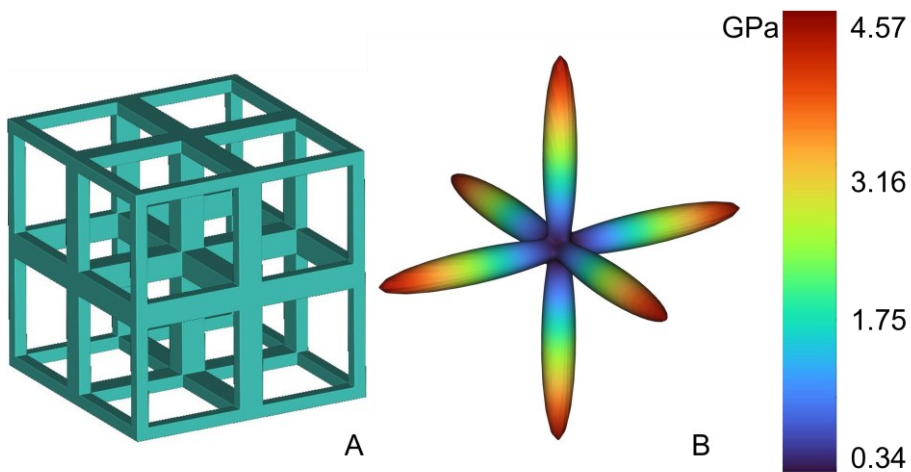
Figure 17 Non-isotropic unit cell homogenization a) Cubic unit cell; b) directional elastic modulus

2.2. Gyroid parameters for load-bearing orthopedic implants

An orthopedic implant for bone replacement must be designed to have good strength and a lattice structure which allows to closely match the stiffness of the bone to minimize stress-shielding effects [31], [61]. The lattice structure itself should provide a suitable environment for bone ingrowth, thus creating a long-lasting strong bond between bone and implant. Osseointegration is conveyed by a combination of physiological processes: cell seeding, vascularization and bone growth. Cell seeding is strongly affected by the available surface area for cell adhesion and is promoted by a low permeability; vascularization and bone growth, instead, require a good permeability to allow nutrients to flow through the structure [31], [61], [63], [98]. For an orthopedic implant is crucial to identify the best trade-off in terms of lattice architecture, pore size and interconnectivity, in order to maximize bone ingrowth. Figure 18 synthetizes these concepts.
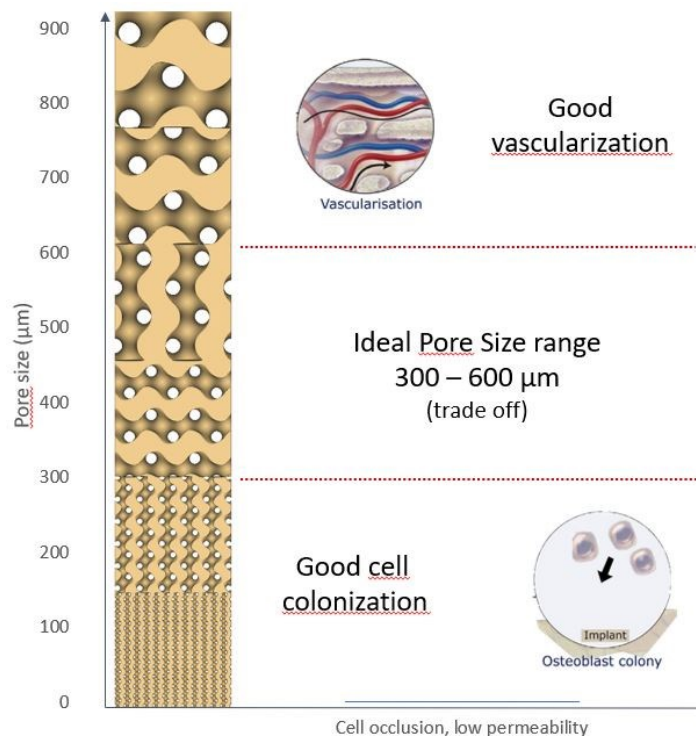
Figure 18 Pore size range for osseointegration

The ideal pore size is between 0.3 and 0.6 mm, which is the best compromise between cell colonization and vascularization, while a high pore interconnectivity and a high surface/volume ratio positively affect bone growth and osseointegration.

The gyroid lattice, due to the high surface/volume ratio, pore interconnectivity, absence of straight lines and edges, is the ideal candidate for bone replacing implants [62], [99]. Its simple mathematical representation allows to easily define the geometric and mechanical properties of the lattice structure to match, at the same time, the mechanical properties of the bone for stress-shielding mitigation and the geometric ideal features for osseointegration [100].

Considering an elastic modulus of 17GPa for the bone, the resulting geometric parameters of the gyroid lattice for elastic matching and bone integration can be derived from Equation 3 and 8:

- E= 17 GPa
- ρ_{rel}= 47.5
- pore size = 0.6 mm
- Cell size=2.3 mm

Far from the bone-implant interface the osseointegration constraint can be relaxed [100], thus the gyroid cell size can be arbitrarily increased to maximize manufacturability through Additive Manufacturing; since the pore size is no longer a concern, it might be convenient to choose a lattice with large pores to simplify post-processing operations; the values chosen are:

- E= 17 GPa
- ρ_{rel}= 47.5
- pore size = 1.8 mm
- cell size= 15 mm

3. Implant design automation

Dealing with the design of personalized medical devices, mass production is not an option that can be hypothesized. Indeed, a cumbersome production process must be considered in such cases, mainly to account for a delicate design phase that needs to take into consideration, as input, an anatomy as well as surgical needs that vary from case-to-case.

Several case studies, provided by the department of oncological orthopedics of Careggi hospital have been analyzed to get an insight of the design process of a custom pelvic implant and find the repetitive operations to be optimized and automated. 20 case studies have been considered, which included a wide variety of oncological cases as well as revision implants. The design process can be summarized as follows:

1. Virtual anatomical reconstruction (acetabular parameters, mesh repair)
2. CAD modelling of the implant shape
3. Lattice infill design

Figure 19 resumes these three phases.
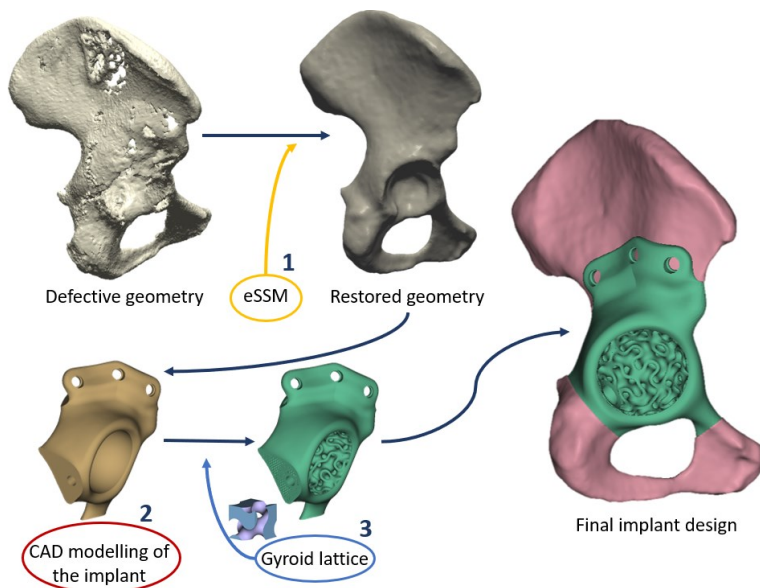
Figure 19 Three steps for custom implant design

The goal of this Ph.D. is to speed up the design phase of custom orthopedic devices by providing healthcare givers and engineers a set of automatic tools able to cover each phase of the process and avoid time-consuming and error-prone manual operations. The first area of

intervention was the development of an automatic workflow for virtual anatomical reconstruction, named eSSM (enhanced Statistical Shape Model), based on Statistical Shape Analysis, then followed the implementation of a series of CAD algorithms for implant design automation and Gyroid lattice infill creation. In the following sections the developed tools for design automation will be discussed.

3.1. Virtual anatomical reconstruction automation

In most oncological cases the target anatomy might be severely damaged and deformed by the pathology. Since the primary function of a pelvic implant is the limb functionality restoration, in most cases the implant doesn't reproduce the exact original anatomy; conversely, the acetabular region receives more importance to ensure satisfaction of functional requirements. An example is provided by Figure 20, where the pelvic implant only restores the acetabulum, while the original anatomy has been neglected.
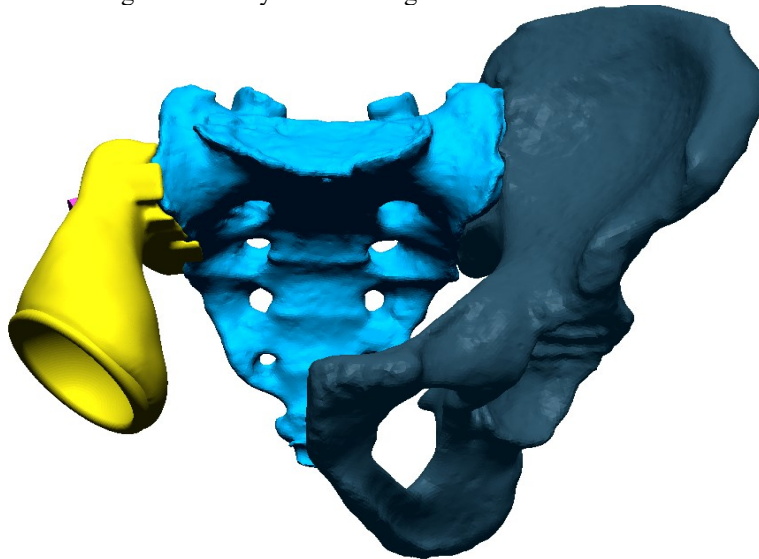
Figure 20 Pelvic implant where the original anatomy is neglected, and only the acetabulum has been restored

In case of large bone defects, in particular when the articular Center Of Rotation (COR) is no longer in its natural location, the very first operation is to retrieve the right acetabular center and orientation in order to guarantee ad adequate leg length and limb kinematics. The acetabular COR and orientation are defined as the coordinates of the center or rotation of the hip joint, and the orientation of the plane through the acetabular rim, as depicted in Figure 21.
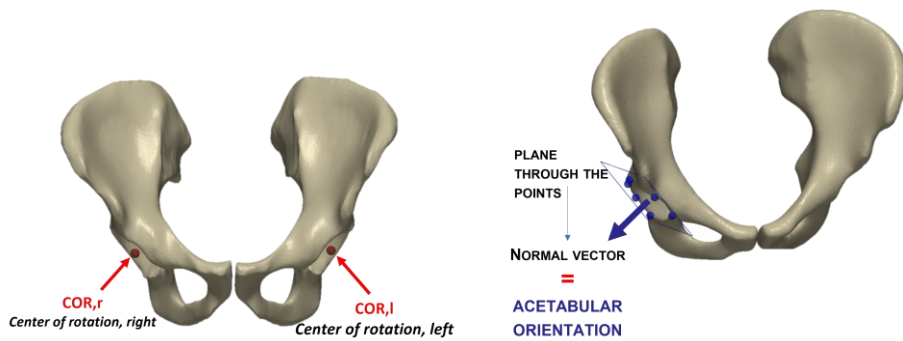
Figure 21 Acetabular COR and orientation

Typically, the COR and acetabular orientation are calculated by expert users by mirroring the healthy COR, whenever possible, though is a time-consuming and error-prone operation. Moreover, in case of large bone defects, like the one in Figure 22, the anatomical model must be manipulated and corrected to obtain a reference geometry for implant design.
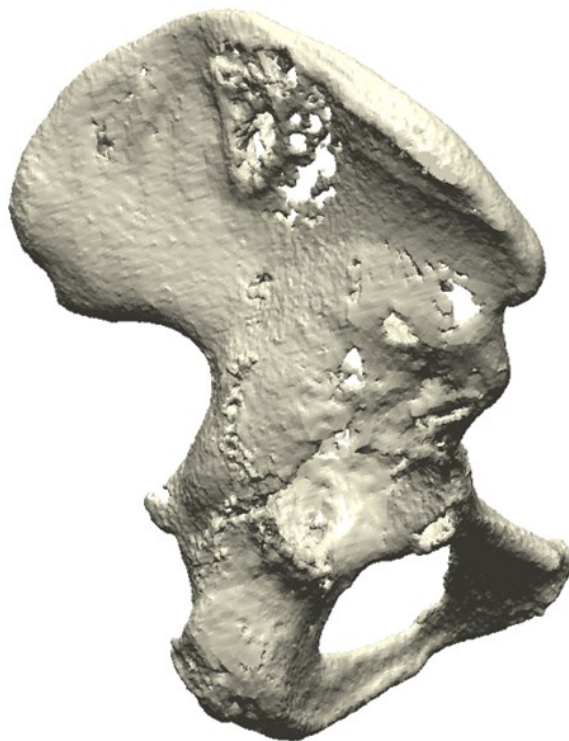
Figure 22 Hemipelvis with large bone deficiencies and deformed COR

With the objective of implant design automation, an automatic tool for anatomical reconstruction have been developed, based on Statistical Shape Analysis.

Statistical Shape Analysis (SSA) [101]–[105] is an established method widely employed to provide a quantitative description of the geometrical characteristics of a specific family of shapes.

When applied to the study of anatomical shapes, SSA allows to synthetize and analyze the information provided by a training set composed by an adequate number of healthy samples of the region of interest (ROI). In its classical formulation, SSA works on a set of training samples provided as discrete models (usually, Point Distribution Models – PDM [104]): the training dataset is then defined as the list of the spatial coordinates of each point of the samples. By assuming all the training samples to be in correspondence (i.e., analogous points are reported in the same positions), SSA exploits powerful mathematical tools, such as multivariate statistical analysis, to interpret and synthesize the information delivered by the training dataset about the possible shape variations from a mean shape. SSA results in a generative parametric model, usually referred to as Statistical Shape Model (SSM), able to describe the family of shapes under consideration and to "summarize" them under a parametric model.

Exploiting its ability to encode an a-priori knowledge of the healthy shape of the ROI, SSM is usually employed as a source of templates for 3D medical image segmentation [104], [106], for the reconstruction of deformed or defective models [101], [107], [108] and for dysmorphisms and asymmetries recognition and evaluation [109]–[111].

Indeed, the design of patient-specific devices would be made easier by an access to a collection of statistical information of geometrical descriptors and landmarks of the ROI that goes beyond the mere surface data. Such database would increase the efficiency of the design process by providing easy-to-access information on various geometric characteristics, improving the typical approach which only exploits sur-face information.

In the application scenario considered, the pelvis, the use of an enhanced SSM (eSSM) would be beneficial whenever the anatomical structure of the acetabulum is severely damaged, and an implant is required. In such cases, the first step is typically the retrieval of the missing geometry and the computation of the natural articular Center Of Rotation (COR) to restore the limb functionality. While the first operation can be affectively carried out automatically by a typical SSA (which calculates the missing geometry according to the highest probability), manual operations are required to retrieve the COR [112]. When the contralateral acetabulum is healthy the most common approach is to mirror its COR, though such method fails when an implant or a bi-lateral defect is present; in addition, the mirroring approach is an important approximation, since the symmetry in human anatomy is only an abstraction and a perfectly symmetric anatomy does not actually exist. The use of an eSSM makes this step automatic, by building an SSM that encompasses the positions of the CORs as learned from the dataset.

The information enclosed within the eSSM presented in the following, are namely the articular centers of rotation and the acetabular orientation.

3.1.1. Classical Statistical Shape Analysis and proposed improvements

The mathematical framework of the SSA is strongly affected by the representation of the training samples; in this work, the classical approach based on the Principal Component Analysis (PCA) was applied on the training samples provided as PDM is considered.

PDM is the most convenient representation of a complex geometry [113], consisting of a discrete description based on landmarks distributed across the surface [104], [114]. In the following, M will be defined as the number of the training samples, and N as the number of

points of each training sample. All the training samples have the same number of points because, as said, it is mandatory that they are in correspondence: in the related literature, many approaches to create a suitable training set are described [115].

With the just described assumptions, each training shape Γ^i can be represented as a discrete set of landmarks x^i:

$$\Gamma^i = \left\{ \mathbf{x}_k^i \middle| \mathbf{x}_k^i \in R^3, k = 1, \dots, N \right\} \ (9)$$

Referring to Equation 9, in typical SSA approach x_k^i contains the Cartesian coordinates, in three dimensions, of the k-th point. Γ^i is then a 3xN matrix.

Each shape Γ^i is rearranged by stacking the coordinates of each point k in a large (3N elements) column vector $\vec{x}^i$. Considering the global reference system in x-, y- and z-axis:

$$\vec{\mathbf{x}}^i = \left[x_1^i \ x_2^i \ \dots \ x_N^i \ y_1^i \ y_2^i \ \dots \ y_N^i \ z_1^i \ z_2^i \ \dots \ z_N^i \right] \ (10)$$

As a result, the column vector reported in Equation 10 represents the 3N variables of the single observation Γ^i.

The whole training set (TS) has to be then organized in a 3NxM matrix whose columns are the observations (i.e., the M shapes) and rows are the variables:

$$\mathbf{TS} = \left[\vec{\mathbf{x}}^1 \ \vec{\mathbf{x}}^2 \ \dots \ \vec{\mathbf{x}}^M \right] \ (11)$$

Once the dataset **TS** is properly defined, and assuming that the family of shapes under consideration is a linear space of R^{3N}, new shapes can be generated by linear combinations of the training samples:

$$\mathbf{x} = \bar{\mathbf{x}} + \sum_{m=1}^{c} \alpha_m \sqrt{\lambda_m} \varphi_m \ (12)$$

Where:

- $\bar{\mathbf{x}}$ is the mean shape defined as:

$$\bar{\mathbf{x}} = \frac{1}{M} \sum_{i=1}^{M} \vec{\mathbf{x}}_i \ (13)$$

- λ_m and φ_m are, respectively, the eigenvalues and eigenvectors resulting from the eigendecomposition of the covariance matrix S:

$$\mathbf{S} = \frac{1}{M-1} \sum_{i=1}^{M} (\vec{\mathbf{x}}_i - \bar{\mathbf{x}}_i)(\vec{\mathbf{x}}_i - \bar{\mathbf{x}}_i)^T \ (14)$$

A PCA-based approach is typically used to provide the eigendecomposition on **S** delivering the principal Modes of Variation (MoVs) Φ_m (eigenvectors of the matrix **S**) and their respective variances λ_m (eigenvalues of the matrix S) estimated on each point $\mathbf{x}_k$ of the initial dataset **TS**. PCA returns the plausible deformations, delivered as directions (Φ_m) and related amplitudes (λ_m) of displacement, of every single point of the mean shape. λ_m and Φ_m are ordered by their variances so that $\lambda_1 \geq \cdots \geq \lambda_{M-1}$.

- $\alpha \in R^M$ is a coefficient vector that permits to constrain the allowed variation to plausible shape; usually, α is delimited in the range [-3;+3], which corresponds to a deformation that is 3 standard deviations away from the mean (α =0 means that the model is equal to the mean shape).
- c represents the number of significant eigenvalues. In the presented application, c is defined so that the accumulated variance (the numerator of Equation 15) reaches a certain ratio r of the total variance (the denominator of Equation 15). Common values of r are between 0.9 and 0.98 [116]. In this work, r was chosen equal to 0.98 because the training sample is relatively small, thus a large value of r doesn't affect the computational time.

$$\frac{\sum_{i=1}^{c} \lambda_i}{\sum_{j=1}^{M-1} \lambda_j} = r \ (15)$$

As Equation 12 shows, SSA results in a mathematically convenient representation of the information contained in the training dataset: such representation is delivered as a parametric model able to generate new consistent set of data simply varying the parameters of α.

In the typical approach, the set of data is represented, as said, by only the spatial coordinates of the training samples. As a result, Equation 14 is able to return pathologically unaffected geometries belonging to the same family of shapes forming the training set. Such model can be used, for example, to infer the full shape of the defective anatomy to be restored [101].

In this work, the described approach is improved expanding the information enclosed in the SSM. Regarding the information contained in the training set, the vector $\vec{x}^i$ can be expanded by including not only the spatial coordinates of the points describing Γ^i, but also those of significant other points such as a joint center, the direction of load applications and so on.

By defining n more points in addition to the N points used to describe the shape, Equation 9 becomes Equation 16.

$$\Gamma^i = \left\{ \mathbf{x}_k^i \middle| \mathbf{x}_k^i \in R^3, k_i = 1, \dots, N, N+1, \dots, N+n \right\} (16)$$

As discussed, the added points must be in correspondence across all the Γ^i too. Starting from the enlarged training samples, the SSA follows the subsequent steps as described above.

An additional approach that could be followed to enhance the SSM could be based on the introduction of additional information in the already built mean shape. While the points composing $\bar{\mathbf{x}}$ remain the same, additional information could be associated to each point using labels, weights, and other parameters. By following this strategy, the mean shape and the SSM remain the same, as they are built using the same dataset.

This information could be, as an example, the indication to which region of the semantic segment each point belongs, or the position of significant landmarks. Such additional information can be effortlessly added after the definition of the SSM directly on the mean shape instead of on each training samples. In this case, and considering the most generic case presented in Equation 16 the mean shape can be defined as:

$$\bar{\mathbf{x}} = \left\{ \bar{\mathbf{x}}_k \middle| \bar{\mathbf{x}}_k \in R^d, k_i = 1, \dots, N+n \right\} (17)$$

where *d* is defined as an integer greater than or equal to 3.

As a consequence, the so obtained eSSM allows, in the first case, to synthetize more geometric information than the mere shape and, in the second case, to encompass more information about each point of the mean shape in addition of its spatial position. This information will be inherited to the restored shape when the eSSM is used to infer the full shape of the defective model.

3.1.2. The e-SSM implementation

The implemented e-SSM was trained with 50 healthy pelvises downloaded from an open-source repository of anonymized medical images (the CT images collection is called '*Pelvic Reference Data*') [117]. For this work, there was no distinction between sex or age, though the presented reliable automatic procedure will allow, in the future, to refine the model and differentiate between sex, ethnicity and so on as soon as the number of cases composing the dataset would guarantee an adequate variability to perform such differentiations. The CT scans have been manually segmented by an experienced user with Materialise® Mimics 23.0 to extract the external shape and the acetabular CORs; each COR was considered coincident with the center of a sphere fitted to each femur head.

The SSA is performed by an in-house automatic algorithm developed in MATLAB®. Such algorithm is based on the one presented in [106], properly improved to deliver the eSSM.

The input data of the algorithm are the triangular mesh of the complete pelvis and the coordinates of the CORs. In the first stages, the algorithm automatically finds the correspondences between the training samples and re-arranges the resulting dataset to obtain $\vec{\mathbf{x}}^i$ (Equation 16) and **TS** (Equation 11). In this application, the column vector $\vec{\mathbf{x}}^i$ contains both the spatial coordinates of the shape descriptors as well as the positions of the CORs for the training sample Γ^i. As a consequence, by defining $x_{RC}^i\, y_{RC}^i\, z_{RC}^i$ and $x_{LC}^i\, y_{LC}^i\, z_{LC}^i$, respectively, the right and left COR spatial coordinates, $\vec{\mathbf{x}}^i \in \mathrm{R}^{3N+6}$ can be defined as:

$$\vec{\mathbf{x}}^i = \left[x_1^i\, x_2^i\, ...\, x_N^i x_{RC}^i\, x_{LC}^i\, y_1^i\, y_2^i\, ...\, y_N^i y_{RC}^i\, y_{LC}^i\, z_1^i\, z_2^i\, ...\, z_N^i z_{RC}^i\, z_{LC}^i \right] \quad (18)$$

After the creation of the matrix **TS**, the algorithm performs the described PCA-based SSA including the CORs. The result of the automatic procedure delivers the mean shape and the mode of variation of the pelvis and CORs as learned from the variability of the initial models. Figure 23 shows the first two modes of variations from the maximum negative (α=-3) to the maximum positive (α=+3) amplitude. α=0 is equal to the mean shape.
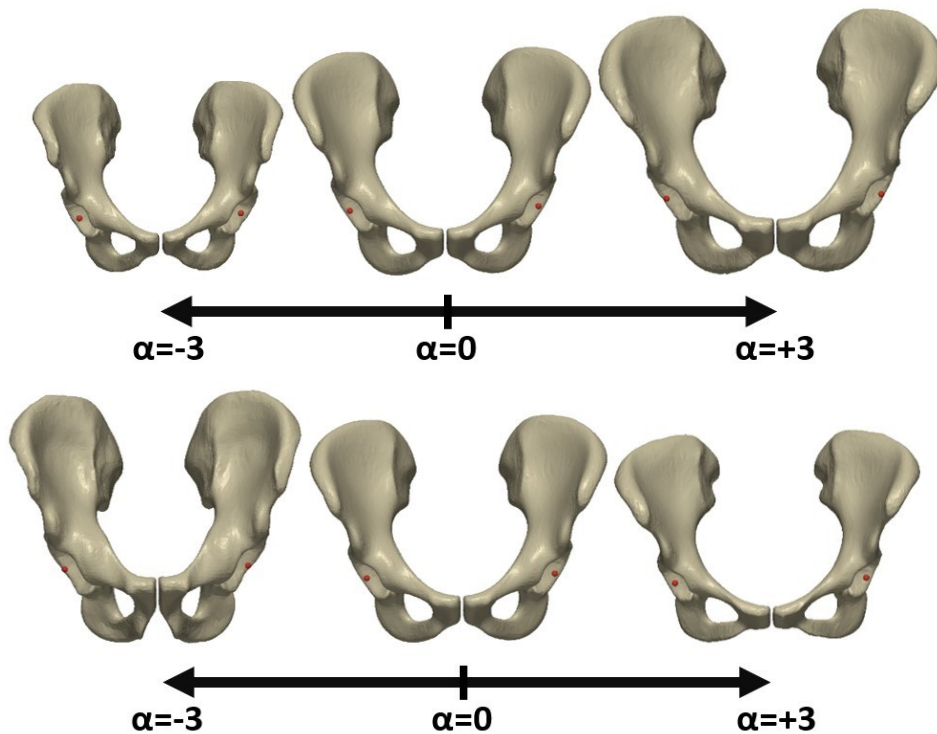
Figure 23 First two modes of variation of the pelvis with the CORs depicted as red dots (the first mode of variation is reported in the upper row)

On the obtained mean shape, an expert user has selected significant landmarks and the points pertaining to a semantic segmentation of the pelvis (e.g., Figure 24 a)). Such landmarks represent points of application of loads and constraints which could be exploited to create a FE model of the pelvis including ligaments and boundary conditions. Additionally, the user has selected the points shown in Figure 24 b) on the acetabular rim, useful to define the acetabular orientation.
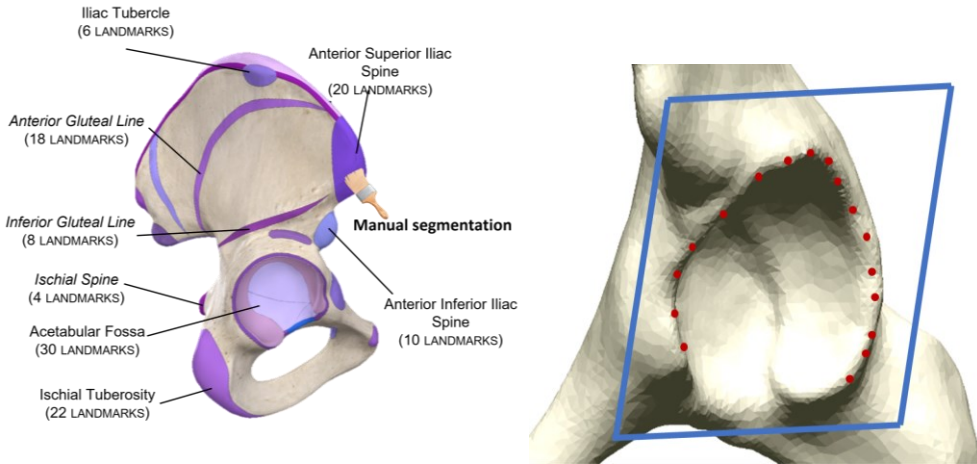
Figure 24 a) Semantic segmentation of the pelvis: the areas highlighted in the figure define meaningful regions with the relative number of landmarks employed. b) selection of the points on the acetabular rim performed by the user.

Operationally speaking, this additional information will be added to the $\bar{\mathbf{x}}$ vector of the mean shape as in Equation 17, expanding the dimensionality of each $\bar{\mathbf{x}}_k$. The kind of information delivered is defined by the position in the $\bar{\mathbf{x}}_k$ vector. Each segmented region is saved as a new PDM, while the coordinates of each selected landmark are exported as text file. This way, the developed algorithm can automatically store the additional data on the proper point of the mean shape by comparing the position within the vector of each point with the positions of the points selected by the user.

The eSSM mean shape vector can be represented, for the sake of clarity, as a matrix, as pointed out in Figure 25, where can be notice in green the traditional SSM mean shape, in red the coordinates of the additional points and in violet the labels.

$$\textbf{MEAN SHAPE - eSSM} \quad e\bar{\Gamma} = \begin{bmatrix} x_1 & y_1 & z_1 & f_1 & \cdots & g_1 \\ x_2 & y_2 & z_2 & f_2 & \cdots & g_2 \\ \cdots & \cdots & \cdots & \cdots & \cdots & \cdots \\ x_N & y_N & z_N & f_N & \cdots & g_N \\ x_{N+1} & y_{N+1} & z_{N+1} & f_{N+1} & \cdots & g_{N+1} \\ \cdots & \cdots & \cdots & \cdots & \cdots & \cdots \\ x_{N+n} & y_{N+n} & z_{N+n} & f_{N+n} & \cdots & g_{N+n} \end{bmatrix}$$

additional rows
(to add meaningful points)

additional columns
(to add information associated to each point)

Figure 25 eSSM mean shape matrix. In green the classical SSM mean shape; in red the additional points for eSSM and in violet the point labels.

In this application, the positions within the $\bar{\mathbf{x}}_k$ vector are defined as follows:

• the first three columns are reserved for the x- y- and z- spatial coordinates of the global reference system

• in the fourth column, a scalar index defines the attribution of the point to a specific labelled region. As an example, a value of 1 defines all the points belonging to the iliac crest, a value of 21 defines the anterior gluteal line, etc.

• the fifth column is a binary variable that equals to 1 if the point has been selected as an acetabular rim point and to 0 otherwise

As a consequence, in the case addressed $\bar{\mathbf{x}}_k \in \mathrm{R}^5$. The $\bar{\mathbf{x}}_k$ vector is then obtained by concatenating respectively the x_N, y_N and z_N coordinates.

When this eSSM is used to infer the full shape of the defective model to be restored, the deformation process affects only the first three positions of the $\bar{\mathbf{x}}_k$ (i.e., the spatial coordinates of the point), while the other information remains unchanged. Therefore, all the additional information stored in each point of the mean shape will be inherited by the restored model.

The developed eSSM has been tested over severely damaged anatomies not belonging to the training set and delivered consistent results with a good approximation.

A representative example is depicted in Figure 26.
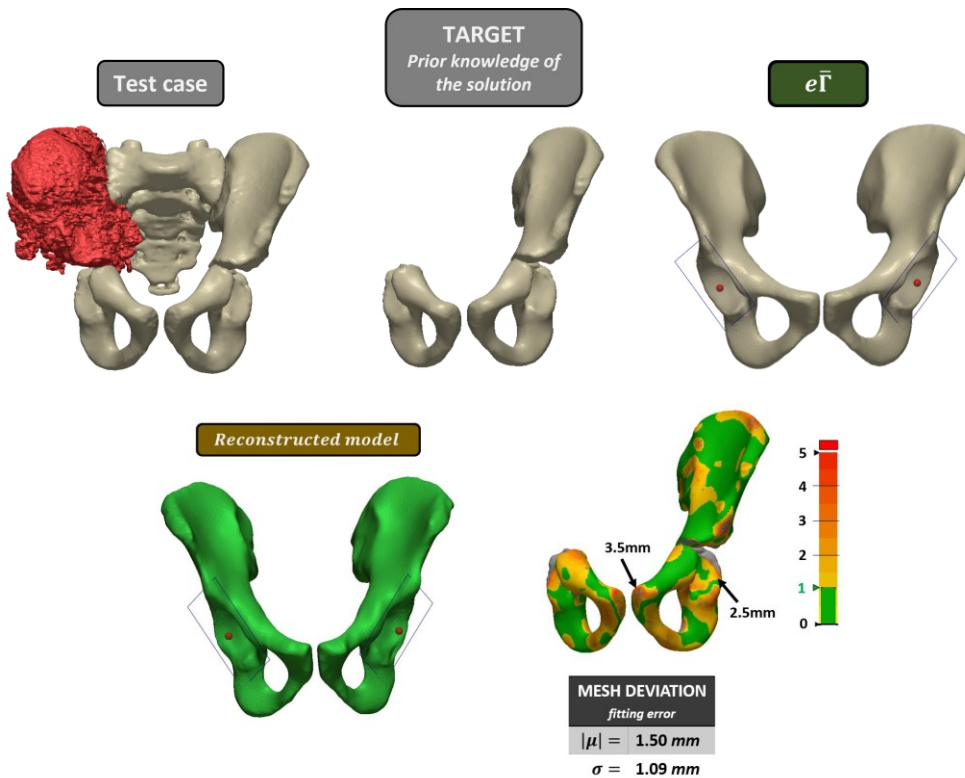
Figure 26 eSSM applied to reconstruct a highly defective pelvis

In the presented example a highly defective pelvis was considered. The eSSM managed to automatically reconstruct a coherent shape with and average error of 1.5mm, which is adequate for the application, along with the acetabular COR and orientation. The

reconstruction accuracy can be further improved by increasing the training set number, which to date is composed of 50 pelvic models.

The repaired mesh and the acetabular COR and orientation will be used as inputs for the next phase of implant design; in particular, the polygonal mesh will be used to define the coarse implant's external shape, while the acetabular coordinates will drive the design of the acetabular cup.

3.2. Implant CAD modelling automation

In this section two automatic procedures will be presented to design the most common types of pelvic implants. The workflow, implemented in nTopology® [81] is designed to require few inputs and allows for a high design flexibility, in order to cover a broad range of cases.

With the support of experienced physicians from Careggi hospital, the three most common types of pelvic implant have been identified, represented in Figure 27.
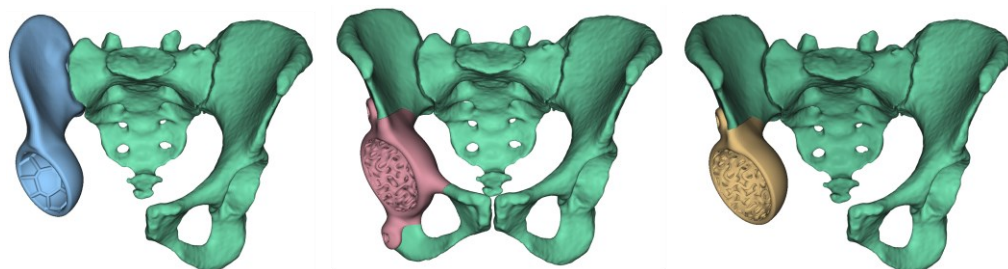
Figure 27 a) hemipelvic implant. b) acetabular implant. c) acetabular implant with removal of pelvic ring

The first example depicted, Figure 27 a), represents a hemipelvic implant; among the cases considered, is the most invasive and, due to its typical large dimensions, the lattice infill is not easily applicable for manufacturing issues, mainly for the non-sintered powder removal. The second and third cases, Figure 27 b), c) can be manufactured with a lattice internal structure instead.

Two algorithms have been implemented, with slight differences, to differentiate between implant with or without lattice internal structure

Within nTopology, based on implicit modeling, every solid body is described by a single mathematical Equation through Signed Distance Fields (SDF) [82], [83], [85], [118]. nTopology allows to create personalized, reusable workflows that are tailored to the unique requirements of the application thanks to a user interface based on block programming: by combining the robustness of implicit modelling and the programming flexibility provided by the nTopology environment, it is possible to capture the engineering workflows and create reliable and reusable automatic procedures.

In the following sections details about the implementation of the two algorithms developed will be provided. First, the hemipelvic implant will be presented along with the inputs required for the automatic procedure, then the acetabular implant will be discussed in detail.

3.2.1. Hemipelvic implant

A hemipelvic implant is necessary in case of large bone lesions, which require the removal of the whole hemipelvis and the implant of a metal device, typically linked to the sacrum through large screws. In such cases, the general tendency is to neglect an accurate reconstruction of the original anatomy to limit the prosthesis' size and weight yet preserving

the articular kinematics. Figure 28 represents the nTopology user interface with the custom function designed to generate hemipelvic implants. The function is designed to guide the user in the design process since allows to input files and variables only in the desired format (i.e. in the first row it is required to import the .STL file of the pelvic bone and so on).
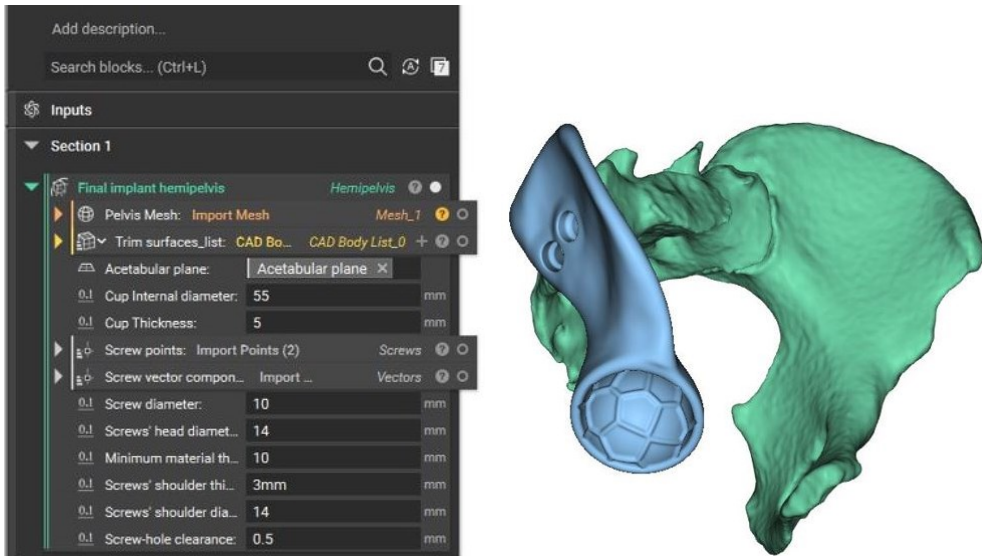
Figure 28 Custom block in nTopology for hemipelvic implants

The custom function requires a set of external inputs, highlighted in Figure 29, namely:

- polygonal mesh of the target bone (.STL)
- CAD surfaces to remove the undesired regions (.stp)
- acetabular planes' coordinates and normal (.csv)
- screws' holes coordinates and vectors (.csv)
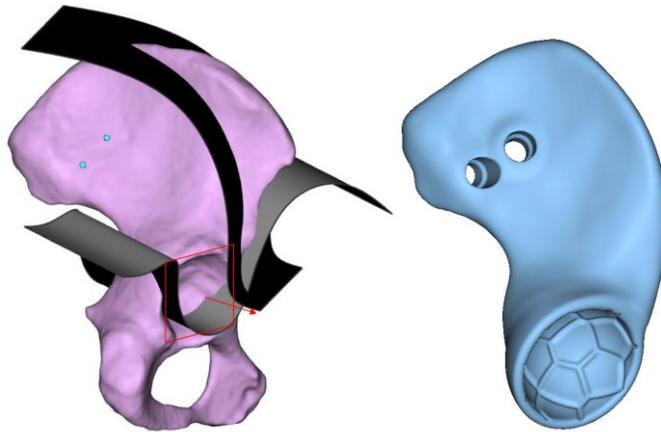
Figure 29 a) required inputs for the automatic procedure for hemipelvic implants. b) resulting hemipelvic implant

Once provided the external inputs, the procedure requires the user to set the numerical values regarding the design variables:

- acetabular cup internal diameter
- acetabular cup thickness
- screw stem diameter
- screw head diameter
- minimum material thickness of the solid part
- screw's shoulder thickness
- screw's shoulder diameter
- screw-hole clearance

After each input have been provided, the workflow automatically produces the 3D model of the hemipelvic implant. The implemented custom function encloses a series of simple functions which perform the repetitive CAD operations exploiting the effectiveness of implicit modelling in performing operations as Booleans (union, subtraction and intersection). In nTopology each basic function is represented by a block; the scripting-like workflow lets the users to properly combine and nest blocks, thus creating a re-usable procedure which captures the sequence of the repetitive operations regardless the parameters.

3.3. Acetabular implants

Acetabular implants, Figure 27 b), c), are employed in case of bone removal in the acetabular region, thus the prosthesis can be connected to the healthy bone with screws through the creation of flanges. This class of implants is designed with an internal lattice structure for stress-shielding mitigation and osseointegration, with the goal to increase implant's longevity and avoid revision surgery, which often leads to severe complications.

The custom function implemented in nTopology is reported in Figure 30.
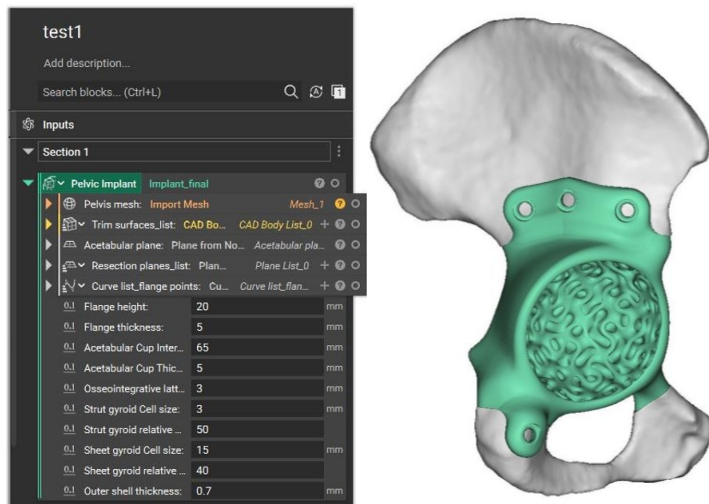
Figure 30 Custom block in nTopology for acetabular implants

The required external inputs, pointed out in Figure 31, are:

- polygonal mesh of the target bone (.STL)
- CAD surfaces to remove the undesired regions (.stp)
- acetabular planes' coordinates and normal (.csv)
- resection planes' coordinates (.csv)
- screws' holes coordinates (.csv)
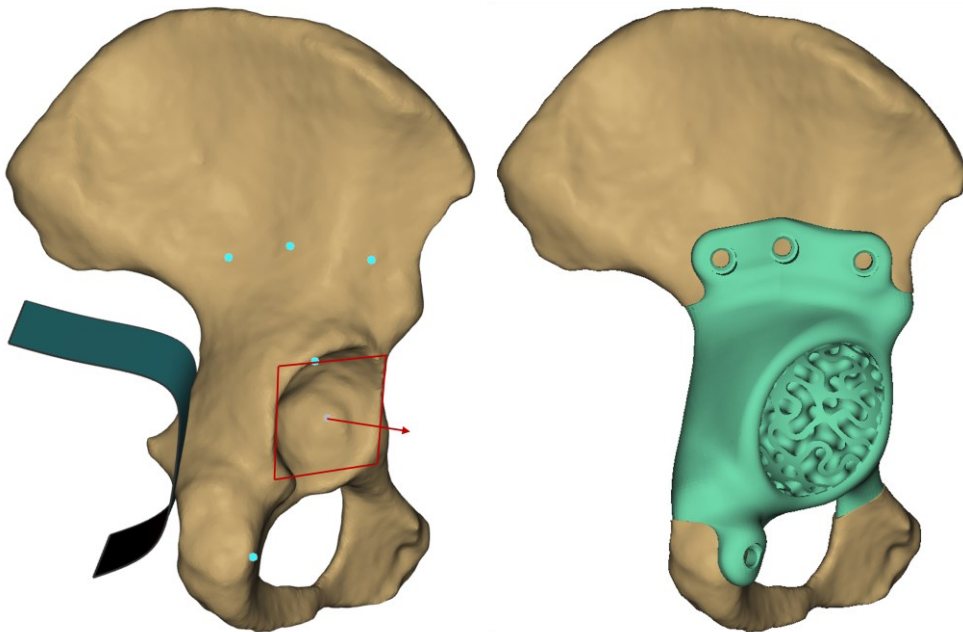
Figure 31 required inputs for the automatic procedure for pelvic implants. b) resulting pelvic implant.

Just as the previous case, the procedure requires to type the desired values for the following design variables:

- flange height
- flange thickness
- acetabular cup internal diameter
- acetabular cup thickness
- thickness of the osseointegrative lattice layer
- gyroid cell size for osseointegration
- gyroid relative density for osseointegration
- gyroid cell size for elastic matching at the implant's core
- gyroid relative density at the implant's core

In this case, due to the high variability between each case, the screws' holes are designed separately with a dedicated custom function, allowing to create as many holes as desired with different dimensions.

Two cross sections of an acetabular implant are presented in Figure 32, where the internal gyroid structure can be appreciated.
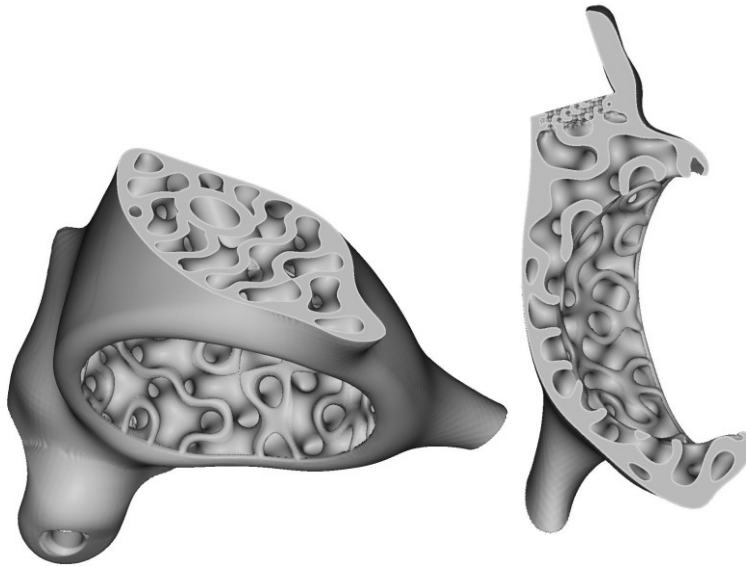
Figure 32 Cross sections of an acetabular implant with graded lattice gyroid infill

The workflow enclosed within the custom function implemented in nTopology for the acetabular implant is resumed in Figure 33. The blue blocks represent the operations, while the yellow ones stand for the intermediate results. The dotted lines show at which step each input is involved. Each operation block has been specifically developed and combined to create a robust workflow which exploits the strengths of implicit modelling. First, the pelvis polygonal mesh is converted into implicit representation for further operations; the undesired parts of the pelvis, bounded by the CAD surfaces (e.g. Figure 31 a), are removed, then the result is merged through a Boolean union with the acetabular cup. Since in most cases the original anatomy is not restored, in this framework it is convenient to remove the undesired parts of the pelvis before the process starts to guarantee a better outcome.
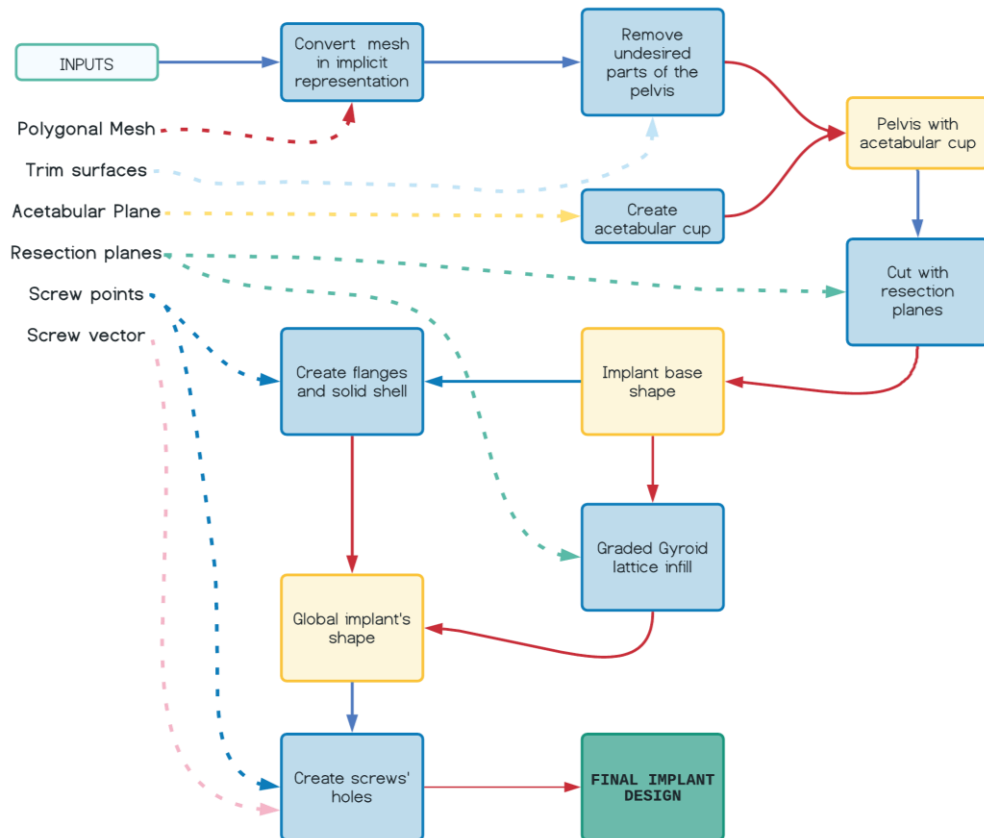
Figure 33 Acetabular implant workflow

The acetabular cup is generated taking as a reference the acetabular plane and the acetabular COR provided by the eSSM. The software allows to impose a blend radius during Boolean operations to create a smooth transition, thus creating the "Pelvis with Acetabular Cup" (PAC), showed in Figure 34, which will be exploited in the following.
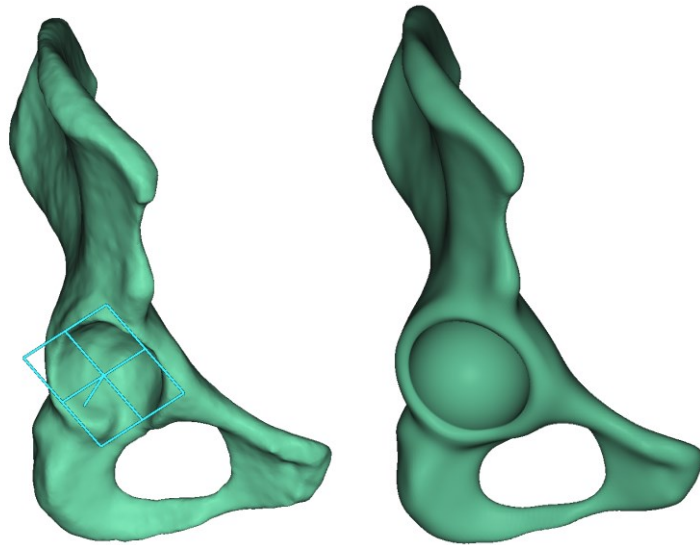
Figure 34 a) Pelvis with acetabular plane. b) Pelvis with acetabular cup

The PAC is then cut with the resection planes, defining the "Implant Base Shape" (IBS) (Figure 35 a) which will drive the following operations, namely the creation of the lattice infill and the solid external skin to protect the soft tissues. Regarding the graded gyroid lattice, the boundary for the transition between the osseointegrative region is defined by and offset of the resection planes; the offset distance is controlled by the user who can type the desired value in the corresponding space in the User Interface. The solid shell is created by subtracting a negative offset, of the desired value, of PAC from IBS (Figure 35 b).
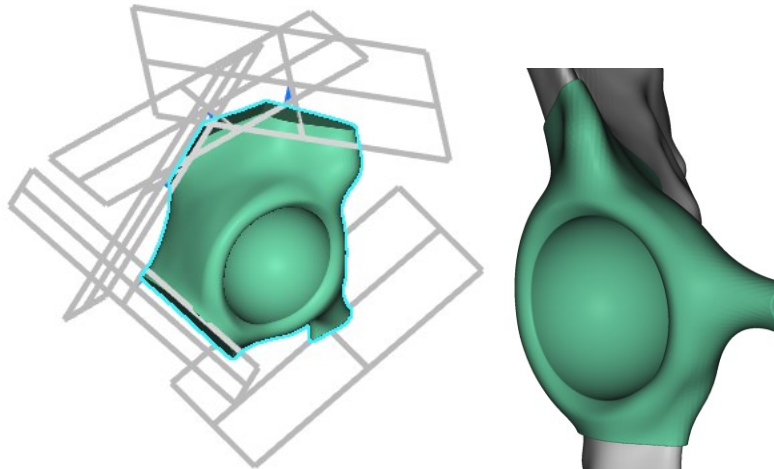
Figure 35 a) Implant Base Shape and resection planes. B) Solid shell creation

The next step is to create the flanges which will be merged with lattice infill and shell. The design of the flanges is demanded to a custom function with takes as input the screws' point, while the user defines height and thickness. First, the screw points are joined by a

segment, then it is thickened and eventually intersected with an offset of PAC of a value corresponding to the flange thickness. The intermediate results are presented in Figure 36.
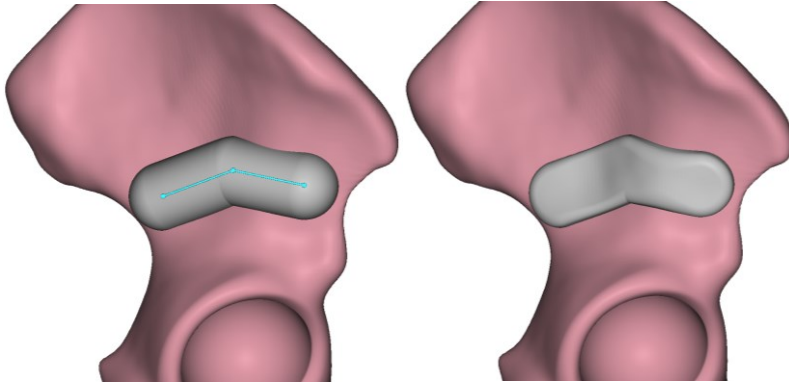
Figure 36 a) Thickening of the segment which joins the screws' points. b) Trimmed flanges with the desired thickness

Eventually, each part is merged through a Boolean union, and the result is the final implant's design with graded Gyroid lattice, flanges, and solid shell. Since the number and the dimensions of the screws' holes may vary within the same implant, in order to guarantee a high design flexibility, the generation of the holes is performed by a new custom function, which takes as input the screws' points and the screws' vectors which define the direction. The screws' variables are defined by the user, as highlighted in Figure 37, which are namely:

- Screw's head diameter
- Screw's stem diameter
- Distance between Screw's head and bone
- Hole clearance
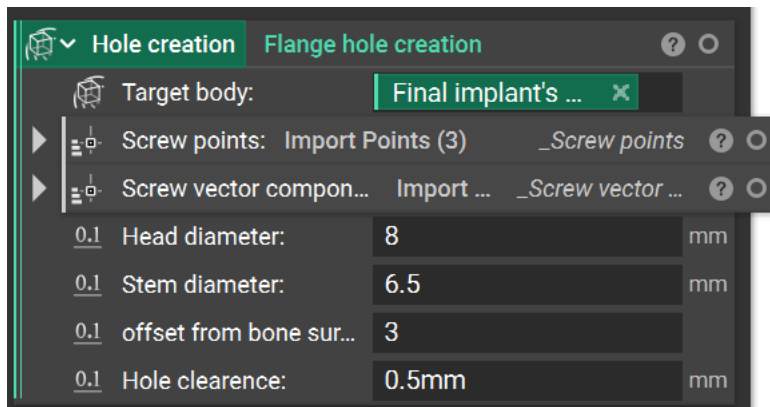
Figure 37 User's Interface of the hole creation function

3.4. Results

The robustness and flexibility of algorithms presented have been tested to reproduce 20 case-studies provided by Careggi Hospital regarding the pelvic region. Due to privacy issues, the original images of the actual implants can't be disclosed.

The automatic procedure managed to reproduce each of the cases analyzed effortlessly and proved to be very robust. Some examples are reported in Figure 38.
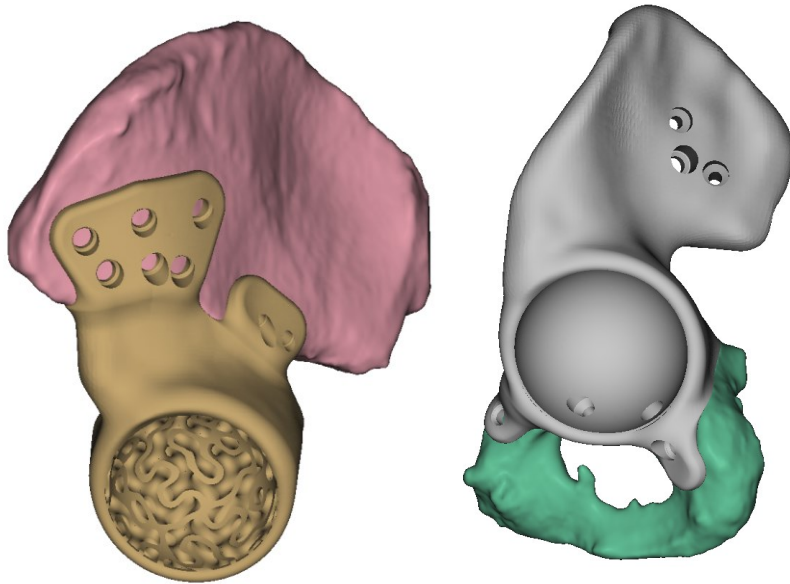
Figure 38 Examples of implants designed with the automatic nTopology procedure

The mean processing time for the 20 case-studies was 2±0.15 minutes on a laptop with GeForce RTX3070 graphic card, AMD Ryzen 9 5900HX processor and 32 Gb RAM. Such result is impressive if compared to the manual processing time which might take up to several hours, according to the complexity. The presented algorithms are non-sensitive to the design variables, and the processing time is only slightly affected by the quality of the original triangular mesh of the pelvis: the smoother it is, the faster becomes the process.

Both functions for hemipelvic and acetabular implants have been stressed by imposing a wide variability of the design parameters e.g., acetabular dimeter, screw's hole diameter, flange thickness and height. The implicit representation of bodies implemented in nTopology is extremely powerful in managing complex geometries as the gyroid lattice infill and is always able to create fillets between each part. Figure 39 shows an example where the hole's diameter has been changed from 5mm to 10mm and yet the software managed to adapt.
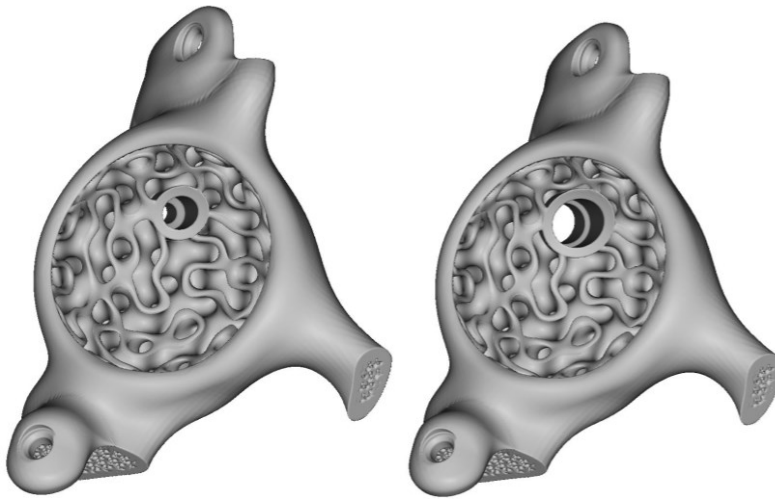
Figure 39 Screw hole

A further example is depicted in Figure 40, where the diameter of the acetabular cup has been set respectively to 50mm, 60mm and 70mm.
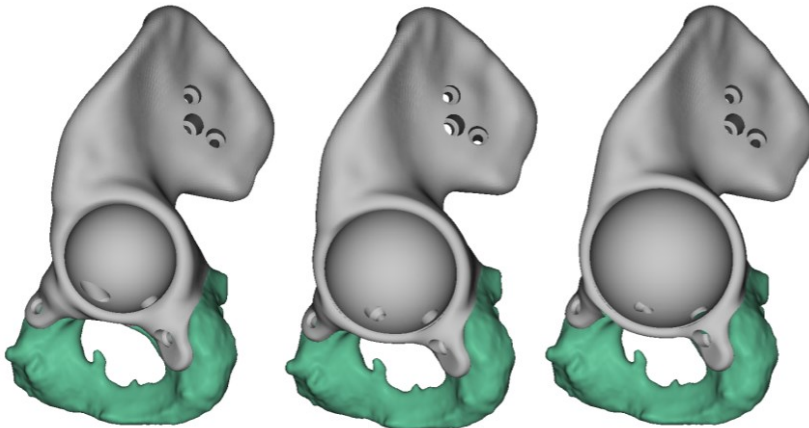
Figure 40 Acetabular cup diameter

The inputs required for the procedure have been manually designed in Geomagic Design X ®, which are:

- resection planes (.csv)
- screw point position (.csv)
- screw vectors, oriented as the screws (.csv)
- CAD surfaces to trim the undesired portions of the original bone (.stp)

and required an average time of 16±4.6 minutes, thus the overall process, from the definition of the inputs to the creation of a ready-to-print 3D model of pelvic implants through the developed algorithm is lower than 20 minutes. Besides the efficiency, the presented workflows also delivers significant advantages in terms of repeatability and product safety, as the human interaction is limited to the input of design variable values, while the CAD operations remain hidden. Furthermore, the user-friendly interface of nTopology enables to design high-performance custom implants with little or no CAD modelling experience, still ensuring a high degree of customization.

To date, the required inputs must be designed into an external software since nTopology, due to its implicit representation of bodies, doesn't allow to easily create CAD entities as surfaces, planes, and points, therefore the presented workflow must be used in conjunction with an external software. Ideally, the required inputs could be exported from a surgical planning software where the surgeons autonomously place resection planes, screws, thus empowering clinicians to have full control over the design and yet retaining the strict design principles enclosed within the automatic workflow.

3.4.1. Case study

A case-study for the acetabular implant is presented in Figure 41. The acetabular parameters have been calculated by the eSSM, while the resection planes and the position of the screws have been designed in Geomagic Design X under supervision of an orthopedic surgeon from Careggi Hospital.
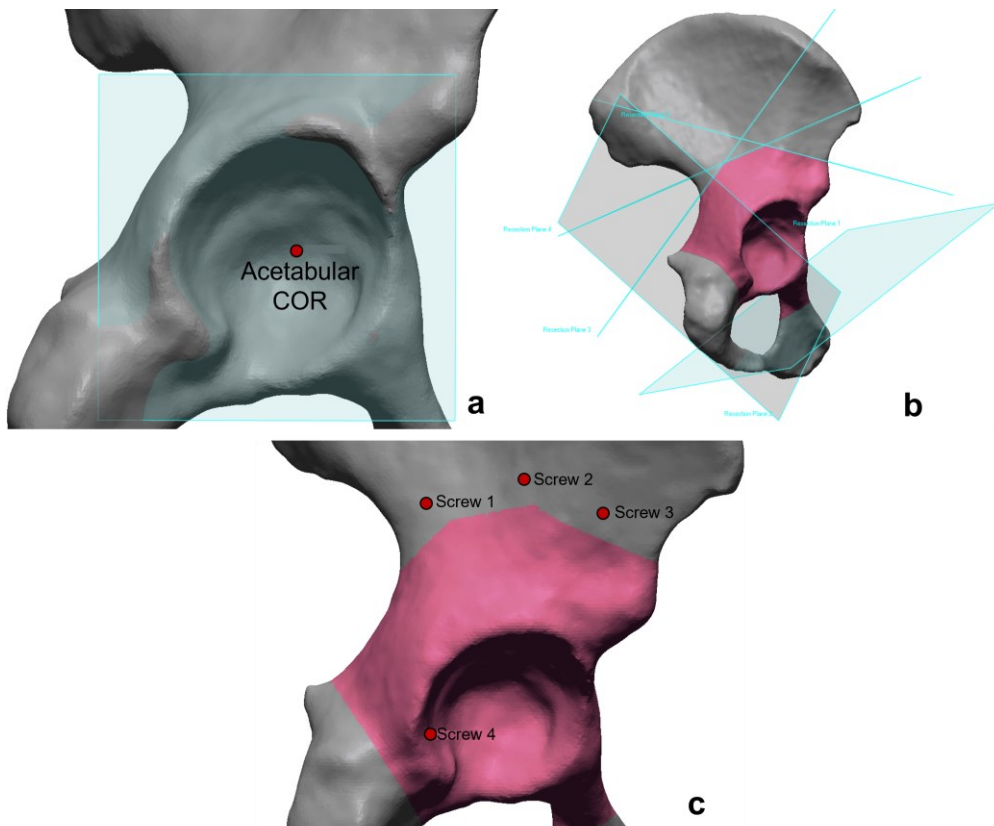
Figure 41 Inputs of the automatic workflow designed in Geomagic Design X. a) Acetabular plane and COR. b) Resection planes. c) Screw points

The CAD entities are exported in .csv format and imported in nTopology, where the same planes and points are retrieved, as highlighted in Figure 42.
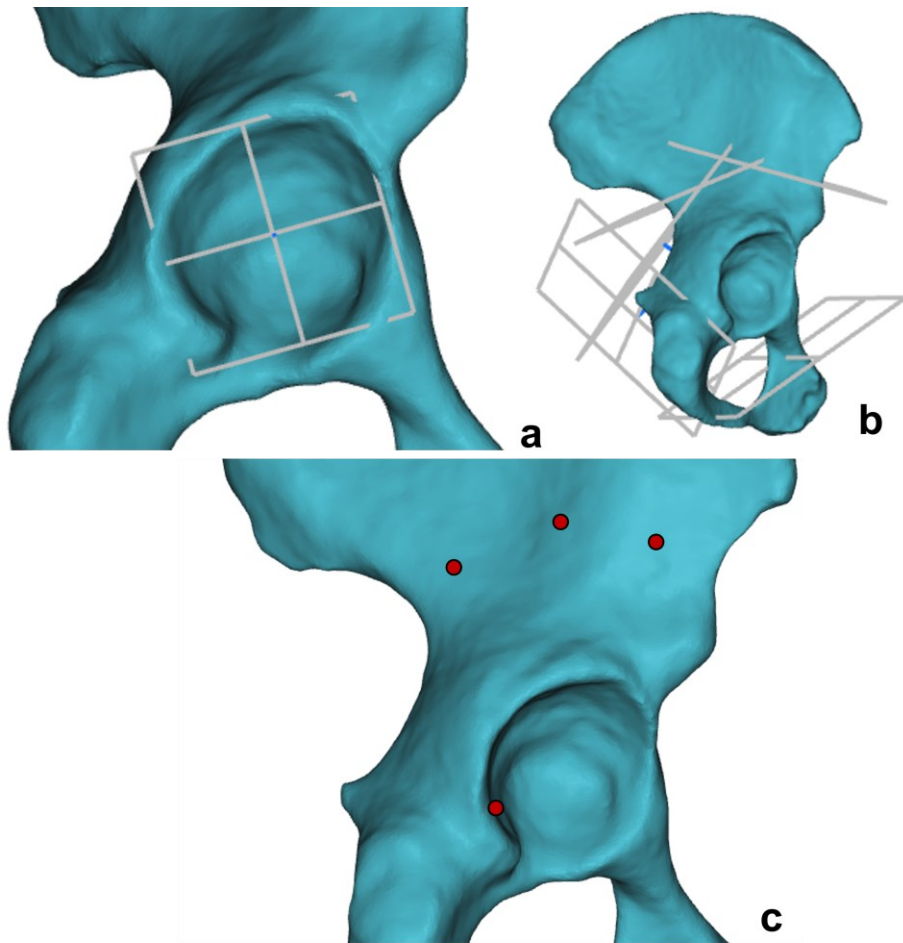
Figure 42 Planes and points imported in nTopology

Once the inputs have been imported, the process only requires to set the values for the design variables. Typical values are those reported in Figure 43.
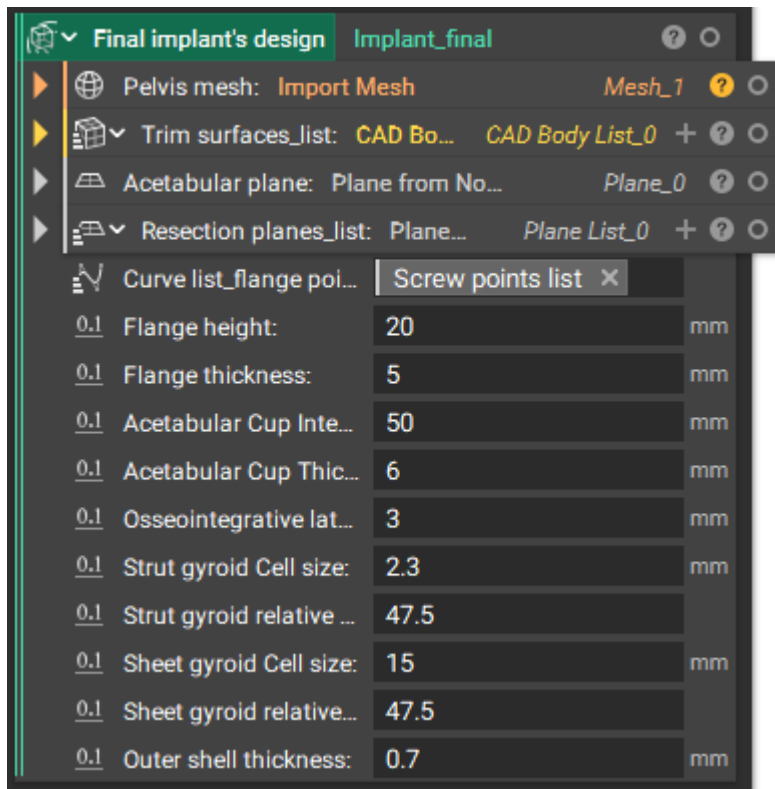
Figure 43 Custom function implemented in nTopology for acetabular implant design automation with typical values.

The set-up phase took 14 minutes. Once the user has set the desired values the automatic process starts and delivers a 3D model of an acetabular implant. The overall processing time for this case was 1.9 minutes. The result is depicted in Figure 44 a). The creation of the screws' holes is demanded to a separate custom function in order to allow for a high design flexibility: the function (Figure 44 d)) can be applied as many times as necessary according to the number and the geometric parameters of the screws. The final design is presented in Figure 44 b).
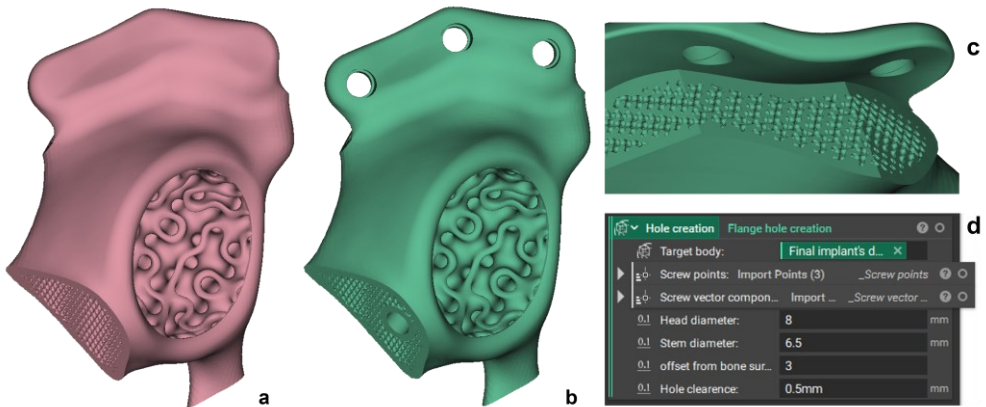
Figure 44 a) Output of the implemented custom function for acetabular implants. b) final design with screw holes. c) detail of the osseointegrative region. d) Function for hole creation.

Globally, the whole process lasted 18 minutes, which is dramatically faster than the manual process; for more, the presented workflow is capable to effectively design complex high-performance lattice structures with a fine control over the geometric and mechanical properties, which is a breakthrough compared to the state-of-the art concerning orthopedic implants, where lattice structures are limited to the bone-implant interface, while the rest is made of fully dense metal.

4. FE biomechanical model of the pelvis

A FE model of the pelvis was implemented to assess the behavior of a gyroid-based custom implant once implanted. First, a biomechanical model of a healthy pelvis was developed in order to be able to compare the results, in terms of stresses and deformations, with the most recent literature studies, then the implant of an acetabular implant was simulated to determine if the adopted approach for implant design delivers significant advantages for stress-shielding mitigation, compared to a traditional implant without an internal lattice structure.

4.1. FE model of the healthy pelvis

A FE biomechanical model of the pelvis was implemented; the goal was to validate the model in order to have a reliable framework to simulate the implantation of a prosthesis. For this purpose, a patient specific model of a 56 years of woman of 62 kg was implemented. First, CT scans have been segmented with Mimics 23.0 ® [119] to produce a polygonal mesh of the following bone structures:

- Sacrum
- Right and left pelvis
- Right and left femurs

Then, such models have been imported within the CAD software Geomagic Design X ® for further refinements. The polygonal meshes have been converted to .stp file with the Geomagic auto-surfacing tool, which automatically creates a 3D patch network on the entire mesh and generates a continuous NURBS surface by fitting control points in the network, then the articular cartilages have been designed, along with cortical and trabecular bone layers.

4.1.1. Hip cartilages

Cartilages of the hip joint act as cushions able to absorb shocks, preserving bone integrity, and facilitate joint rotation with a nearly-zero coefficient of friction [120]. For this work, two cartilage layers 1.5mm thick have been designed for a good realism; the hip joint has been approximated to a ball joint, consistently with the state of the art of FE pelvic models [121]–[124]. Figure 45 shows how femur and acetabulum have been manipulated to create regular spherical surfaces.
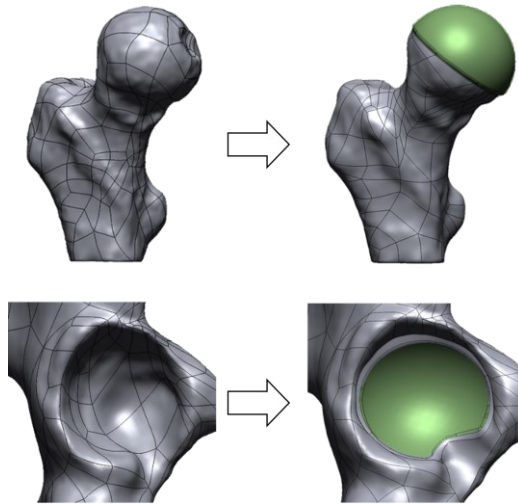
Figure 45 Design of articular cartilages for femur and the acetabulum.

4.1.2. Sacro-iliac joint cartilages

The cartilages of the sacro-iliac joint are two thin layers of material that connect the sacrum to the right and left iliac bones. These elements can vary greatly between each individual. In this case, the cartilages have been designed to fill the voids between sacrum and the two pelvises. The result is presented in Figure 46.
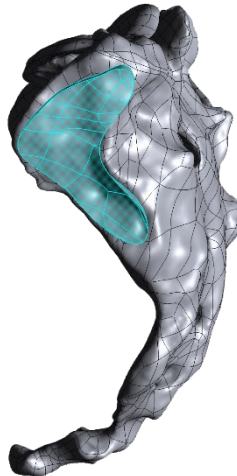
Figure 46 Lateral left view of sacrum bone and sacro-iliac cartilage

4.1.3. **Pubic symphysis cartilage**

The pubic symphysis is the cartilaginous joint that connects inferiorly the two halves of the pelvis. Its main functions are to stabilize the sacrum, help the bones of the pelvis support the internal organs, and to allow proper movement of the torso and lower limbs. Although the symphysis is composed of multiple layers of different material and properties, most literature studies simplify this component into a single body with material properties as the cortical bone [125]–[128]. The result is shown in Figure 47.

Figure 47 Pubic symphysis

4.1.4. **Cortical bone layer**

The bone structure can be divided into two structures with different physical properties:

- Cortical bone, which forms the strong and compact external cortex, with an average thickness of 2mm [129], [130]
- Trabecular bone, or spongious bone, which constitutes the elastic core of the bones with a hive-like structure

For this work each bone was modelled with a 2mm thick layer representing the cortical bone. An example is represented in Figure 48.

Figure 48 Femur with 2mm cortical layer (grey) and trabecular core (turquoise)

4.2. Pelvic implant modelling fixation

The pelvic implant was modelled with the support of the orthopedic surgeons of Careggi hospital, with the goal to reproduce the most common type of implant [131], [132]. The pelvic model was cut with four planes, as highlighted in Figure 49 a), then it was manipulated to create the acetabular cup (Figure 49 b))
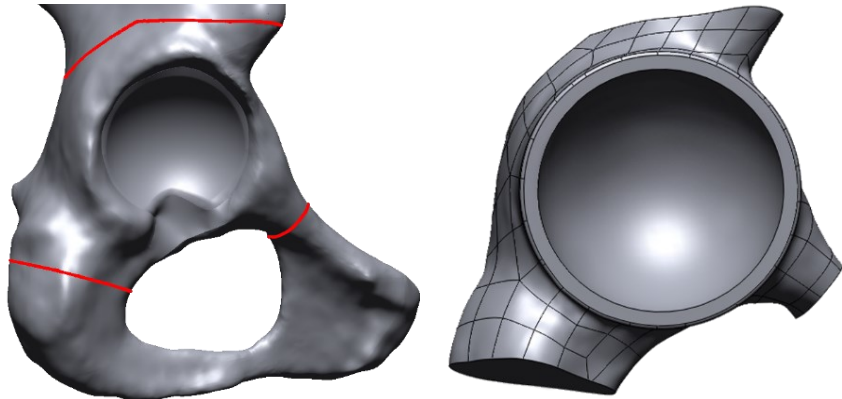
Figure 49 a) resection planes and b) implant with acetabular cup

4.3. Fastening elements design

Self-tapping screws made of titanium alloy T6Al4V1 were chosen, with variable length depending on the position in the model. The choice regarding screws' positioning was entrusted to surgeons and confirmed by recent studies [133].

The screws were schematically simplified as threadless cylinders [133], [134], and arranged as follows:

- one M5 screw at the pubis
- one M5 screw at the ischium
- two M6 screws at the ileum
- one 10mmØ stem

Figure 50 shows the described configuration.
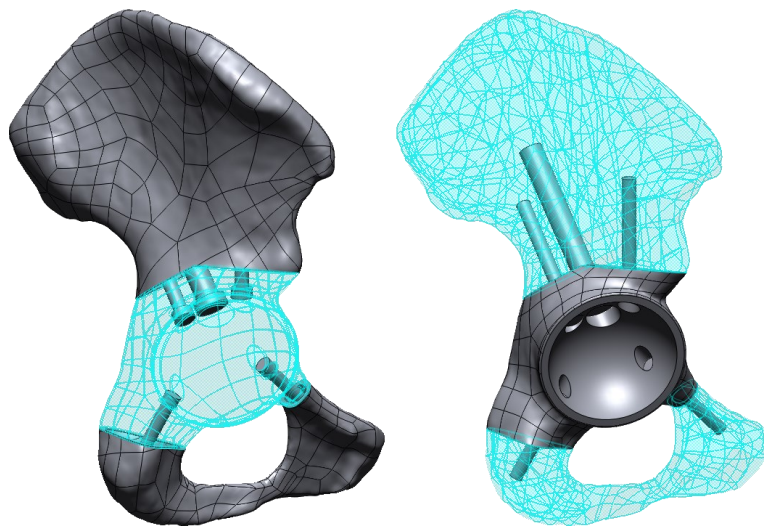
Figure 50 Screws and stem configuration within the implant

4.4. FEM implementation of the healthy pelvis

FE implementation was performed within Ansys ® 2019R3. First, a biomechanical model of a healthy pelvis was developed and compared with the state of the art; once validated the healthy model, the implantation of the prosthesis described in the previous section have been simulated to evaluate its effects over stress-shielding.

Stress-shielding is evaluated trough the Stress-shielding Signal (Equation 1); ideally, the strain energy in the healthy should remain unchanged before and after implant [135], [136].

Since the gyroid lattice structure is nearly isotropic, for this work it was approximated to a homogenous material with Young's modulus depending on the gyroid's relative density (eq Gibson); in such fashion, it is possible to evaluate the influence of the implant's stiffness over stress-shielding by tuning the implant's material properties within the simulation environment.

Due to the difficulty to directly compare simulation results with other studies, three models, with different loading conditions and constraints, have been implemented for a qualitative comparison with the most recent literature studies. For each model, stresses, deformations, and strain energy have been analyzed.

4.4.1. Material properties

The bone and cartilage material properties have been derived by [120], [137]. Three materials have been identified:

- Cortical bone, an isotropic material with Young's modulus E=17000 MPa and Poisson's coefficient ν=0.3

- Trabecular bone, isotropic material with Young's modulus E=1500 MPa and Poisson's coefficient ν=0.3
- Articular cartilage, isotropic material with Young's modulus E=15000 MPa and Poisson's coefficient ν=0.45

4.4.2. Contact modelling

The only movement allowed in the presented model is the rotation of the pelvis around the hip joint. Although several studies neglect the hip rotation [128], [138], in the following analyses the rotation was included proposing a more comprehensive evaluation. In the following, the types of contact used:

- FRICTIONLESS contact between femur and acetabular cartilages [130]. This approximation is consistent because the joints are constantly lubricated by the synovial fluid which cancels friction
- BONDED contact, which was applied to all the remaining contacts of the model, including the sacro-iliac joint because subject negligible micromovements [129].

4.4.3. Meshing

The bodies have been meshed with 2mm size quadratic tetrahedral elements. The meshes have been refined at each contact region by merging the elements' nodes and improve the result's reliability. The whole model consists of 1.519.976 nodes and 938.122 elements; in particular, the implant's core is composed of 796.630 nodes 582.016 elements, while the shell counts 17.2340 nodes and 102.210 elements.

4.4.4. Implementation of ligaments

Ligaments play a fundamental role in the stability of the human body, in fact, in case of traumas or too wide movements for the joints, they enter in tension with the purpose to preserve the correct integrity of joints, muscles and bones. For the model under consideration, the ligamentous groups were the sacro-iliac, ileo-femoral and pubic ligaments. These elements were schematized as tension-only springs, applied on two nodes, with assigned stiffness k. The springs' parameters have been derived by [130], [139], as presented in Equation 19:

$$k^L = k_{ISO}^L \frac{A^S}{A^L} \ (19)$$

Where:
k^L= stiffness assigned to individual ligament (spring element)
k_{ISO}^L= isometric stiffness assigned to the ligament group
A^S= total area associated with the node to which the spring is bound
A^L= total area associated with the ligament group

Table 2 shows the selected number of springs for each ligament with the relative stiffness.

Ligament	Stiffness $N.mm^2$	Number of springs
Sacroiliac	5000	45
Sacrospinous	1500	12
Sacrotuberous	1500	30
Iliolumbar	1000	10
Superior pubic	500	10
Arcuate pubic	500	15
Iliofemoral	1000	20

Table 2 Number of springs for each ligament and relative stiffness

Pelvic muscles have not been modelled because, for static analyses, have a negligible effect [139]–[141].

4.5. Loading conditions and constraints

Since there is no standard method to establish boundary conditions for FE analyses of the pelvis [142], two models have been developed to compare the results with most detailed FE studies of the pelvis [122]–[124], [143]–[147], and assess the reliability of the developed model for further simulations with the metal implant. The difference between the models consists in the boundary condition: in the first one, the lower faces of the femurs are constrained in all directions, while in the second one the constraints are directly in the acetabulum, since the femurs have been removed.

4.5.1. Model 1

The most comprehensive and accurate model is depicted in Figure 51, which includes cartilages, ligaments and femurs; it is loaded with a vertical force of 800N distributed over the first sacral vertebra, while the femurs' lower faces are fixed (Figure 51). This configuration reproduces very closely the natural loading condition of the pelvis in upright position.
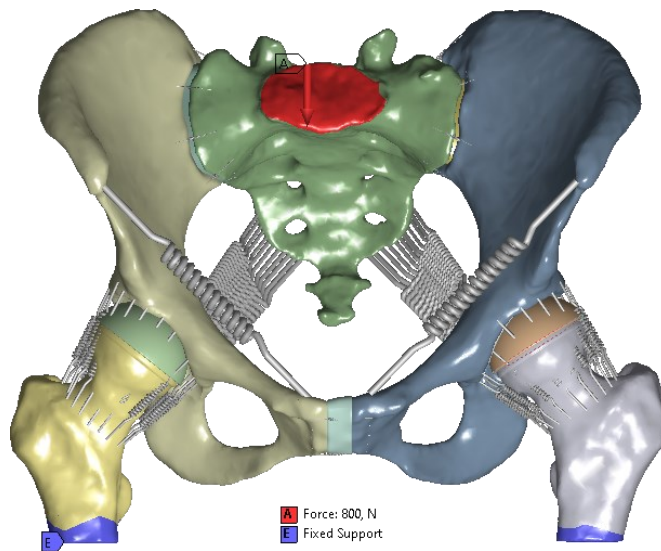
Figure 51 Model 1

4.5.2. **Model 2**

The second configuration, depicted in Figure 52, is the same as Model 1, though the femurs and the relative ligaments have been removed. Such set-up is very common in literature because of its simplicity, though the expected results shouldn't differ significantly from the previous case.
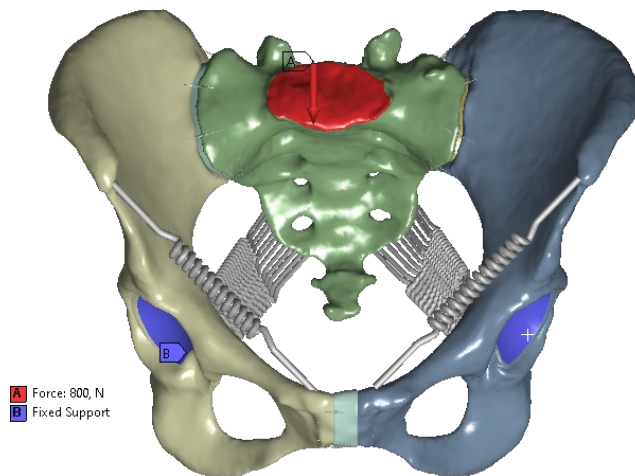
Figure 52 Model 2

4.6. Results

For the two models described above the Von Mises stress distribution have been evaluated. Since a direct numerical comparison of the results with reference studies is not feasible doe to geometric differences of the model, a qualitative analysis has been performed to assess if the developed model behaves consistently with the state of the art.

The results for both Model 1 and Model 2 are presented in Figure 53. The stress distribution across the entire pelvis exhibits the same behavior for both models, consistently with previous studies both qualitatively and in magnitude [142].
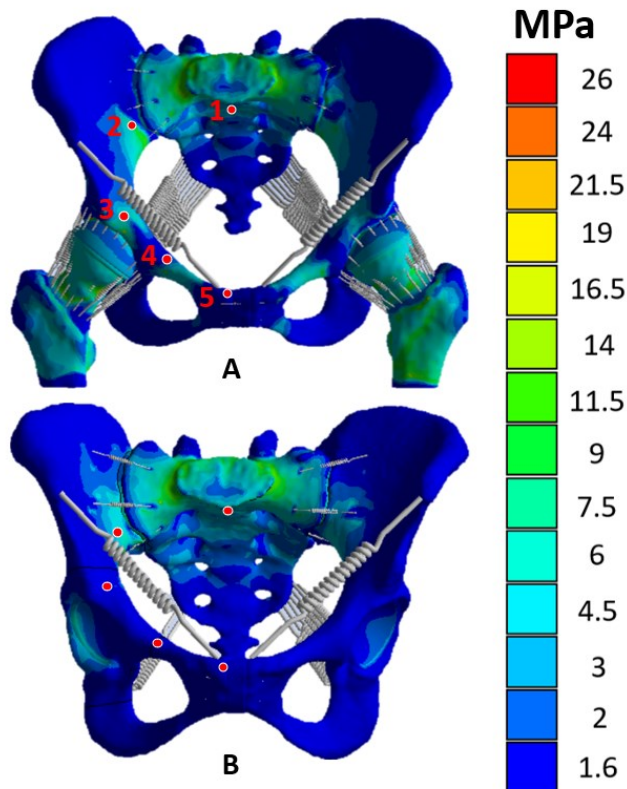
Figure 53 Von Mises stress distribution in Model 1 a) and Model 2 b). The values are expressed in MPa.

The stress is transmitted along the iliopectineal line in a very similar fashion for both models; the only difference lies in the fact that the pubis results nearly unloaded in Model 2 since the natural rotation around the femur heads, allowed in Model 1, is not permitted; such result is confirmed by the study of five relevant points in the iliopectineal line (Figure 53) on the right side of the pelvis. The corresponding points in each model have the same spatial coordinates and thus show the stress value of the corresponding nodes of the FE mesh. The stress values corresponding to the five points are presented in Table 3.

	Points				
	1	2	3	4	5
Model 1	3.8 MPa	4.5 MPa	0.43 MPa	0.55 MPa	0.003 MPa
Model 2	3.8 MPa	4.6 MPa	0.38 MPa	0.14 MPa	0.00034 MPa

Table 3 Stress values for Model and Model 2 at five relevant point on the ileopectineal line

The data confirm that the stress at Point 4 in Model 2 is lower compared to its counterpart in Model 1.

The models described behaved as expected consistently with the reference studies [121]–[124], [144], [145], [148]–[150], considering the stress distribution under the same loading condition, thus it is reasonable to exploit this framework for further analyses simulating the implant of a metal acetabular prosthesis.

4.7. FE analysis of the pelvis with metal implant

The goal of this analysis is to assess the effect of a gyroid-based lattice infill of a pelvic metal implant for stress-shielding mitigation. Since the gyroid structure has a nearly isotropic behavior, and its elastic modulus is a function of the structure's relative density [100], in this work the gyroid lattice have been approximated to a homogenous isotropic material. With the goal to simulate different densities, and thus mechanical properties, of the gyroid lattice, different material properties have been attributed to the prosthesis. First, a fully dense titanium implant was simulated, then its elastic modulus has been decreased until matching that of the cortical bone, in order to assess is the elastic matching approach is beneficial in reducing stress-shielding effects.

Besides displacements, deformations and stress, the most important parameter for the evaluation of stress-shielding effects is the Strain Energy Density (SED) [151]:

$$SED = \frac{1}{2}\sigma_{ij}\varepsilon_{ij} \left[\frac{J}{m^3}\right] (20)$$

Ideally, after implant the SED in the bone, particularly at the bone-implant interface, should be equal to the before-implant condition, which would mean that the bone is subject to the same mechanical stimuluses and thus is able to naturally renovate and avoid resorption due to stress-shielding. Such analysis was performed by measuring the SEDs at the bone-implant interfaces and comparing the corresponding values at the same location with the intact heathy model, as highlighted in green in Figure 54.
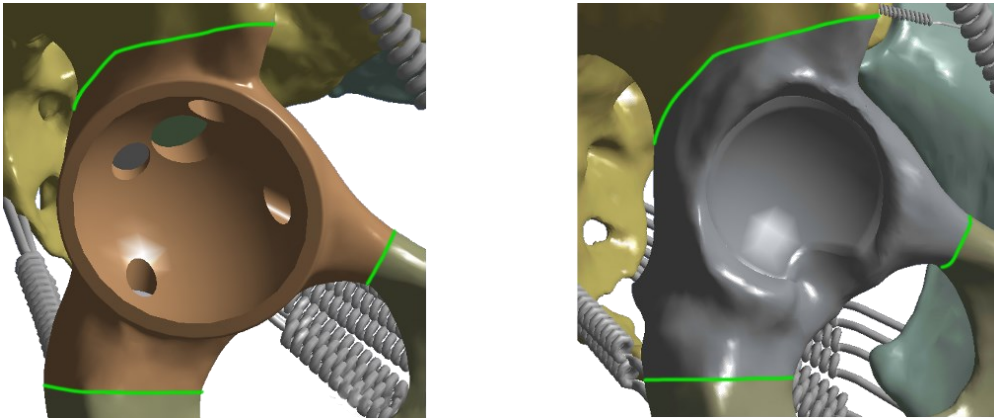
Figure 54 In green the corresponding areas for Strain Energy Density evaluation after and before implant

The implant was designed with a 0.7mm thick, fully dense superficial layer, and a core, which represents the lattice infill. A static analysis has been performed for each of the following material properties assigned to the implant's core, in order to determine the effects over stress-shielding of different gyroid's relative densities; the material properties assigned to the metal components are:

- Titanium alloy Ti6Al4V, Isotropic material with Young's modulus E=110 GPa, Poisson's coefficient ν=0,35.
- Isotropic material with Young's modulus E=50 GPa, Poisson's coefficient ν=0,35
- Isotropic material with Young's modulus E=17 GPa, Poisson's coefficient ν=0,35. This material matches the cortical bone's elastic modulus
- Isotropic material with Young's modulus E=1.5 GPa, Poisson's coefficient ν=0,35

4.8. Simulation set-up

Since the acetabular region corresponding to the implant have been removed, along with cartilages and ligaments, the configuration chosen to analyze the effects of the introduction of a pelvic metal implant was Model 2, to enable a direct comparison with the before-implant situation.

According to [152], three loading conditions have been simulated, namely upright position standing on both legs, single leg stance on left leg and single leg stance on right leg, as depicted in Figure 55.

In order to simulate different levels of osseointegration within the implant, the following contact types have been implemented:

- Frictionless: a non-realistic situation where there is no friction at the bone-implant interface and the implant's stability is entirely entrusted to the screws

- Frictional with μ=0.5 : simulates a condition with high friction after implant
- Bonded : ideal condition when the osseointegration is complete and there is no separation between bone and implant (at least after 12 months from implant)

The most interesting conditions to take into account is the Bonded contact between bone and implant: the first is the most severe case for the fixing screws which must maintain entirely the implant's stability; the latter, which simulates a perfect integration between bone and implant with no relative movement, allows to better evaluate the effects of the implant's internal lattice structure, and analyze the stress-shielding effects.

Regarding the screws, 200N preload was imposed according to [134], which states that the optimal preload for trabecular bone screws is between 200 N and 300 N; a higher value might compromise the bone's integrity, while a lower preload does not guarantee enough contact pressure between bone and implant, allowing relative micro-movements with negative effects over osseointegration. In each case analyzed, including the Frictionless set up, which is the most onerous for the screws, with 200 N preload the stresses in the screws had an average value of 40 MPa and a maximum value of 205 MPa, which is widely in safety conditions for the titanium components (critical stress = 1.065 GPa); regarding the bones, the maximum stress values in both trabecular and cortical bone exceed the critical values (10 MPa for the trabecular bone and 160 MPa for the cortical bone), though peak values occur in local hot-spots and should not compromise bone's integrity. Such results are coherent with [134], [153].
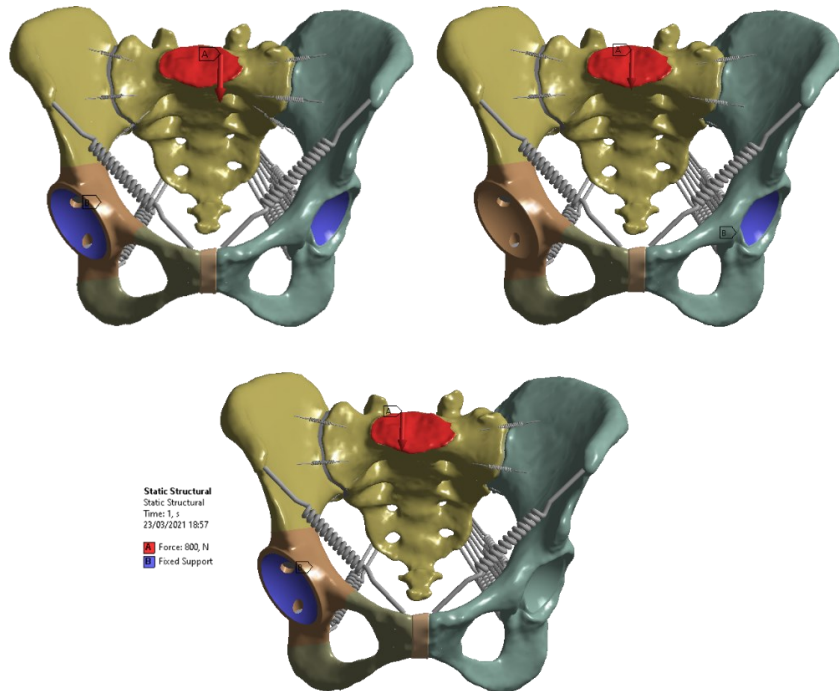
Figure 55 Simulation set-up of the pelvis with implant: a) constrained acetabulum and implant, b) constrained acetabulum, c) constrained implant

4.8.1. **Results**

Stresses and SED of the pelvis with implant have been evaluated and compared with the results of Model 2, with the goal to assess if the elastic matching approach is beneficial in reducing stress shielding effects in the healthy bone stock, and thus promote a long duration over time of the pelvic implant.

In this section the results of a double leg-stance will be presented, as the other configurations did not provide any additional relevant information.

Figure 56 shows the stress distribution of the whole pelvis for the four materials assigned to the implant's core, compared with the results of Model 2 (Figure 53 b)).
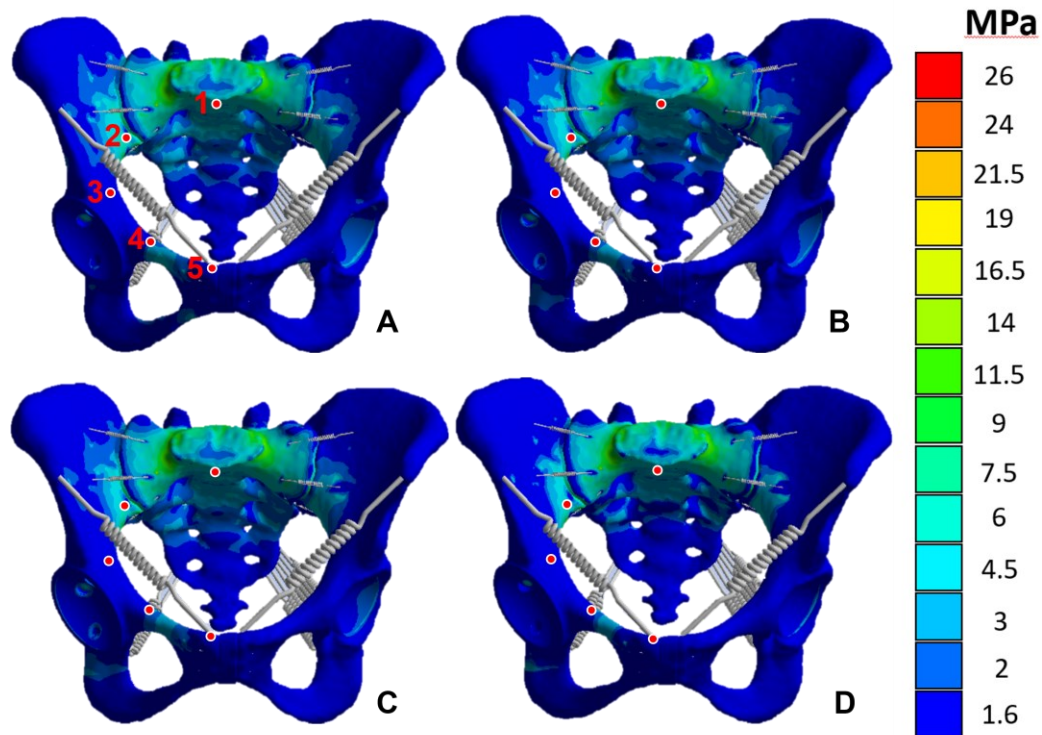
Figure 56 Stress distribution in the pelvis with different Young's modulus of the implant's core: a) 110GPa, b) 50 GPa, c) 17 GPa, d) 1.5 GPa

The insertion of the prosthesis does not involve significant changes in stress distribution. The stress values at five significant points on the iliopectineal line are reported in Figure 57.
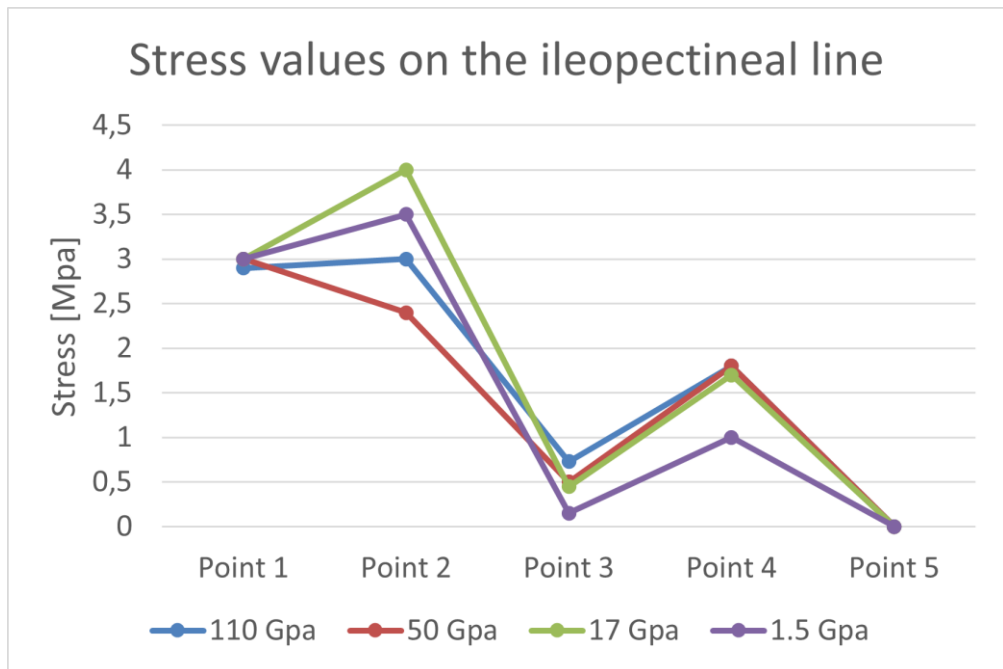
Figure 57 Stress values on the ileopectineal line for different implant's core mechanical properties

The largest difference between Model 2 and the four cases presented with the implant can be noticed in the pubic ramus, in the surrounding of Point 4, which is caused by the introduction of the fixation screw; in fact, the stress values in that area remain nearly constant regardless of the variation of the implant's material properties.

Concerning the SED, larger differences can be appreciated among the case presented. By decreasing the elastic modulus of the implant's core from 110 GPa to 1.5 GPa, thus from dense titanium to a lattice structure with the same properties as the trabecular bone, as the stiffness decreases the total SED in the healthy bone increases, meaning that the mechanical stimuluses necessary to promote bone renovation increase as well. In Table 4 are presented the SED values in the ileum at the bone-implant interface; in Ansys Mechanical, the SED is calculated for each element of the mesh, thus the Total corresponds to the sum of the SED of each mesh element in the area of interest.

Implant core material	Minimum [J]	Maximum [J]	Total [J]
110 GPa	$9.86 \ 10^{-12}$	$8.62 \ 10^{-7}$	$1.34 \ 10^{-4}$
50 GPa	$9.45 \ 10^{-12}$	$8.27 \ 10^{-7}$	$1.36 \ 10^{-4}$
17 GPa	$8.32 \ 10^{-12}$	$7.22 \ 10^{-7}$	$1.42 \ 10^{-4}$
1.5 GPa	$6.76 \ 10^{-12}$	$3.83 \ 10^{-7}$	$1.93 \ 10^{-4}$

Table 4 SED in the ileum at the bone-implant interface for the four tested material

Such result can be noticed at each bone-implant interface examined, which confirms the positive effect of the elastic matching approach for orthopedic implants to reduce stress-shielding effects. In a real-case-scenario, among the tested materials for the implant's core, the

ideal value is that of the cortical bone as the corresponding gyroid lattice structure, with $\rho_{rel} =$ 47.5, restores the same stress distribution in the pelvis as well as the SED as the before-implant case; besides stress and SED restoration, such structure also guarantees excellent mechanical properties and promotes osseointegration.

The SED for the four materials at the bone-implant interface at the ileum are presented in Figure 58. To be noted that Ansys Mechanical expresses the SED in Joule, so the results should be normalized with the average mesh element's volume for a direct comparison with other literature studies.
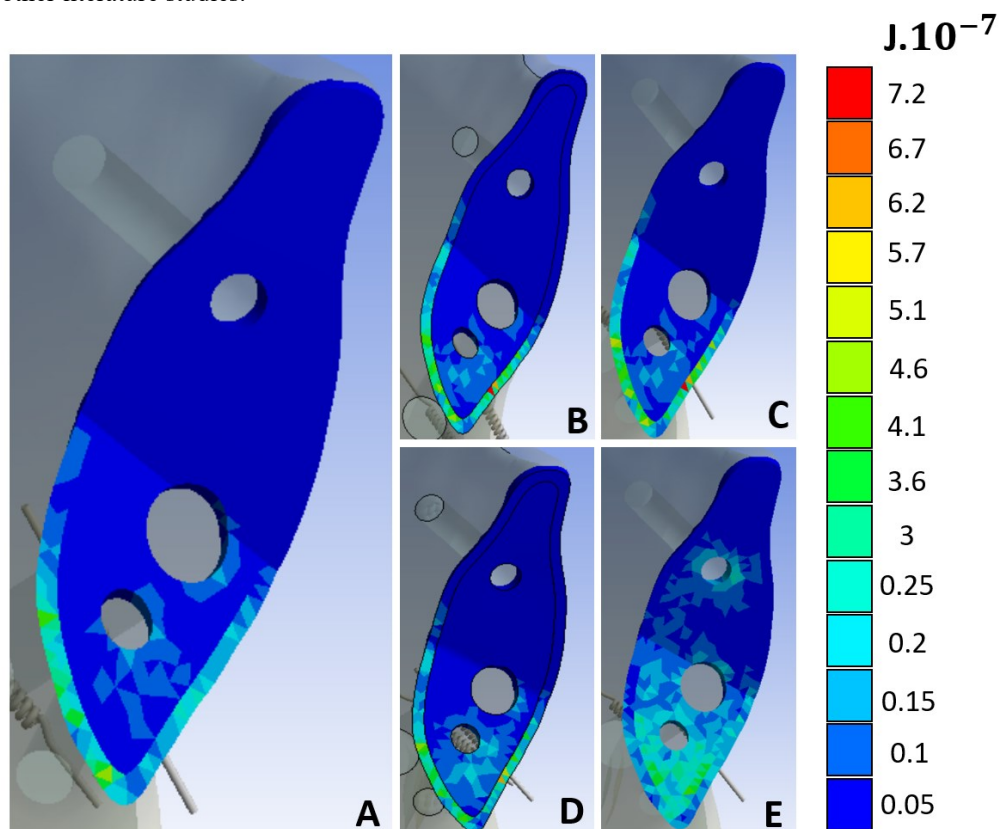
Figure 58 SED in the ischium at the bone-implant interface. a) healthy bone. b) implant with 110 GPa. c) implant with 50 GPa. d) implant with 17 GPa. e) implant with 1.5 GPa

As highlighted by the picture, by decreasing the elastic modulus of the implant's core, which corresponds to decrease the relative density of the Gyroid lattice, the SED in the bone increases, which means that the mechanical stimulus increases accordingly, which has a positive effect to promote bone growth (Figure 2). Among the tested materials for the implant's lattice structure, the one that best restores the pattern of SED is the one with the same Young's modulus of the bone (Figure 58 d)), which confirms the effectiveness of the elastic matching approach to mitigate stress shielding effects [16], [136].

5. Conclusions and final remarks

The activity presented in this Ph.D. thesis deals with the design automation of high-performance customized orthopedic implants for load bearing applications. In particular, this work aimed to analyze the design process of personalized devices and eventually automate the repetitive operations in order to implement an efficient and robust workflow able to deliver, in a brief time span, a ready-to-manufacture 3D model with a gyroid-based lattice infill.

First, a novel approach to tackle the stress shielding occurrence has been investigated: by matching the elastic modulus of the metal implant with that of the bone, it is possible to limit bone remodeling effects induced by the altered load transmission and thus ensure a longer duration of the implant; such result can be achieved by implementing a lattice infill, with the goal to reduce the implant's stiffness, while maintaining a good mechanical resistance. Although several studies investigated the effectiveness of the Gyroid lattice for orthopedic applications, to date it hasn't been employed yet to real-case scenarios. The novelty introduced in this thesis work is the implementation of a graded gyroid lattice structure for orthopedic implants within a framework for the design of custom devices. Compared to other lattice structures, the Gyroid has better mechanical properties and its unique geometry is able to promote osseointegration; for more, thanks to its simple mathematical formulation, it is possible to locally tune the mechanical and geometric features to comply with the biomechanical requirements for implantable devices.

A relevant contribution of the present work is the improvement of the classical formulation of SSM: with the goal to implement an automatic workflow for the design of custom implants for severe bone defects and bone tumors, an enhanced version of the SSM has been presented able to enclose, besides information regarding the mere geometry of the pelvis, in this application, other relevant parameters as the acetabular center of rotation and orientation. Such tool can automatically reconstruct highly defective geometries and also provide the coordinates of the CORs as well as the acetabular orientation, overcoming the current manual method based on the study of plane radiographies by expert users.

A semi-automatic procedure for the design of pelvic custom implants has been implemented in nTopology, a CAD software based on implicit modelling which provides a very handy environment to create custom reusable workflows. For this work, two algorithms with slight differences have been developed to cover the most common types of pelvic implants; such algorithms have been tested over 20 case studies with a wide variability in terms of geometry and design constraints and always succeeded to deliver the expected results. The great advantage of this method is the processing time, which resulted in 2±0.15 minutes, compared to a manual process, which might take up to several hours. Design automation also improves the product's safety by reducing the human interaction and allows non expert CAD users to perform the task. Due to the high design flexibility allowed by the implemented algorithms, it is possible to easily adapt the procedure to design implants in different anatomical regions with little effort.

To date metal implants are manufactured with fully dense material, with a lattice structure only at the bone-implant interface for osseointegration; the novelty of this work is to implement a gyroid based resistant and easily manufacturable lattice structure within the whole

implant, with a great advantage in terms of weight reduction, stress shielding mitigation, cost and manufacturing time reduction. A sample custom implant, presented in Figure 59, has been manufactured via Selective Laser Melting AM technology in pure titanium to assess the manufacturability of the gyroid lattice; from a visual inspection the component is compliant with the 3D model, though further analyses are necessary to determine the actual geometric accuracy.

Figure 59 3D printed custom implant with Gyroid lattice structure

Finally, a patient specific FE biomechanical model of the pelvis has been implemented in Ansys Mechanical to validate the design strategy and assess the effects induced by the implementation of a Gyroid based lattice infill. The results suggest that, by matching the elastic modulus of the implant with that of the bone, the stress shielding effects are mitigated. Such promising result should be further investigated by analyzing the stress distribution and the SED in the whole pelvis and not just at the bone-implant interfaces; moreover, a more comprehensive analysis which includes the femurs could provide additional information.

The implemented automatic workflow for the design of custom implants triggered the development of a web-based platform for surgical planning at the Department of Industrial Engineering of the University of Florence, with the goal to provide a user-friendly environment for surgeons where they can easily point out every design constraint, as planes, screws and so on, which will be exported and then automatically imported within nTopology, thus completing the automatic procedure. The integration of these two tools would represent a

breakthrough in the field of orthopedic surgery because it would enable surgeons to autonomously plan and design custom devices, yet ensuring a high quality and safety standard, since the design operation are hidden to the user which can only type certain design variables. The design automation would then cut the design costs and make such devices more and more accessible.

Concerning the eSSM, an interesting improvement would be the implementation of a deformable template for FE patient specific analyses, which would dramatically cut the implementation time and allow to study in depth the interaction between bone and implant, which to date is not feasible in most real cases due to time issues.

Acknowledgements

Bibliography

[1]   A. Vaish and R. Vaish, "3D printing and its applications in Orthopedics," *Journal of Clinical Orthopaedics and Trauma*, vol. 9, Mar. 2018, doi: 10.1016/j.jcot.2018.02.003.

[2]   D. Pacione, O. Tanweer, P. Berman, and D. H. Harter, "The utility of a multimaterial 3D printed model for surgical planning of complex deformity of the skull base and craniovertebral junction," *Journal of Neurosurgery*, vol. 125, no. 5, Nov. 2016, doi: 10.3171/2015.12.JNS151936.

[3]   K. C. Wong, K. Y. Sze, I. O. L. Wong, C. M. Wong, and S. M. Kumta, "Patient-specific instrument can achieve same accuracy with less resection time than navigation assistance in periacetabular pelvic tumor surgery: a cadaveric study," *International Journal of Computer Assisted Radiology and Surgery*, vol. 11, no. 2, pp. 307–316, 2016, doi: 10.1007/s11548-015-1250-x.

[4]   T. M. Wong *et al.*, "The use of three-dimensional printing technology in orthopaedic surgery," *Journal of Orthopaedic Surgery*, vol. 25, no. 1, Jan. 2017, doi: 10.1177/2309499016684077.

[5]   A. L. Jardini *et al.*, "Cranial reconstruction: 3D biomodel and custom-built implant created using additive manufacturing," *Journal of Cranio-Maxillofacial Surgery*, vol. 42, no. 8, Dec. 2014, doi: 10.1016/j.jcms.2014.07.006.

[6]   Mohd. Javaid and A. Haleem, "Additive manufacturing applications in orthopaedics: A review," *Journal of Clinical Orthopaedics and Trauma*, vol. 9, no. 3, Jul. 2018, doi: 10.1016/j.jcot.2018.04.008.

[7]   Mohd. Javaid and A. Haleem, "Current status and challenges of Additive manufacturing in orthopaedics: An overview," *Journal of Clinical Orthopaedics and Trauma*, vol. 10, no. 2, Mar. 2019, doi: 10.1016/j.jcot.2018.05.008.

[8]   F. Buonamici, L. Guariento, and Y. Volpe, "3D Digital Surgical Planning: An Investigation of Low-Cost Software Tools for Concurrent Design," pp. 765–775, 2020, doi: 10.1007/978-3-030-31154-4_65.

[9]   N. Kumar and B. Gupta, "Global incidence of primary malignant bone tumors," *Current Orthopaedic Practice*, vol. 27, no. 5, pp. 530–534, 2016, doi: 10.1097/BCO.0000000000000405.

[10]   T. Ozaki *et al.*, "Osteosarcoma of the pelvis: Experience of the Cooperative Osteosarcoma Study Group," *Journal of Clinical Oncology*, vol. 21, no. 2, pp. 334–341, 2003, doi: 10.1200/JCO.2003.01.142.

[11]   N. G. Burke, J. P. Gibbons, A. J. Cassar-Gheiti, F. M. Walsh, and J. P. Cashman, "Total hip replacement—the cause of failure in patients under 50 years old?," *Irish*

Journal of Medical Science (1971 -), vol. 188, no. 3, Aug. 2019, doi: 10.1007/s11845-018-01956-8.

[12]   M. Baauw, G. G. van Hellemondt, M. L. van Hooff, and M. Spruit, "The accuracy of positioning of a custom-made implant within a large acetabular defect at revision arthroplasty of the hip," *Bone and Joint Journal*, vol. 97-B, no. 6, pp. 780–785, 2015, doi: 10.1302/0301-620X.97B6.35129.

[13]   S. Arabnejad, B. Johnston, M. Tanzer, and D. Pasini, "Fully porous 3D printed titanium femoral stem to reduce stress-shielding following total hip arthroplasty," *Journal of Orthopaedic Research*, vol. 35, no. 8, Aug. 2017, doi: 10.1002/jor.23445.

[14]   T. W. Bauer and J. Schils, "The pathology of total joint arthroplasty," *Skeletal Radiology*, vol. 28, no. 9, Sep. 1999, doi: 10.1007/s002560050552.

[15]   M. B. Bezuidenhout, D. M. Dimitrov, A. D. van Staden, G. A. Oosthuizen, and L. M. T. Dicks, "Titanium-Based Hip Stems with Drug Delivery Functionality through Additive Manufacturing," *BioMed Research International*, vol. 2015, 2015, doi: 10.1155/2015/134093.

[16]   K. Haase and G. Rouhi, "Prediction of stress shielding around an orthopedic screw: Using stress and strain energy density as mechanical stimuli," *Computers in Biology and Medicine*, vol. 43, no. 11, Nov. 2013, doi: 10.1016/j.compbiomed.2013.07.032.

[17]   G. J. della Rocca, K. S. Leung, and H.-C. Pape, "Periprosthetic Fractures: Epidemiology and Future Projections," *Journal of Orthopaedic Trauma*, vol. 25, no. Supplement 2, Jun. 2011, doi: 10.1097/BOT.0b013e31821b8c28.

[18]   D. N. Kugelman, V. H. Frankel, A. Baker, and K. Egol, "A Recurrent Stress Fracture of the Humerus following Fixation: The Effect of Implant Stress Shielding.," *Journal of orthopaedic case reports*, vol. 9, no. 2, 2019, doi: 10.13107/jocr.2250-0685.1342.

[19]   M. I. Z. Ridzwan, S. Shuib, A. Y. Hassan, A. A. Shokri, and M. N. Mohamad Ib, "Problem of Stress Shielding and Improvement to the Hip Implant Designs: A Review," *Journal of Medical Sciences*, vol. 7, no. 3, Mar. 2007, doi: 10.3923/jms.2007.460.467.

[20]   J. Wolff, *The Law of Bone Remodelling*. Berlin, Heidelberg: Springer Berlin Heidelberg, 1986. doi: 10.1007/978-3-642-71031-5.

[21]   H. M. Frost, "From Wolff's law to the mechanostat: A new 'face' of physiology," *Journal of Orthopaedic Science*, vol. 3, no. 5, pp. 282–286, 1998, doi: 10.1007/s007760050054.

[22]   H. M. Frost, "Bone's Mechanostat: A 2003 Update," *Anatomical Record - Part A Discoveries in Molecular, Cellular, and Evolutionary Biology*, vol. 275, no. 2, pp. 1081–1101, 2003, doi: 10.1002/ar.a.10119.

[23]   S. Sturm, S. Zhou, Y. W. Mai, and Q. Li, "On stiffness of scaffolds for bone tissue engineering-a numerical study," *Journal of Biomechanics*, vol. 43, no. 9, pp. 1738–1744, 2010, doi: 10.1016/j.jbiomech.2010.02.020.

[24]   D. Mahmoud and M. Elbestawi, "Lattice Structures and Functionally Graded Materials Applications in Additive Manufacturing of Orthopedic Implants: A Review," *Journal of Manufacturing and Materials Processing*, vol. 1, no. 2, p. 13, 2017, doi: 10.3390/jmmp1020013.

[25]   C. Han *et al.*, "Continuous functionally graded porous titanium scaffolds manufactured by selective laser melting for bone implants," *Journal of the Mechanical Behavior of Biomedical Materials*, vol. 80, no. January, pp. 119–127, 2018, doi: 10.1016/j.jmbbm.2018.01.013.

[26]   H. A. Zaharin *et al.*, "Effect of unit cell type and pore size on porosity and mechanical behavior of additively manufactured Ti6Al4V scaffolds," *Materials*, vol. 11, no. 12, 2018, doi: 10.3390/ma11122402.

[27]   L. Yang, R. Mertens, M. Ferrucci, C. Yan, Y. Shi, and S. Yang, "Continuous graded Gyroid cellular structures fabricated by selective laser melting: Design, manufacturing and mechanical properties," *Materials and Design*, vol. 162, pp. 394–404, 2019, doi: 10.1016/j.matdes.2018.12.007.

[28]   A. Yánez, A. Herrera, O. Martel, D. Monopoli, and H. Afonso, "Compressive behaviour of gyroid lattice structures for human cancellous bone implant applications," *Materials Science and Engineering C*, vol. 68, no. May 2019, pp. 445–448, 2016, doi: 10.1016/j.msec.2016.06.016.

[29]   C. Yan, L. Hao, A. Hussein, and P. Young, "Ti-6Al-4V triply periodic minimal surface structures for bone implants fabricated via selective laser melting," *Journal of the Mechanical Behavior of Biomedical Materials*, vol. 51, pp. 61–73, 2015, doi: 10.1016/j.jmbbm.2015.06.024.

[30]   L. Dall'Ava, H. Hothi, J. Henckel, A. di Laura, P. Shearing, and A. Hart, "Comparative analysis of current 3D printed acetabular titanium implants," *3D Printing in Medicine*, vol. 5, no. 1, Dec. 2019, doi: 10.1186/s41205-019-0052-0.

[31]   N. Taniguchi *et al.*, "Effect of pore size on bone ingrowth into porous titanium implants fabricated by additive manufacturing: An in vivo experiment," *Materials Science and Engineering: C*, vol. 59, Feb. 2016, doi: 10.1016/j.msec.2015.10.069.

[32]   R. Xia, Z. Zhai, Y. Chang, and H. Li, "Clinical Applications of 3-Dimensional Printing Technology in Hip Joint," *Orthopaedic Surgery*, vol. 11, no. 4, Aug. 2019, doi: 10.1111/os.12468.

[33]   X. Y. Zhang, G. Fang, S. Leeflang, A. A. Zadpoor, and J. Zhou, "Topological design, permeability and mechanical behavior of additively manufactured functionally graded porous metallic biomaterials," *Acta Biomaterialia*, vol. 84, pp. 437–452, 2019, doi: 10.1016/j.actbio.2018.12.013.

[34]   Y. E. Delikanli and M. C. Kayacan, "Design, manufacture, and fatigue analysis of lightweight hip implants," *Journal of Applied Biomaterials & Functional Materials*, vol. 17, no. 2, Apr. 2019, doi: 10.1177/2280800019836830.

[35]   D. J. Yoo, "Advanced porous scaffold design using multi-void triply periodic minimal surface models with high surface area to volume ratios," *International Journal of Precision Engineering and Manufacturing*, vol. 15, no. 8, pp. 1657–1666, 2014, doi: 10.1007/s12541-014-0516-5.

[36]   A. du Plessis *et al.*, "Beautiful and Functional: A Review of Biomimetic Design in Additive Manufacturing," *Additive Manufacturing*, vol. 27. Elsevier B.V., pp. 408–427, May 01, 2019. doi: 10.1016/j.addma.2019.03.033.

[37]   Z. Hua, Y. Fan, Q. Cao, and X. Wu, "Biomechanical study on the novel biomimetic hemi pelvis prosthesis," *Journal of Bionic Engineering*, vol. 10, no. 4, pp. 506–513, 2013, doi: 10.1016/S1672-6529(13)60244-9.

[38]   S. Vijayavenkataraman, L. Zhang, S. Zhang, J. Y. Hsi Fuh, and W. F. Lu, "Triply Periodic Minimal Surfaces Sheet Scaffolds for Tissue Engineering Applications: An Optimization Approach toward Biomimetic Scaffold Design," *ACS Applied Bio Materials*, vol. 1, no. 2, Aug. 2018, doi: 10.1021/acsabm.8b00052.

[39]   B. Zhang *et al.*, "The biomimetic design and 3D printing of customized mechanical properties porous Ti6Al4V scaffold for load-bearing bone reconstruction," *Materials and Design*, vol. 152, pp. 30–39, 2018, doi: 10.1016/j.matdes.2018.04.065.

[40]   N. Kladovasilakis, K. Tsongas, and D. Tzetzis, "Finite element analysis of orthopedic hip implant with functionally graded bioinspired lattice structures," *Biomimetics*, vol. 5, no. 3, 2020, doi: 10.3390/BIOMIMETICS5030044.

[41]   S. Parithimarkalaignan and T. v. Padmanabhan, "Osseointegration: An Update," *The Journal of Indian Prosthodontic Society*, vol. 13, no. 1, Mar. 2013, doi: 10.1007/s13191-013-0252-z.

[42]   S. Arabnejad Khanoki and D. Pasini, "The Fatigue Design of a Bone Preserving Hip Implant With Functionally Graded Cellular Material," *Journal of Medical Devices*, vol. 7, no. 2, Jun. 2013, doi: 10.1115/1.4024310.

[43]   M. A. K. Liebschner, "Biomechanical considerations of animal models used in tissue engineering of bone," *Biomaterials*, vol. 25, no. 9, Apr. 2004, doi: 10.1016/S0142-9612(03)00515-5.

[44]   L. G. Cima, J. P. Vacanti, C. Vacanti, D. Ingber, D. Mooney, and R. Langer, "Tissue Engineering by Cell Transplantation Using Degradable Polymer Substrates," *Journal of Biomechanical Engineering*, vol. 113, no. 2, May 1991, doi: 10.1115/1.2891228.

[45]   V. KARAGEORGIOU and D. KAPLAN, "Porosity of 3D biomaterial scaffolds and osteogenesis," *Biomaterials*, vol. 26, no. 27, Sep. 2005, doi: 10.1016/j.biomaterials.2005.02.002.

[46]   J. M. Huyghe, R. van Loon, F. T. R. Baaijens, P. M. van Kemenade, and T. H. Smit, "We all are porous media," in *Poromechanics II*, CRC Press, 2020. doi: 10.1201/9781003078807-3.

[47]   D. J. Mooney, D. F. Baldwin, N. P. Suh, J. P. Vacanti, and R. Langer, "Novel approach to fabricate porous sponges of poly(d,l-lactic-co-glycolic acid) without the use of organic solvents," *Biomaterials*, vol. 17, no. 14, Jul. 1996, doi: 10.1016/0142-9612(96)87284-X.

[48]   M. N. Yousaf, B. T. Houseman, and M. Mrksich, "Using electroactive substrates to pattern the attachment of two different cell populations," *Proceedings of the National Academy of Sciences*, vol. 98, no. 11, May 2001, doi: 10.1073/pnas.101112898.

[49]   L. G. GRIFFITH, "Emerging Design Principles in Biomaterials and Scaffolds for Tissue Engineering," *Annals of the New York Academy of Sciences*, vol. 961, no. 1, Jun. 2002, doi: 10.1111/j.1749-6632.2002.tb03056.x.

[50]   A. Vats, N. S. Tolley, J. M. Polak, and J. E. Gough, "Scaffolds and biomaterials for tissue engineering: a review of clinical applications," *Clinical Otolaryngology and Allied Sciences*, vol. 28, no. 3, Jun. 2003, doi: 10.1046/j.1365-2273.2003.00686.x.

[51]   T. S. Karande, J. L. Ong, and C. M. Agrawal, "Diffusion in Musculoskeletal Tissue Engineering Scaffolds: Design Issues Related to Porosity, Permeability, Architecture, and Nutrient Mixing," *Annals of Biomedical Engineering*, vol. 32, no. 12, Dec. 2004, doi: 10.1007/s10439-004-7825-2.

[52]   L. Yang *et al.*, "Investigation on the orientation dependence of elastic response in Gyroid cellular structures," *Journal of the Mechanical Behavior of Biomedical Materials*, vol. 90, no. September 2018, pp. 73–85, 2019, doi: 10.1016/j.jmbbm.2018.09.042.

[53]   S. Arabnejad, R. Burnett Johnston, J. A. Pura, B. Singh, M. Tanzer, and D. Pasini, "High-strength porous biomaterials for bone replacement: A strategy to assess the interplay between cell morphology, mechanical properties, bone ingrowth and manufacturing constraints," *Acta Biomaterialia*, vol. 30, pp. 345–356, 2016, doi: 10.1016/j.actbio.2015.10.048.

[54] H. Zaharin *et al.*, "Effect of Unit Cell Type and Pore Size on Porosity and Mechanical Behavior of Additively Manufactured Ti6Al4V Scaffolds," *Materials*, vol. 11, no. 12, Nov. 2018, doi: 10.3390/ma11122402.

[55] H. Weinans, D. R. Sumner, R. Igloria, and R. N. Natarajan, "Sensitivity of periprosthetic stress-shielding to load and the bone density–modulus relationship in subject-specific finite element models," *Journal of Biomechanics*, vol. 33, no. 7, Jul. 2000, doi: 10.1016/S0021-9290(00)00036-1.

[56] X. Y. Zhang, G. Fang, and J. Zhou, "Additively manufactured scaffolds for bone tissue engineering and the prediction of their mechanical behavior: A review," *Materials*, vol. 10, no. 1, 2017, doi: 10.3390/ma10010050.

[57] M. Pelanconi and A. Ortona, "Nature-inspired, ultra-lightweight structures with gyroid cores produced by additive manufacturing and reinforced by unidirectional carbon fiber ribs," *Materials*, vol. 12, no. 24, pp. 1–14, 2019, doi: 10.3390/ma1224134.

[58] K. Michielsen and D. G. Stavenga, "Gyroid cuticular structures in butterfly wing scales: Biological photonic crystals," *Journal of the Royal Society Interface*, vol. 5, no. 18, pp. 85–94, 2008, doi: 10.1098/rsif.2007.1065.

[59] O. Al-Ketan, R. Rowshan, and R. K. Abu Al-Rub, "Topology-mechanical property relationship of 3D printed strut, skeletal, and sheet based periodic metallic cellular materials," *Additive Manufacturing*, vol. 19, no. January, pp. 167–183, 2018, doi: 10.1016/j.addma.2017.12.006.

[60] D. J. Yoo, "Porous scaffold design using the distance field and triply periodic minimal surface models," *Biomaterials*, vol. 32, no. 31, pp. 7741–7754, 2011, doi: 10.1016/j.biomaterials.2011.07.019.

[61] A. du Plessis, I. Yadroitsava, I. Yadroitsev, S. G. le Roux, and D. C. Blaine, "Numerical comparison of lattice unit cell designs for medical implants by additive manufacturing," *Virtual and Physical Prototyping*, vol. 13, no. 4, pp. 266–281, 2018, doi: 10.1080/17452759.2018.1491713.

[62] D. Barba, E. Alabort, and R. C. Reed, "Synthetic bone: Design by additive manufacturing," *Acta Biomaterialia*, vol. 97, no. August, pp. 637–656, 2019, doi: 10.1016/j.actbio.2019.07.049.

[63] C. Yan, L. Hao, A. Hussein, and P. Young, "Ti-6Al-4V triply periodic minimal surface structures for bone implants fabricated via selective laser melting," *Journal of the Mechanical Behavior of Biomedical Materials*, vol. 51, pp. 61–73, 2015, doi: 10.1016/j.jmbbm.2015.06.024.

[64] E. Yang *et al.*, "Effect of geometry on the mechanical properties of Ti-6Al-4V Gyroid structures fabricated via SLM: A numerical study," *Materials and Design*, vol. 184, p. 108165, 2019, doi: 10.1016/j.matdes.2019.108165.

[65] A. H. Schoen, "Infinite periodic minimal surfaces without self-intersections," *Nasa Technical Note D-5541*, p. 92, 1970, [Online]. Available: http://ntrs.nasa.gov/search.jsp?R=19700020472

[66] L. Riva, P. S. Ginestra, and E. Ceretti, "Mechanical characterization and properties of laser-based powder bed–fused lattice structures: a review," *The International Journal of Advanced Manufacturing Technology*, vol. 113, no. 3–4, pp. 649–671, Mar. 2021, doi: 10.1007/s00170-021-06631-4.

[67] L. Mullen, R. C. Stamp, W. K. Brooks, E. Jones, and C. J. Sutcliffe, "Selective laser melting: A regular unit cell approach for the manufacture of porous, titanium, bone in-growth constructs, suitable for orthopedic applications," *Journal of Biomedical*

Materials Research - Part B Applied Biomaterials, vol. 89, no. 2, pp. 325–334, 2009, doi: 10.1002/jbm.b.31219.

[68]   B. Otsuki, M. Takemoto, S. Fujibayashi, M. Neo, T. Kokubo, and T. Nakamura, "Pore throat size and connectivity determine bone and tissue ingrowth into porous implants: Three-dimensional micro-CT based structural analyses of porous bioactive titanium implants," *Biomaterials*, vol. 27, no. 35, pp. 5892–5900, 2006, doi: 10.1016/j.biomaterials.2006.08.013.

[69]   J. G. Torres-Rendon *et al.*, "Bioactive gyroid scaffolds formed by sacrificial templating of nanocellulose and nanochitin hydrogels as instructive platforms for biomimetic tissue engineering," *Advanced Materials*, vol. 27, no. 19, pp. 2989–2995, 2015, doi: 10.1002/adma.201405873.

[70]   M. R. Ashby and R. Medalist, "The Mechanical Properties of Cellular Solids," *The Metallurgical Society of AIME*, vol. 14, no. September, pp. 1755–1769, 1983.

[71]   P. Wang, X. Li, S. Luo, M. L. S. Nai, J. Ding, and J. Wei, "Additively manufactured heterogeneously porous metallic bone with biostructural functions and bone-like mechanical properties," *Journal of Materials Science and Technology*, vol. 62, pp. 173–179, 2021, doi: 10.1016/j.jmst.2020.05.056.

[72]   X. Z. Zhang, M. Leary, H. P. Tang, T. Song, and M. Qian, "Selective electron beam manufactured Ti-6Al-4V lattice structures for orthopedic implant applications: Current status and outstanding challenges," *Current Opinion in Solid State and Materials Science*, vol. 22, no. 3, pp. 75–99, 2018, doi: 10.1016/j.cossms.2018.05.002.

[73]   X. Wang *et al.*, "Topological design and additive manufacturing of porous metals for bone scaffolds and orthopaedic implants: A review," *Biomaterials*, vol. 83, Mar. 2016, doi: 10.1016/j.biomaterials.2016.01.012.

[74]   E. Alabort, D. Barba, and R. C. Reed, "Design of metallic bone by additive manufacturing," *Scripta Materialia*, vol. 164, pp. 110–114, 2019, doi: 10.1016/j.scriptamat.2019.01.022.

[75]   D. Mahmoud, M. A. Elbestawi, and B. Yu, "Process-structure-property relationships in selective laser melting of porosity graded gyroids," *Journal of Medical Devices, Transactions of the ASME*, vol. 13, no. 3, pp. 1–11, 2019, doi: 10.1115/1.4043736.

[76]   X. P. Tan, Y. J. Tan, C. S. L. Chow, S. B. Tor, and W. Y. Yeong, "Metallic powder-bed based 3D printing of cellular scaffolds for orthopaedic implants: A state-of-the-art review on manufacturing, topological design, mechanical properties and biocompatibility," *Materials Science and Engineering C*, vol. 76, pp. 1328–1343, 2017, doi: 10.1016/j.msec.2017.02.094.

[77]   D. Mahmoud and M. A. Elbestawi, "Selective laser melting of porosity graded lattice structures for bone implants," *International Journal of Advanced Manufacturing Technology*, vol. 100, no. 9–12, pp. 2915–2927, 2019, doi: 10.1007/s00170-018-2886-9.

[78]   C. Yan, L. Hao, A. Hussein, Q. Wei, and Y. Shi, "Microstructural and surface modifications and hydroxyapatite coating of Ti-6Al-4V triply periodic minimal surface lattices fabricated by selective laser melting," *Materials Science and Engineering C*, vol. 75, pp. 1515–1524, 2017, doi: 10.1016/j.msec.2017.03.066.

[79]   C. Yan, L. Hao, A. Hussein, and D. Raymont, "Evaluations of cellular lattice structures manufactured using selective laser melting," *International Journal of Machine Tools and Manufacture*, vol. 62, pp. 32–38, 2012, doi: 10.1016/j.ijmachtools.2012.06.002.

[80]   N. Yang, Z. Quan, D. Zhang, and Y. Tian, "Multi-morphology transition hybridization CAD design of minimal surface porous structures for use in tissue engineering," *CAD Computer Aided Design*, vol. 56, pp. 11–21, 2014, doi: 10.1016/j.cad.2014.06.006.

[81]   nTopology, "nTop Platform." https://ntopology.com/ntop-platform/, New York, NY 10013, USA, 2020. [Online]. Available: https://ntopology.com/ntop-platform/

[82]   T. Reiner, G. Mückl, and C. Dachsbacher, "Interactive modeling of implicit surfaces using a direct visualization approach with signed distance functions," *Computers and Graphics (Pergamon)*, vol. 35, no. 3, pp. 596–603, 2011, doi: 10.1016/j.cag.2011.03.010.

[83]   D. J. Yoo, "Three-dimensional human body model reconstruction and manufacturing from CT medical image data using a heterogeneous implicit solid based approach," *International Journal of Precision Engineering and Manufacturing*, vol. 12, no. 2, pp. 293–301, 2011, doi: 10.1007/s12541-011-0039-2.

[84]   G. Savio, S. Rosso, R. Meneghello, and G. Concheri, "Geometric modeling of cellular materials for additive manufacturing in biomedical field: A review," *Applied Bionics and Biomechanics*, vol. 2018, 2018, doi: 10.1155/2018/1654782.

[85]   X. Y. Liu, H. Wang, C. S. Chen, Q. Wang, X. Zhou, and Y. Wang, "Implicit surface reconstruction with radial basis functions via PDEs," *Engineering Analysis with Boundary Elements*, vol. 110, pp. 95–103, 2020, doi: 10.1016/j.enganabound.2019.09.021.

[86]   J. C. Carr *et al.*, "Reconstruction and representation of 3D objects with radial basis functions," in *Proceedings of the 28th Annual Conference on Computer Graphics and Interactive Techniques, SIGGRAPH 2001*, 2001, pp. 67–76. doi: 10.1145/383259.383266.

[87]   ISO 13314, "ISO 13314 Mechanical testing of metals, ductility testing, compression test for porous and cellular metals," *Reference number ISO*, vol. 13314, no. 13314, pp. 1–7, 2011, [Online]. Available: www.iso.org

[88]   "Ansys Mechanical."

[89]   M. Speirs, B. van Hooreweder, J. van Humbeeck, and J. P. Kruth, "Fatigue behaviour of NiTi shape memory alloy scaffolds produced by SLM, a unit cell design comparison," *Journal of the Mechanical Behavior of Biomedical Materials*, vol. 70, no. October 2016, pp. 53–59, 2017, doi: 10.1016/j.jmbbm.2017.01.016.

[90]   M. Afshar, A. Pourkamali Anaraki, and H. Montazerian, "Compressive characteristics of radially graded porosity scaffolds architected with minimal surfaces," *Materials Science and Engineering C*, vol. 92, no. May, pp. 254–267, 2018, doi: 10.1016/j.msec.2018.06.051.

[91]   F. Liu, Z. Mao, P. Zhang, D. Z. Zhang, J. Jiang, and Z. Ma, "Functionally graded porous scaffolds in multiple patterns: New design method, physical and mechanical properties," *Materials and Design*, vol. 160, pp. 849–860, 2018, doi: 10.1016/j.matdes.2018.09.053.

[92]   C. Yan, L. Hao, A. Hussein, and D. Raymont, "Evaluations of cellular lattice structures manufactured using selective laser melting," *International Journal of Machine Tools and Manufacture*, vol. 62, pp. 32–38, 2012, doi: https://doi.org/10.1016/j.ijmachtools.2012.06.002.

[93]   D. W. Abueidda, M. Elhebeary, C. S. (Andrew) Shiang, S. Pang, R. K. Abu Al-Rub, and I. M. Jasiuk, "Mechanical properties of 3D printed polymeric Gyroid cellular structures: Experimental and finite element study," *Materials and Design*, vol. 165, p. 107597, 2019, doi: 10.1016/j.matdes.2019.107597.

[94] N. W. Hrabe, P. Heinl, B. Flinn, C. Körner, and R. K. Bordia, "Compression-compression fatigue of selective electron beam melted cellular titanium (Ti-6Al-4V)," *Journal of Biomedical Materials Research Part B: Applied Biomaterials*, vol. 99B, no. 2, pp. 313–320, Nov. 2011, doi: 10.1002/jbm.b.31901.

[95] L. Yang, R. Mertens, M. Ferrucci, C. Yan, Y. Shi, and S. Yang, "Continuous graded Gyroid cellular structures fabricated by selective laser melting: Design, manufacturing and mechanical properties," *Materials and Design*, vol. 162, pp. 394–404, 2019, doi: 10.1016/j.matdes.2018.12.007.

[96] O. Fashanu *et al.*, "Effective elastic properties of additively manufactured metallic cellular structures using numerical unit-cell homogenization," *Progress in Additive Manufacturing*, vol. 5, no. 4, Dec. 2020, doi: 10.1007/s40964-020-00141-7.

[97] I. Maskery and I. A. Ashcroft, "The deformation and elastic anisotropy of a new gyroid-based honeycomb made by laser sintering," *Additive Manufacturing*, vol. 36, Dec. 2020, doi: 10.1016/j.addma.2020.101548.

[98] F. P. W. Melchels, A. M. C. Barradas, C. A. van Blitterswijk, J. de Boer, J. Feijen, and D. W. Grijpma, "Effects of the architecture of tissue engineering scaffolds on cell seeding and culturing," *Acta Biomaterialia*, vol. 6, no. 11, pp. 4208–4217, 2010, doi: 10.1016/j.actbio.2010.06.012.

[99] A. A. Zadpoor, "Bone tissue regeneration: The role of scaffold geometry," *Biomaterials Science*, vol. 3, no. 2, pp. 231–245, 2015, doi: 10.1039/c4bm00291a.

[100] L. Guariento, F. Buonamici, A. Marzola, Y. Volpe, and L. Governi, "Graded Gyroid Structures for Load Bearing Orthopedic Implants," Nov. 2020. doi: 10.1109/NAP51477.2020.9309692.

[101] M. A. Fuessinger *et al.*, "Planning of skull reconstruction based on a statistical shape model combined with geometric morphometrics," *International Journal of Computer Assisted Radiology and Surgery*, vol. 13, no. 4, Apr. 2018, doi: 10.1007/s11548-017-1674-6.

[102] T. F. Cootes, C. J. Taylor, D. H. Cooper, and J. Graham, "Active Shape Models-Their Training and Application," *Computer Vision and Image Understanding*, vol. 61, no. 1, Jan. 1995, doi: 10.1006/cviu.1995.1004.

[103] T. F. Cootes, G. J. Edwards, and C. J. Taylor, "Active appearance models," 1998. doi: 10.1007/BFb0054760.

[104] T. Heimann and H. P. Meinzer, "Statistical shape models for 3D medical image segmentation: A review," *Medical Image Analysis*, vol. 13, no. 4, pp. 543–563, 2009, doi: 10.1016/j.media.2009.05.004.

[105] T. Heimann *et al.*, "Comparison and Evaluation of Methods for Liver Segmentation From CT Datasets," *IEEE Transactions on Medical Imaging*, vol. 28, no. 8, Aug. 2009, doi: 10.1109/TMI.2009.2013851.

[106] E. A. Audenaert *et al.*, "Cascaded statistical shape model based segmentation of the full lower limb in CT," *Computer Methods in Biomechanics and Biomedical Engineering*, vol. 22, no. 6, Apr. 2019, doi: 10.1080/10255842.2019.1577828.

[107] M. A. Fuessinger *et al.*, "Virtual reconstruction of bilateral midfacial defects by using statistical shape modeling," *Journal of Cranio-Maxillofacial Surgery*, vol. 47, no. 7, Jul. 2019, doi: 10.1016/j.jcms.2019.03.027.

[108] A. Marzola, L. Governi, L. Genitori, F. Mussa, Y. Volpe, and R. Furferi, "A Semi-Automatic Hybrid Approach for Defective Skulls Reconstruction," *Computer-Aided Design and Applications*, vol. 17, no. 1, May 2019, doi: 10.14733/cadaps.2020.190-204.

[109] C. S. Mendoza, N. Safdar, K. Okada, E. Myers, G. F. Rogers, and M. G. Linguraru, "Personalized assessment of craniosynostosis via statistical shape modeling," *Medical Image Analysis*, vol. 18, no. 4, May 2014, doi: 10.1016/j.media.2014.02.008.

[110] W. Keustermans *et al.*, "High quality statistical shape modelling of the human nasal cavity and applications," *Royal Society Open Science*, vol. 5, no. 12, Dec. 2018, doi: 10.1098/rsos.181558.

[111] J. T. Lynch *et al.*, "Statistical shape modelling reveals large and distinct subchondral bony differences in osteoarthritic knees," *Journal of Biomechanics*, vol. 93, Aug. 2019, doi: 10.1016/j.jbiomech.2019.07.003.

[112] F. Gelaude, T. Clijmans, P. L. Broos, B. Lauwers, and J. vander Sloten, "Computer-aided planning of reconstructive surgery of the innominate bone: Automated correction proposals," *Computer Aided Surgery*, vol. 12, no. 5, Jan. 2007, doi: 10.3109/10929080701684762.

[113] T. F. Cootes, C. J. Taylor, D. H. Cooper, and J. Graham, "Training Models of Shape from Sets of Examples," in *BMVC92*, London: Springer London, 1992. doi: 10.1007/978-1-4471-3201-1_2.

[114] F. L. Bookstein, "Landmark methods for forms without landmarks: morphometrics of group differences in outline shape," *Medical Image Analysis*, vol. 1, no. 3, Apr. 1997, doi: 10.1016/S1361-8415(97)85012-8.

[115] A. Marzola, M. Servi, and Y. Volpe, "A Reliable Procedure for the Construction of a Statistical Shape Model of the Cranial Vault," 2020. doi: 10.1007/978-3-030-31154-4_67.

[116] T. Heimann and H.-P. Meinzer, "Statistical shape models for 3D medical image segmentation: A review," *Medical Image Analysis*, vol. 13, no. 4, Aug. 2009, doi: 10.1016/j.media.2009.05.004.

[117] "23. https://www.cancerimagingarchive.net."

[118] Y. Tripathi, M. Shukla, and A. D. Bhatt, "Implicit-Function-Based Design and Additive Manufacturing of Triply Periodic Minimal Surfaces Scaffolds for Bone Tissue Engineering," *Journal of Materials Engineering and Performance*, vol. 28, no. 12, pp. 7445–7451, 2019, doi: 10.1007/s11665-019-04457-6.

[119] "3D Medical Image Processing Software | Materialise Mimics."

[120] R. Ghosh, B. Pal, D. Ghosh, and S. Gupta, "Finite element analysis of a hemi-pelvis: the effect of inclusion of cartilage layer on acetabular stresses and strain," *Computer Methods in Biomechanics and Biomedical Engineering*, vol. 18, no. 7, May 2015, doi: 10.1080/10255842.2013.843674.

[121] A. E. Anderson, C. L. Peters, B. D. Tuttle, and J. A. Weiss, "Subject-specific finite element model of the pelvis: Development, validation and sensitivity studies," *Journal of Biomechanical Engineering*, vol. 127, no. 3, pp. 364–373, 2005, doi: 10.1115/1.1894148.

[122] P. Hu *et al.*, "Influence of Different Boundary Conditions in Finite Element Analysis on Pelvic Biomechanical Load Transmission," *Orthopaedic Surgery*, vol. 9, no. 1, pp. 115–122, 2017, doi: 10.1111/os.12315.

[123] A. E. Anderson, B. J. Ellis, S. A. Maas, and J. A. Weiss, "Effects of idealized joint geometry on finite element predictions of cartilage contact stresses in the hip," *Journal of Biomechanics*, vol. 43, no. 7, pp. 1351–1357, 2010, doi: 10.1016/j.jbiomech.2010.01.010.

[124] Z. Hao, "The Effect of Boundary Condition on the Biomechanics of a Human Pelvic Joint Under an Axial Compressive Load: A Three-Dimensional Finite Element

Model," *Journal of Biomechanical Engineering*, vol. 133, no. 10, p. 101006, 2011, doi: 10.1115/1.4005223.

[125]   P. L. Ricci, S. Maas, J. Kelm, and T. Gerich, "Finite element analysis of the pelvis including gait muscle forces: an investigation into the effect of rami fractures on load transmission," *Journal of Experimental Orthopaedics*, vol. 5, no. 1, 2018, doi: 10.1186/s40634-018-0151-7.

[126]   E. P. Ravera, M. J. Crespo, F. A. Guarnieri, and A. A. Braidot, "Stress in Human Pelvis throughout the Gait Cycle: Development, Evaluation and Sensitivity Studies of a Finite Element Model," 2015. doi: 10.1007/978-3-319-13117-7_64.

[127]   M. Dalstra and R. Huiskes, "Load transfer across the pelvic bone," *Journal of Biomechanics*, vol. 28, no. 6, Jun. 1995, doi: 10.1016/0021-9290(94)00125-N.

[128]   D. Shi, F. Wang, D. Wang, X. Li, and Q. Wang, "3-D finite element analysis of the influence of synovial condition in sacroiliac joint on the load transmission in human pelvic system," *Medical Engineering & Physics*, vol. 36, no. 6, Jun. 2014, doi: 10.1016/j.medengphy.2014.01.002.

[129]   A. T. M. Phillips, P. Pankaj, C. R. Howie, A. S. Usmani, and A. H. R. W. Simpson, "Finite element modelling of the pelvis: Inclusion of muscular and ligamentous boundary conditions," *Medical Engineering & Physics*, vol. 29, no. 7, Sep. 2007, doi: 10.1016/j.medengphy.2006.08.010.

[130]   Z. Hao, C. Wan, X. Gao, and T. Ji, "The Effect of Boundary Condition on the Biomechanics of a Human Pelvic Joint Under an Axial Compressive Load: A Three-Dimensional Finite Element Model," *Journal of Biomechanical Engineering*, vol. 133, no. 10, Oct. 2011, doi: 10.1115/1.4005223.

[131]   K. C. Wong, S. M. Kumta, N. v. Geel, and J. Demol, "One-step reconstruction with a 3D-printed, biomechanically evaluated custom implant after complex pelvic tumor resection," *Computer Aided Surgery*, vol. 20, no. 1, Jan. 2015, doi: 10.3109/10929088.2015.1076039.

[132]   S. Ahmad *et al.*, "Simulation of Hip Implant with respect to the Clearance between the Bone and Endoprosthesis: A Case Study," *Procedia CIRP*, vol. 89, 2020, doi: 10.1016/j.procir.2020.05.120.

[133]   E. Dong *et al.*, "Finite Element Analysis of the Pelvis after Customized Prosthesis Reconstruction," *Journal of Bionic Engineering*, vol. 15, no. 3, pp. 443–451, 2018, doi: 10.1007/s42235-018-0035-7.

[134]   L. Maslov *et al.*, "Some aspects of custom-made 3d-printed hip joint implant structural simulation," *IOP Conference Series: Materials Science and Engineering*, vol. 986, Dec. 2020, doi: 10.1088/1757-899X/986/1/012035.

[135]   K. Haase and G. Rouhi, "Prediction of stress shielding around an orthopedic screw: Using stress and strain energy density as mechanical stimuli," *Computers in Biology and Medicine*, vol. 43, no. 11, p. 1748, 2013, doi: 10.1016/j.compbiomed.2013.07.032.

[136]   H. Weinans, D. R. Sumner, R. Igloria, and R. N. Natarajan, "Sensitivity of periprosthetic stress-shielding to load and the bone density-modulus relationship in subject-specific finite element models," *Journal of Biomechanics*, vol. 33, no. 7, pp. 809–817, 2000, doi: 10.1016/S0021-9290(00)00036-1.

[137]   E. Siggelkow, D. Hertig, K. Widmer, H. P.- Bone, and U. 2004, "Construction and validation of a finite element model of a human pelvis," *Proceedings of Computer Methods in Biomechanics and Biomedical Engineering, Madrid. FIRST Numerics.*, pp.   1971–1973,   2004,   [Online].   Available: https://isbweb.org/images/conf/2001/Longabstracts/PDF/0100_0199/0146.pdf

[138] J. Lei, P. Dong, Z. Li, F. Zhu, Z. Wang, and X. Cai, "Biomechanical analysis of the fixation systems for anterior column and posterior hemi-transverse acetabular fractures," *Acta Orthopaedica et Traumatologica Turcica*, vol. 51, no. 3, May 2017, doi: 10.1016/j.aott.2017.02.003.

[139] T. Iqbal *et al.*, "Development of finite element model for customized prostheses design for patient with pelvic bone tumor," *Proceedings of the Institution of Mechanical Engineers, Part H: Journal of Engineering in Medicine*, vol. 231, no. 6, Jun. 2017, doi: 10.1177/0954411917692009.

[140] A. S. O. Leung, L. M. Gordon, T. Skrinskas, T. Szwedowski, and C. M. Whyne, "Effects of bone density alterations on strain patterns in the pelvis: Application of a finite element model," *Proceedings of the Institution of Mechanical Engineers, Part H: Journal of Engineering in Medicine*, vol. 223, no. 8, Nov. 2009, doi: 10.1243/09544119JEIM618.

[141] J.-T. Hsu *et al.*, "The number of screws, bone quality, and friction coefficient affect acetabular cup stability," *Medical Engineering & Physics*, vol. 29, no. 10, Dec. 2007, doi: 10.1016/j.medengphy.2006.11.005.

[142] P. Hu *et al.*, "Influence of Different Boundary Conditions in Finite Element Analysis on Pelvic Biomechanical Load Transmission," *Orthopaedic Surgery*, vol. 9, no. 1, Feb. 2017, doi: 10.1111/os.12315.

[143] M. Dalstra and R. Huiskes, "Load transfer across the pelvic bone," *Journal of Biomechanics*, vol. 28, no. 6, pp. 715–724, 1995, doi: 10.1016/0021-9290(94)00125-N.

[144] A. T. M. Phillips, P. Pankaj, C. R. Howie, A. S. Usmani, and A. H. R. W. Simpson, "Finite element modelling of the pelvis: Inclusion of muscular and ligamentous boundary conditions," *Medical Engineering and Physics*, vol. 29, no. 7, pp. 739–748, 2007, doi: 10.1016/j.medengphy.2006.08.010.

[145] M. Dalstra, R. Huiskes, and L. van Erning, "Development and validation of a three-dimensional finite element model of the pelvic bone," *Journal of Biomechanical Engineering*, vol. 117, no. 3, pp. 272–278, 1995, doi: 10.1115/1.2794181.

[146] A. S. O. Leung, L. M. Gordon, T. Skrinskas, T. Szwedowski, and C. M. Whyne, "Effects of bone density alterations on strain patterns in the pelvis: Application of a finite element model," *Proceedings of the Institution of Mechanical Engineers, Part H: Journal of Engineering in Medicine*, vol. 223, no. 8, pp. 965–979, 2009, doi: 10.1243/09544119JEIM618.

[147] T. Iqbal *et al.*, "Development of finite element model for customized prostheses design for patient with pelvic bone tumor," *Proceedings of the Institution of Mechanical Engineers, Part H: Journal of Engineering in Medicine*, vol. 231, no. 6, pp. 525–533, 2017, doi: 10.1177/0954411917692009.

[148] E. Dong *et al.*, "Finite Element Analysis of the Pelvis after Customized Prosthesis Reconstruction," *Journal of Bionic Engineering*, vol. 15, no. 3, pp. 443–451, 2018, doi: 10.1007/s42235-018-0035-7.

[149] S. G. Clarke, A. T. M. Phillips, and A. M. J. Bull, "Evaluating a suitable level of model complexity for finite element analysis of the intact acetabulum," *Computer Methods in Biomechanics and Biomedical Engineering*, vol. 16, no. 7, pp. 717–724, 2013, doi: 10.1080/10255842.2011.633906.

[150] R. Ghosh, B. Pal, D. Ghosh, and S. Gupta, "Finite element analysis of a hemi-pelvis: the effect of inclusion of cartilage layer on acetabular stresses and strain," *Computer*

Methods in Biomechanics and Biomedical Engineering, vol. 18, no. 7, pp. 697–710, 2015, doi: 10.1080/10255842.2013.843674.

[151]   R. Huiskes, H. Weinans, H. J. Grootenboer, M. Dalstra, B. Fudala, and T. J. Slooff, "Adaptive bone-remodeling theory applied to prosthetic-design analysis," *Journal of Biomechanics*, vol. 20, no. 11–12, Jan. 1987, doi: 10.1016/0021-9290(87)90030-3.

[152]   E. Dong *et al.*, "Finite Element Analysis of the Pelvis after Customized Prosthesis Reconstruction," *Journal of Bionic Engineering*, vol. 15, no. 3, May 2018, doi: 10.1007/s42235-018-0035-7.

[153]   M. Schimmelpfenning, "Patient specific optimization of fracture treatment considering the inhomogeneous material properties of bone tissue and the expected load situation," *10. Weimarer Optimierungs- und Stochastiktage 2013*, 2013, [Online]. Available:
http://www.dynardo.de/fileadmin/Material_Dynardo/bibliothek/WOST10/03_WOST 2013_Optimization_Schimmelpfennig_Paper.pdf